LASER INTERFEROMETER GRAVITATIONAL WAVE OBSERVATORY
- LIGO -
==========
LIGO SCIENTIFIC COLLABORATION

Technical Note	**LIGO-T1400226-v10**	2024/09/25

LIGO Voyager Upgrade: Design Concept

Rana X Adhikari, Aidan Brooks, Brett Shapiro, Radhika Bhatt, David McClelland, Francisco Salces Carcoba, Aaron Markowitz, Michael Laxen, Eric K. Gustafson, Valery Mitrofanov, Koji Arai, Yuta Michimura, Christopher Wipf, Edgard Bonilla

Auto-generated by voyagerwhitepaper repository @ 7ea783a8

California Institute of Technology
LIGO Project, MS 100-36
Pasadena, CA 91125
Phone (626) 395-2129
Fax (626) 304-9834
E-mail: info@ligo.caltech.edu

Massachusetts Institute of Technology
LIGO Project, Room NW22-295
Cambridge, MA 02139
Phone (617) 253-4824
Fax (617) 253-7014
E-mail: info@ligo.mit.edu

LIGO Hanford Observatory
Route 10, Mile Marker 2
Richland, WA 99352
Phone (509) 372-8106
Fax (509) 372-8137
E-mail: info@ligo.caltech.edu

LIGO Livingston Observatory
19100 LIGO Lane
Livingston, LA 70754
Phone (225) 686-3100
Fax (225) 686-7189
E-mail: info@ligo.caltech.edu

http://www.ligo.org/

Contents

List of Figures

List of Tables

1 Introduction

The LIGO Voyager upgrade consists of a number of technological improvements aimed at improving the broadband strain sensitivity of LIGO beyond the Advanced LIGO+ levels. This document describes the technical details and motivations for these design choices.

There are several potential advantages of this technology, which are described in the text. There are also many areas where the R&D is not yet mature enough to accurately determine the risks involved.

This upgrade is not as incremental as the A-plus and A-sharp upgrades, and so there is a risk that at the end, the performance would be worse than the other room temperature upgrade concepts. However, the risks associated with the other (A-sharp) option are also substantial and there is a substantial possibility that the coating thermal noise and high stored power goals may not be met.

1.1 Structure of this document

This white paper discusses the technical and logistic details of all the upgrades for LIGO Voyager with the goals of (a) investigating the feasibility of all the required technology, largely illustrated in Figure 1, and highlighting those technological areas that require further research and (b) describing all the key noise contributions illustrated in the noise budget in Figure 3 (and thus determining the LIGO Voyager sensitivity).

To assist with readability, most of the section follow a similar structure, namely:

1. **Overview**: a few short paragraphs describing the background of the subsystem. Also details of elements of the subsystem that are unchanged for LIGO Voyager.
2. **Requirements**: a discussion of the requirements/objectives of the changes to the subsystem
3. **Technical details**: all the relevant technical details regarding the improvements in the subsystem. Very extensive details and supplementary information are in the appendices as opposed to this subsection.
4. **Unresolved issues**: Details of outstanding issues and problems for this subsystem that are still To Be Resolved and that require further R&D.
5. **Development approach & timeline**: projections of the timeline for work that needs to be done, including unresolved issues, for this subsystem to be ready for LIGO Voyager. Also discussion of installation and commissioning timelines for these elements.

The sections focus on technical details of the overall system or specific subsystems with one additional section discussing design choice for laser wavelength. The sections are:

- Section 2 provides a basic overview of the Voyager design concept, discusses the baseline optical topology and variations on this design and explores the sensitivity curves for all variations.
- Section 3 describes the silicon core optics and their coatings. We examine the feasibility of using large, cryogenically-cooled (123 K) silicon test masses. Additionally, this section describes a coating design corresponding to the Brownian noise curve shown in the noise budget and also identifies coating absorption as a key obstacle that must be overcome.
- Section 4 discusses the cryogenic operation, cooling system and shielding for LIGO Voyager and reviews the relevant heat budget, and relavent noise sources.
- Section 5 describes the suspension upgrades necessary to operate LIGO Voyager. It explores the practicality of manufacturing these silicon components. The suspension thermal noise (associated with the use of silicon blades and ribbons) is also described.
- Section 6 describes the changes needed for the Arm Length Stabilization system to operate in the near infrared.
- Section 7 describes the thermal compensation system. The choice of a low-thermal-expansion silicon substrate makes the design substantially different from aLIGO.
- Section 8 describes the requirements for a 2 micron laser system to replace the existing PSL. We review the development of mid-IR laser sources and find no significant impediment to producing a ~200 W, low-noise, single-frequency, 2 micron laser within the next 10 years.
- Section 9 details quantum noise (shot noise and radiation pressure) for LIGO Voyager and the necessary steps to get squeezing at a new laser wavelength. Quantum noise as a limiting noise source and the feasibility of injecting 18 dB of frequency–dependent squeezed vacuum at 2 microns.
- Section 10 describes the considerations for the choice of main laser wavelength including a list of pros and cons for longer and shorter wavelength.
- Section 11 describes the System design, interfaces between different subsystems and also discusses auxiliary issues and smaller subsystems affected by the change in wavelength, temperature and material.

2 Overview of LIGO Voyager

The LIGO Voyager upgrade is a replacement of the lasers and optics of the LIGO detectors to enable operation at modest cryogenic temperatures, with a concomitant increase of the astrophysical reach over the future Advanced LIGO configuration (aka 'A+').

Below, we describe the major technical differences, sensitivity improvements, and major remaining risks.

2.1 Background

The current LIGO detectors will approach the thermodynamic and quantum mechanical limits of their designs within a few years. Over the next several years, aLIGO will undergo an upgrade, designated "A+". The aim of this upgrade is chiefly to lower the quantum noise through the use of squeezed [1] light, and also to reduce somewhat the thermal noise from the mirror coatings. This upgrade has the goal of enhancing the sensitivity by ~50% [102] and is scheduled to be operational and taking science data in the latter part of this decade.

In this article, we describe a more substantial upgrade, called "LIGO Voyager", that will increase the range by a factor of 4 – 5 over aLIGO, and the event rate by approximately 100 times, to roughly one detection per hour. Such a dramatic change in the sensitivity should increase the detection rate of binary neutron star mergers to about 10 per day and the rate of binary black hole mergers to around 30 per day. This upgraded instrument would be able to detect binary black holes out to a redshift of 10.

The path to LIGO Voyager requires reducing several noise sources, including:

1. quantum radiation pressure and shot noise,
2. mirror thermal noise,
3. mirror suspension thermal noise,
4. Newtonian gravity noise

All of these noise sources are addressed by the LIGO Voyager design, with the goal of commissioning and observational runs within a decade.

2.2 Justification

The most significant design changes in LIGO Voyager versus Advanced LIGO can be traced to the need to reduce the quantum noise in tandem with the mirror thermal noise.

[1] this has been mostly done and is in use during the O4 run.

- Quantum noise will be reduced by increasing the optical power stored in the arms. In Advanced LIGO, the stored power is limited by thermally induced wavefront distortion effects in the fused silica test masses. These effects will be alleviated by choosing a test mass material with a high thermal conductivity, such as silicon.
- The test mass temperature will be lowered to 123 K, to mitigate thermo-elastic noise. This species of thermal noise is especially problematic in test masses that are good thermal conductors. Fortunately, in silicon at 123 K, the thermal expansion coefficient crosses zero, which eliminates thermo-elastic noise. (Other plausible material candidates, such as sapphire, require cooling to near 0 K to be free of this noise.)
- The thermal noise of the mirror coating will be reduced by switching to low dissipation amorphous silicon based coatings, and by reducing the temperature. Achieving low optical absorption in the amorphous silicon coatings requires an increased laser wavelength.

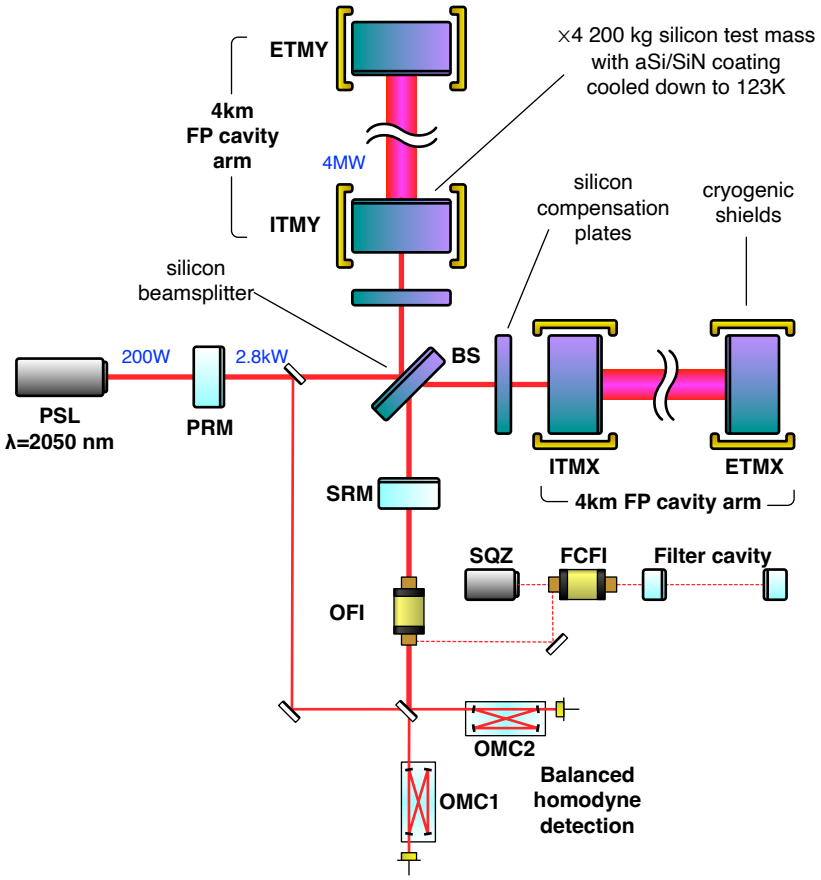

FIGURE 1: A simplified schematic layout of LIGO Voyager. Dual-recycled Fabry-Perot Michelson (DRFPMI) with frequency dependent squeezed light injection. The beam from a 2µm pre-stabilized laser (PSL), passes through an input mode cleaner (IMC) and is injected into the DRFPMI via the power-recycling mirror (PRM). Signal bandwidth is shaped via the signal recycling mirror (SRM). A squeezed vacuum source (SQZ) injects this vacuum into the DRFPMI via an output Faraday isolator (OFI) after it is reflected off a filter-cavity to provide frequency dependent squeezing. A Faraday isolator (FCFI) facilitates this coupling to the filter cavity. The output from the DRFPMI is incident on a balanced homodyne detector, which employs two output mode cleaner cavities (OMC1 and OMC2) and the local oscillator light picked off from the DRFPMI. Cold shields surround the input and end test masses in both the X and Y arms (ITMX, ITMY, ETMX and ETMY) to maintain a temperature of 123 K in these optics. The high-reflectivity coatings of the test masses are made from amorphous silicon.

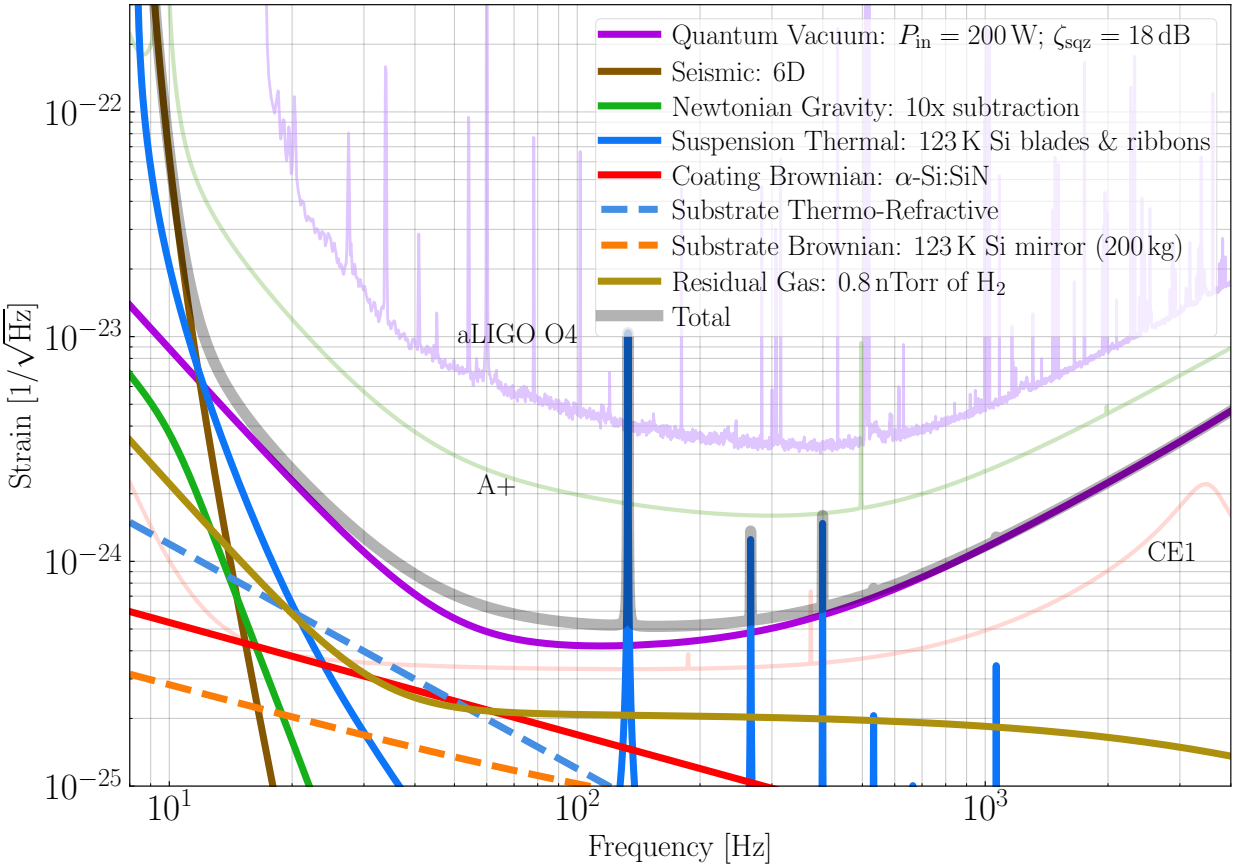

FIGURE 2: Noise Budget of LIGO Voyager Deep noise curve compared to Advanced LIGO during O4, and the CE1 and A+ design goals.

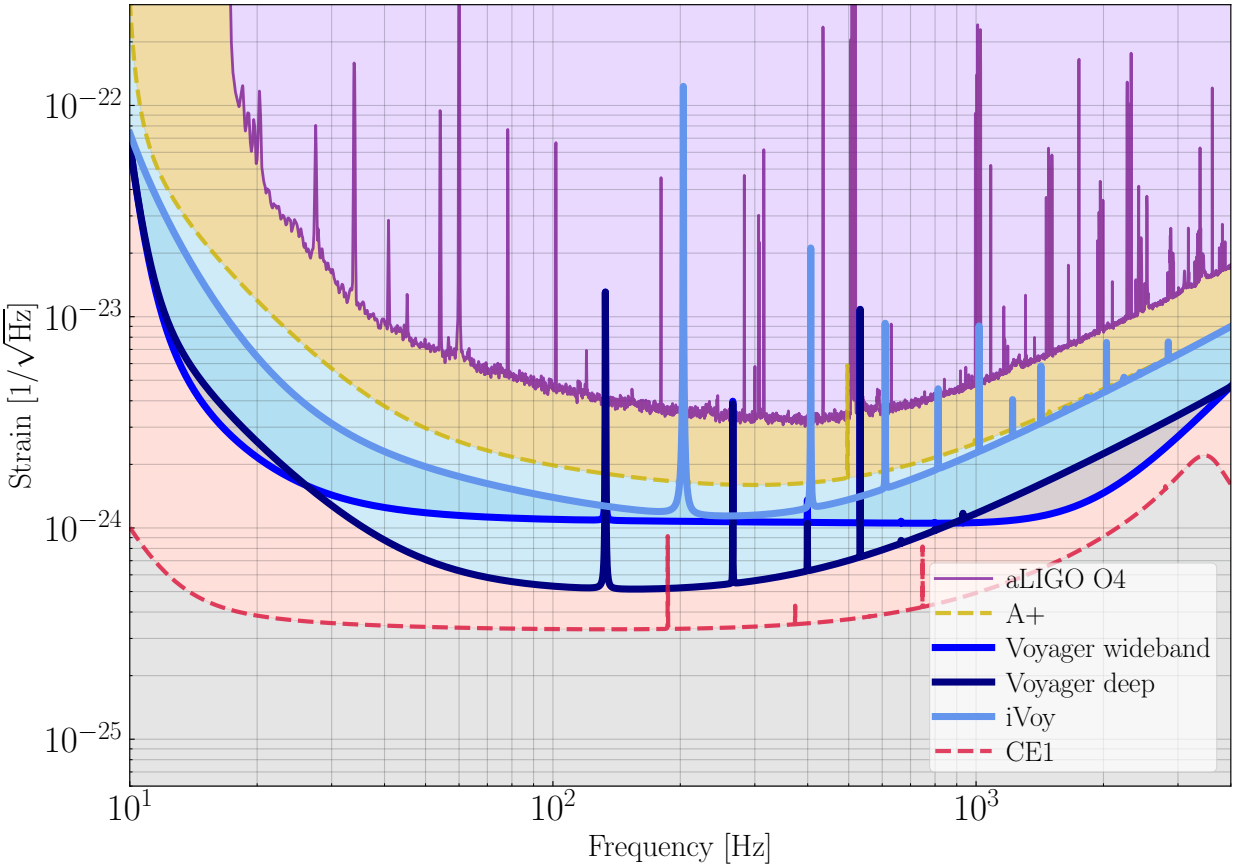

FIGURE 3: LIGO Voyager noise curves compared to Advanced LIGO during O4, and the CE1 and A+ design goals.

2.3 Design overview and variations

2.3.1 Baseline Voyager: Deep and wideband

The LIGO Voyager design is illustrated in Figure 1, with critical parameters called out in Table 1. The dual-recycled, Fabry-Perot Michelson topology is similar to Advanced LIGO and A+, with the following additional upgrades. Optical coatings on the cryogenically-cooled (123 K) test masses will be made from amorphous silicon, with the lower coating mechanical loss and cryogenic operation reducing the coating thermal noise. The 200 kg test-masses will be made of crystalline silicon (rather than fused silica). The absorption spectrum of the test mass materials requires us to choose a longer wavelength laser. The longer wavelength will also significantly reduce optical scattering from the mirrors, lowering losses and allowing for higher finesse arm cavities. The quantum noise (shot noise and radiation pressure) will be reduced by a combination of frequency-dependent squeezing, heavier test masses, and higher stored power in the arms. Finally, the environmentally produced Newtonian gravitational noise [57] will be reduced using seismometer arrays combined with adaptive noise regression [22, 34].

The LIGO Voyager noise budget and design sensitivity relative to other interferometer are shown in Figure 2 and Figure 3, respectively. Horizon distances for astrophysical sources are illustrated in Figure 4a and Figure 4b, showing the improvement over the Advanced LIGO design.

As with all modern GWD, Voyager can be operated in Deep and Wideband modes with appropriate choice of signal recycling mirror reflectivity.

Although most optical components will need to be changed to handle the new wavelength, we plan on reusing the Advanced LIGO hardware and infrastructure wherever possible (for example, the seismic isolation platforms, vacuum systems, electronics and infrastructure).

Some Design Highlights

1. 100 kg–200 kg silicon test masses to reduce radiation pressure(see Section 3)
2. α-Si:SiN multi-layer coatings (see Section 3.3.2) for reduced thermal noise.
3. Low temperature (~123 K) operation of the silicon test masses at zero thermal expansion point(see Section 4).
4. Low temperature operation of silicon ribbons for the final stage of test mass suspension (see Section 5).
5. 200 W, CW, pre-stabilized laser, with a ~2000 nm wavelength (see Section 8).
6. Squeezed light injection in combination with a squeezed light filter cavity (see Section 9).

7. Newtonian Gravity noise subtraction with seismometer arrays and adaptive filtering.

Key parameter changes from the aLIGO detectors are listed in Table 14.

2.3.2 Risk Reduction Option: Intermediate Voyager

We have identified several key technologies that still need development to achieve the baseline Voyager design. In order to maximize the chances of success and proceed as soon as possible, we propose a lower sensitivity version of Voyager that significantly reduces risk. Specifically,

- **Smaller test masses.** Using 100 kg, 30 cm diameter silicon test masses, as opposed to 45 cm diameter. This reduces risk due to the ready availability of boules of silicon in the smaller size at the appropriate purity levels. This has the added benefit that the 100 kg mass is the target load for the Heavy SUS being designed for A-Sharp. The penalty is higher radiation pressure and higher CTN due to larger beam sizes. Annealing of the test mass to trap residual oxygen should be easier.
- **Hybrid coatings to reduce absorption.** Adding a few layers of SiO_2 and tantala to the top of the a:Si coatings to reduce the absorption. This reduces the technology development risk for low absorption a:Si coatings at the cost of marginally increased coating thermal noise.
- **Metal blade springs**. The blade springs suspending the penultimate stage will be metal instead of silicon. These are readily available and are an established technology but will have elevated suspension thermal noise relative to future silicon blades.
- **Metal suspension wires**. The suspension wires will be made of beryillium copper (BeCu) instead of silicon. These are readily available and are an established technology but will have elevated suspension thermal noise relative to future silicon ribbons.

The iVoyager (iVoy) sensitivity curve is shown in Fig. 3. As can be seen, the main penalty is increased noise at frequencies below 100 Hz and particularly below 20 Hz.

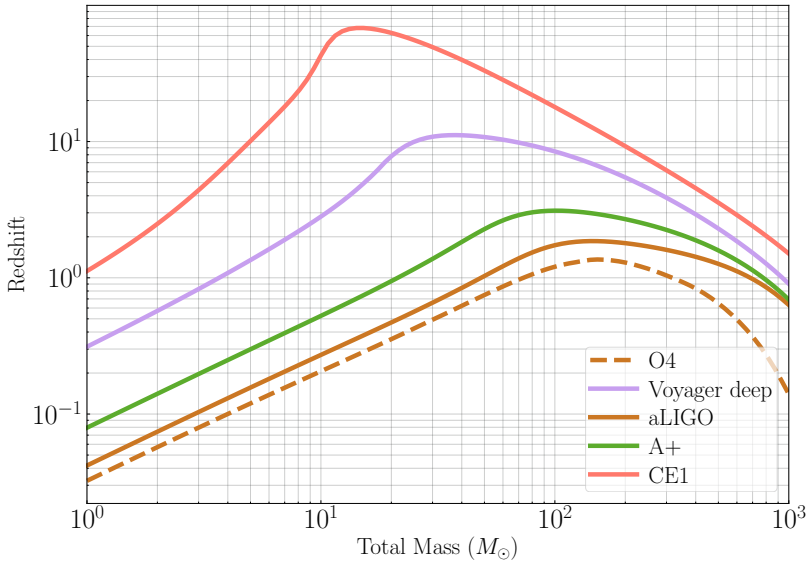

(A)

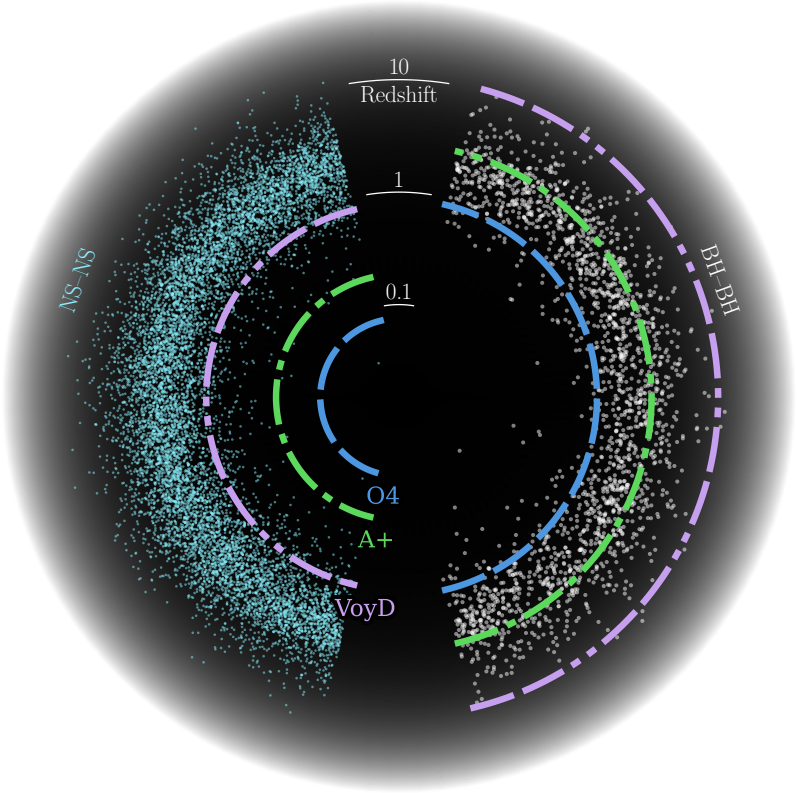

(B)

FIGURE 4: (A) Distance at which an optimally oriented, equal mass, binary black hole merger can be detected (with SNR = 8) as a function of the total mass of the binary (in the source frame). (B) Donut visualization of the horizon distance of LIGO Voyager Deep, aLIGO, and A+, shown with a population of binary neutron star mergers (blue) and 30 – 30 $M_\odot$ binary black hole mergers (gray). This assumes a Madau-Dickinson star formation rate [89] and a typical merger time of 100 Myr.

2.4 List of critical parameters

Parameter	Voyager Deep (Wideband)	Intermediate Voy.
Laser wavelength	2050 nm	2050 nm
Input laser power	200 W	60 W
PRC power	2.8 kW	840 W
Arm power	3.92 MW	1.18 MW
Mirror substrate	Silicon	Silicon
Mirror radius	22.5 cm	15.0 cm
Mirror thickness	30.0 cm†	60.0 cm
Beam radius on ITM/ETM	5.9 cm/8.5 cm	5.6 cm/5.6 cm
ITM ROC	1800 m	2570 m
ETM ROC	2500 m	2570 m
ITM transmission	0.0014	0.0014
PRM transmission	0.072	0.072
SRM transmission	0.040 (0.0051)	0.048
TM mass	200 kg†	100 kg
TM temperature	123 K	123 K
Suspension	silicon ribbon	beryillium copper

TABLE 1: Relevant parameters for the LIGO Voyager design. (†: Additional silicon elements are bonded to the outer diameter. Hence, the optic is not purely cylindrical and a simple $\rho \pi r^2 h$ calculation does not yield the mass.)

3 Core Optics

3.1 Overview

The central part of this interferometer upgrade is the change of the test mass optics from silica (SiO_2) to silicon. There are a number of reasons why silicon is a compelling choice:

1. Silicon has high thermal conductivity at cryogenic temperatures. This reduces the temperature gradients that are generated by laser heating.
2. The mechanical loss in silicon is low, similar to that of fused silica and sapphire.
3. In silicon, the thermal expansion coefficient crosses zero at 123 K. Near this temperature, thermo-elastic distortions of the mirror surface are drastically reduced, as is thermo-elastic noise due to thermodynamic temperature fluctuations.
4. Silicon can be produced in large sizes. Boules up to 45 cm are within the capabilities of silicon manufacturers. These allow for mirrors having masses up to 200 kg.
5. Silicon is commercially available with high purity levels, consistent with low absorption in the substrates at wavelengths of 1500 – 2200 nm.

Silicon was previously proposed as a test mass material in other contexts [63, 122, 125], and has a long history of use for optics that handle high incident power [7, 12].

3.2 Requirements

3.2.1 Optical Requirements

- **Substrate**
  - **Substrate bulk absorption:** The bulk absorption at needs to be less than 20 ppm/cm at the chosen laser wavelength. This requirement comes from the maximum radiative cooling capacity of the mirrors (~10 W) and the estimated coating absorption of 3 W.
  - **Mirror surface roughness:** Figure error and microroughness need to satisfy the cavity loss requirement of 10 ppm per bounce (together with the coating scatter loss). See Appendix E.1 for details.
  - **Substrate homogeneity:** Inhomogeneity of the index of refraction in the ITMs is a source of contrast defect, which mainly impacts the squeezed field injected from the dark port. This has not yet been characterized or modeled for silicon, where the inhomogeneity is likely to be in the form of voids or defects in the crystal.

  - **Substrate phase noise:** The ITM substrate should not create phase noise greater than the target sensitivity. The effect of the substrate phase noise is reduced by a factor of the round-trip number ($2F/\pi$, where F is the arm finesse). The known sources of substrate phase noise are thermo-refractive noise and carrier density fluctuation. There may be more unknown noise processes, so the phase noise has to be confirmed by a phase noise interferometer experiment. Assessing the unknown substrate noise is a major goal of Mariner (the Voyager prototype under development now).

- **Coating**

  - **Coating absorption:** The coating absorption must be $\lessapprox 2$ ppm. Limited by total radiative cooling power as above.
  - **Coating scatter loss:** The coating scatter loss target is 10 ppm per bounce (together with the loss due to the surface roughness). See Appendix E.1.

- **Thermal engineering:**

  - Barrel/Face coating and fins for radiative cooling need to be applied.

- **Other requirements:**

  - Birefringence of the substrate and coating needs to be low, so as not to cause additional optical loss and noise by splitting of the cavity resonant modes.
  - Similar to the above, second harmonic generation in coatings needs to be low.

3.2.2 Mechanical Requirements

- **Large size test mass availability:**

  The Voyager design employs large silicon test masses that weigh ~200 kg. The availability of such a large and pure silicon substrate is discussed in Section 3.3.1.

- **Mechanical quality factors:**

  - The substrate loss angle needs to be low at the test mass cryogenic temperature.
  - The HR coating mechanical loss needs to be low as well. This is discussed in Section 3.3.2.
  - The barrel and face coatings, and fins for radiative cooling, should not create too much mechanical loss.

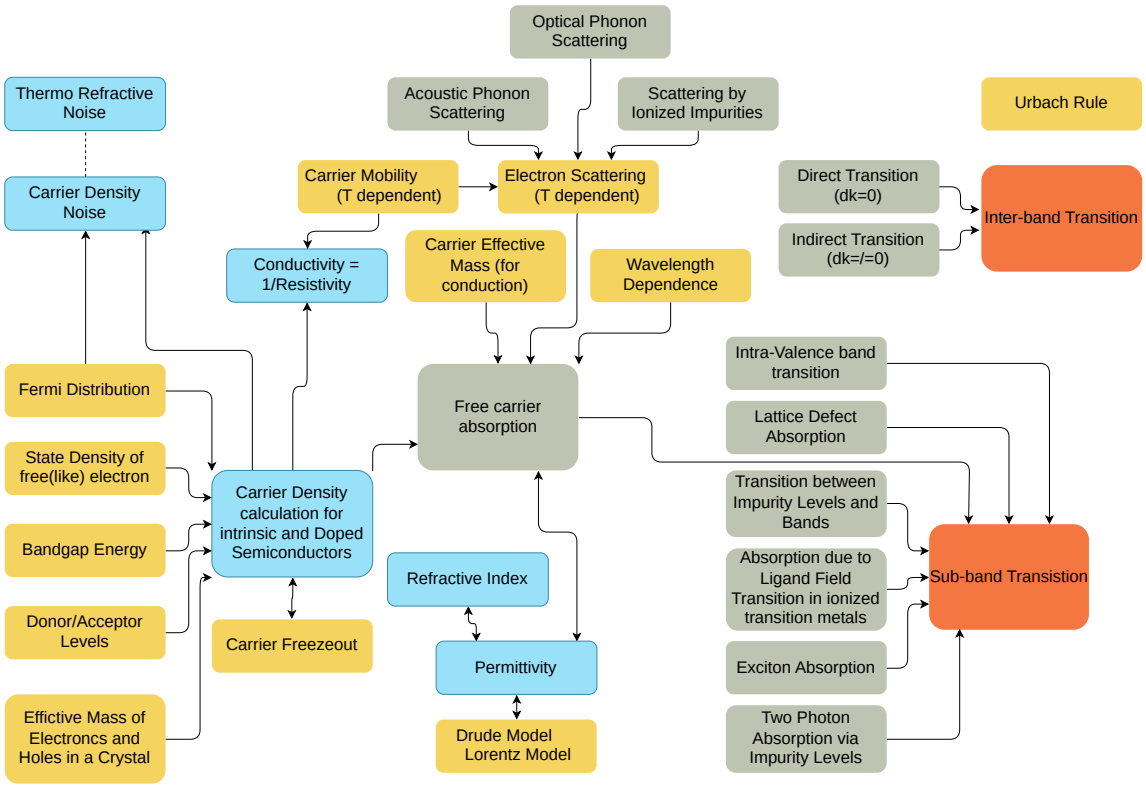

FIGURE 5: Silicon Mind Map illustrating interconnections of issues related to processing of silicon for low absorption, low optical scattering, and mechanical loss.

3.3 Technical Details

3.3.1 Test Masses

The baseline design is to use ~200 kg mono-crystalline silicon as the substrate for the arm cavity mirrors. The test mass needs to meet demanding mechanical and optical requirements.

The requirements are straightforward to meet with float-zone (FZ) silicon [42], but FZ silicon is limited to boules of 20 cm diameter by the surface tension of silicon. Our baseline is to use magnetic Czochralski (MCZ) silicon which has been grown in 45 cm boules since ~ 2010 [87] by several manufacturers. The 45 cm process is not yet the industry standard, but boules and wafers with low defect count exist.

Silicon is considered to be a promising material for the Voyager test mass material as it can be made with high purity, large size, and high mechanical Q. Here we discuss practical points with regard to the silicon test mass.

Substrate absorption Silicon has many mechanisms for optical absorption. Fig. 5 shows a concept map of the silicon substrate absorption at near-infrared wavelengths. Here we summarize some of the major absorption processes that are still simple enough to consider.

Inter-band absorption The basics of the inter-band absorption in silicon are described in Schinke, et al. [124]. Absorption of light in silicon is a direct transition above 3.4 eV (365 nm), but at the near-IR wavelengths of interest, the fundamental inter-band absorption process is an indirect transition.

In an indirect transition, a valence band electron needs to acquire energy and momentum at the same time to be excited to the conduction band, which is about 1.1 eV above. Therefore, the inter-band excitation can only occur with assistance from a phonon, as the photon carries very little momentum in relation to its energy.

Schinke, et al [124] measured the absorption coefficients using four different measurement methods, and compared them with previous measurements in order to determine the coefficient for the inter-band absorption. Fig. 6 shows their result. We should bear in mind that their absorption measurement above 1100 nm was indirect (i.e. photoluminescence or photoelectron measurement), and its relevance to our application is still questionable. We need to consider electron loss processes in the bulk, like electron-hole recombination. The absorption below 1100 nm (thus above $\alpha >\sim 10^0$) is relevant for us, as it was measured by ellipsometry and R&T measurements. The inter-band absorption is also a strong function of temperature. An example measurement of this effect can be found in [139], although there it was measured at 1064 nm, and we still need to seek the information at 1550 nm and 2000 nm.

Experimental efforts to measure the absorption of silicon have been carried out in the context of ET [29, 30]. The absorption in FZ silicon with a resistivity of 10 kΩ cm was found to be 4 ppm/cm [29] at 1550 nm. This result implies that the fundamental inter-band absorption can be smaller than this level, and need not be an issue.

Free Carrier Absorption Both doped silicon and intrinsic silicon have excited carriers in the conduction and valence bands. Due to the finite temperature, the carriers are thermally excited and become unbound. These free(-like) carriers move in response to an external optical field, causing optical absorption. This process is called *free carrier absorption* (FCA).

The calculation of the free carrier concentration for intrinsic and doped silicon, as well as the free carrier absorption based on the simple Drude model are described in T1500619. The free carrier concentration of intrinsic silicon is $10^{10}/cm^3$ at 300 K, and $3 \times 10^{-6}/cm^3$ at 120 K. The FCA resulting from such low carrier densities is negligible. However, free carriers from trace impurities typically dominate over the intrinsic free carrier population. For lightly doped silicon, the free carrier concentration is basically determined by the doping concentration. The calculation tells us that "free carrier freeze out" (i.e. reduction of the free carrier concentration at cryogenic temperatures) does not happen at 123 K when the doping concentration is low ($< 10^{16}/cm^3$). It was estimated that a doping concentration of 10^{13} (corresponding to a resistivity of ~ 1kΩcm) causes FCA of several ppm at 1550 nm, increasing at longer wavelengths as λ^2.

Pankove [114] suggested that the actual FCA process is more complicated. Processes like

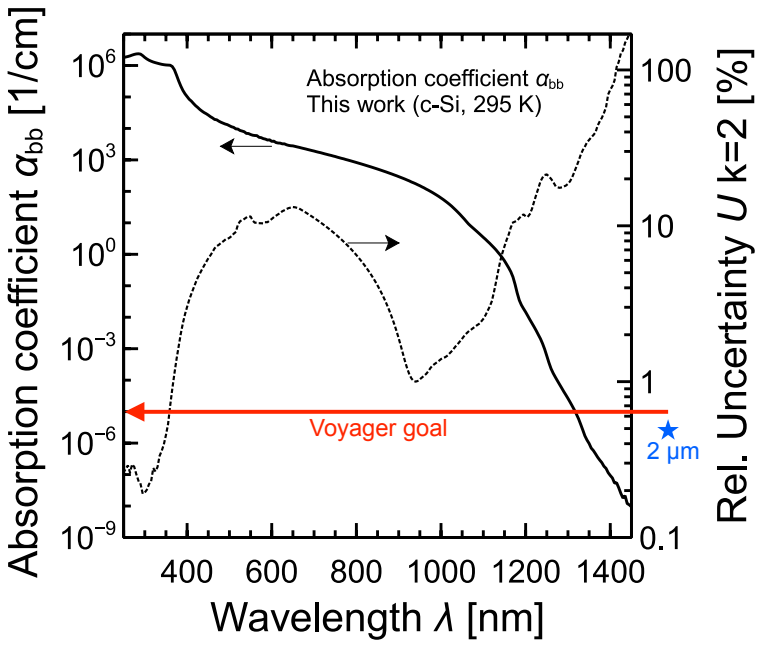

FIGURE 6: Inter-band absorption in Silicon as a function of wavelength [124]. The measurement has been done *directly* below 1100 nm, relevant for our purposes. Above 1100 nm, the measurement was electro-optically done. The red line corresponds to the Voyager bulk absorption goal, and the blue star indicates the lowest bulk absorption seen near 2000 nm in MCZ silicon [94].

lattice scattering by acoustic phonons, by optical phonons, and by ionized impurities can cause the absorption to scale as $\lambda^{1.5}$, λ^2, and $\lambda^3 \sim \lambda^{3.5}$, respectively.

The measurement of 4 ppm/cm [29] loss at 1550 nm was much higher than the FCA level expected from the simple Drude model and the high resistivity of their silicon sample. It was suggested that the presence of an absorption band in n-type silicon centered around 2300 nm could be the reason for this excess. Spitzer and Fan [134] experimentally showed that this absorption band has a height of $\alpha \sim N/10^{17}/cm$, as a function of doping concentration N/cm^3. The height of the band was only weakly dependent on temperature down to 5 K. Since we are especially interested in the absorption limits near 2000 nm, this finding should be further investigated.

A theoretical model of free carrier absorption in silicon was presented by Tsai [151], building on the work of Ridley [121]. This model offers a physical motivation for the Spitzer-Fan absorption feature, in terms of the conduction band structure in silicon. However, it is rather cumbersome and depends on numerous material parameters, some of which are not tightly constrained.

Many simple empirical models for free carrier absorption have been devised. The formula of Schroder, Thomas, and Swartz [126] (STS) follows the Drude λ^2 dependence:

$$\alpha_{\mathrm{STS}} = 10^{-18}\lambda^2(n + 2.7p) \tag{1}$$

given in units of cm^{-1}, with λ the wavelength in microns, and n, p the electron and hole densities in cm^{-3}. Another formula, due to Green [54], attempts to fit the Spitzer-Fan

excess absorption near 2 microns with a λ^3 dependence:

$$\alpha_{\text{Green}} = 10^{-18}\lambda^2(2.6\lambda n + 2.7p) \tag{2}$$

Both the STS and Green formulas are based on data from highly doped silicon ($> 10^{16}\text{cm}^{-3}$).

Degallaix et al [29] fit their 1.55 µm data for high resistivity FZ silicon to yet another formula:

$$\alpha_{\text{Degallaix}} = 0.0454/\rho \tag{3}$$

where ρ is the resistivity of the n-type silicon in Ω cm. This agrees well with α_{Green} at 1.55 µm.

The temperature dependence of the free carrier absorption remains unclear. From the Drude model, some improvement might be expected with cooling due to increased carrier mobility, even if the carriers do not "freeze out" at 123 K. Yet, measurements of low-absorption samples have shown little change, or a modest increase in absorption between 300 K and 123 K.

Other Processes Another noteworthy absorption process is multi-photon absorption. It was experimentally [17, 38] and theoretically [26] shown that two-photon absorption (TPA) of silicon has a strong dependence on the laser wavelength in the near infrared region. These papers reported that the TPA coefficient, β, of silicon at 300 K were $0.5 \sim 0.8\,\text{cm/GW}$ and $\sim 0.2\,\text{cm/GW}$ at 1550 nm and 2000 nm, respectively. β has temperature dependence because of phonon assisting involved in the absorption process. This dependence is not too strong to change the order of magnitude. Also, β is even reduced as the substrate is cooled [26, 153]. Therefore, the absorption coefficient here is estimated with the experimental data measured at 300 K. Assuming 10 kW of laser power through a spot area of $\sim 300\,\text{cm}^2$, this gives us a power density (P_{dens}) in the substrate to be $30\,\text{W/cm}^2 = 3 \times 10^{-8}\,\text{GW/cm}^2$. Therefore, the absorption coefficient due to TPA at 2000 nm and 300 K is estimated to be $\alpha_{TPA} = \beta P_{\text{dens}} = 6 \times 10^{-9}\,\text{cm}^{-1}$. This is a negligibly small number. Three-photon absorption (3PA) can also be a source of absorption. The 2000 nm light can be upconverted to a visible wavelength whose photon energy is larger than the bandgap of silicon. In fact, the measurement of the 3PA coefficient by [141] shows a strong peak at a wavelength of 2600 nm. Nevertheless, the reported 3PA coefficient by [115] is on the order of $\gamma = 0.03\text{cm}^3/\text{GW}^2$ at 2300 nm at 300 K. This corresponds to an absorption coefficient of $\alpha_{3PA} = \gamma P_{\text{dens}}^2 = 3 \times 10^{-17}\,\text{cm}^{-1}$. This is also a totally negligible number.

Availability of Large Silicon Substrates It seems likely that 45 cm diameter pieces can be acquired from CZ or MCZ process with a resistivity greater than $1\,\text{k}\Omega\,\text{cm}$. The absorption and bulk mechanical loss measurement of the silicon of such samples is crucial. An absorption as low as 2 ppm/cm has been measured in un-annealed MCZ silicon, with some evidence of a radial increase in absorption.

Oxygen and annealing Rapid annealing of MCZ silicon wafers to ~700 °C or higher is routinely done in order to annihilate oxygen clusters (known as "thermal donors") that contribute to free carrier absorption [53, 78, 86, 99]. A sufficiently rapid anneal of a bulky sample such as a test mass substrate has not been demonstrated, but may be feasible, based on the following considerations:

- Large temperature gradients in the test mass during an anneal are undesirable, because they may lead to optical non-uniformity or defects. An in-air or in-vacuum anneal to 700 °C is estimated to produce modest (though non-negligible) temperature gradients.

  The Biot number, defined as $\mathrm{Bi} = \frac{h_{\mathrm{heat}}}{\kappa} L_c$, characterizes the uniformity of the temperature distribution inside the test mass. Here h_{heat} is the surface heat transfer coefficient, κ is the thermal conductivity, and L_c is the ratio of volume to surface area ($\approx 8\,\mathrm{cm}$ for the test mass). If $\mathrm{Bi} \ll 1$, the temperature distribution can be regarded as uniform.

  Convection in air can give rise to $h_{\mathrm{air}} = 10 - 100\,\mathrm{W\,m^{-2}\,K^{-1}}$, while radiative transfer leads to $h_{\mathrm{rad}} = \epsilon\sigma(T_1^2 + T_2^2)(T_1 + T_2) \lesssim 230\,\mathrm{W\,m^{-2}\,K^{-1}}$. In silicon, κ ranges from $130\,\mathrm{W\,m^{-1}\,K^{-1}}$ at room temperature to $\sim 30\,\mathrm{W\,m^{-1}\,K^{-1}}$ at 700 °C.

  Combining these figures, Bi is bounded $\lesssim 1$ up to 700 °C.

- To annihilate thermal donors, while avoiding the creation of "new donors", the test mass must dwell only briefly (at least a few minutes, but probably less than an hour) near the peak temperature of 700 °C [53]. To avoid regenerating oxygen thermal donors, it must rapidly cool down from 500 °C to 400 °C (within an hour, perhaps) [86].

  These time scales are roughly compatible with the rate at which the test mass can heat up and cool down in air. Approximating the test mass as a lumped element with uniform temperature, mass M, surface area A, specific heat $c_M \approx 800\,\mathrm{J\,kg^{-1}\,K^{-1}}$, and heat transfer coefficient $h_{\mathrm{heat}} \approx 100\,\mathrm{W\,m^{-2}\,K^{-1}}$, the thermal time constant $\frac{M c_M}{h_{\mathrm{heat}} A}$ is $\sim 24\,\mathrm{min}$.

A thermal model with convective heat transfer of $h_{\mathrm{heat}} = 100\,\mathrm{W\,m^{-2}\,K^{-1}}$ has been constructed in COMSOL (see Fig. 7) and is consistent with the analysis above. However, radiative effects should also be considered, so as to design an annealing schedule and ensure that the requirements can be satisfied. Moreover, a tighter constraint on annealing may stem from the requirement to avoid plastic deformation due to thermal stress, which would introduce birefringence. These same requirements also apply to any subsequent anneal of the reflective coating.

Rapid annealing to annihilate oxygen clusters might not be necessary, if MCZ silicon with ultra-low oxygen content [71] can be grown at the 45 cm size.

Modify the Test Mass Geometry Although we have historically chosen an optimum test mass geometry (in terms of the ratio of thickness to width), this is a soft optimum

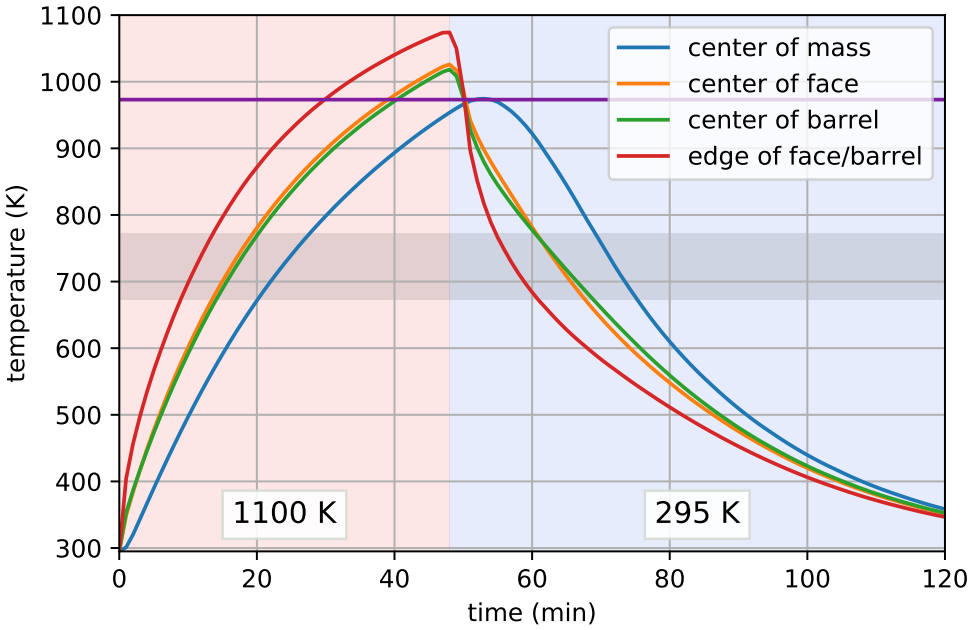

FIGURE 7: Simulated anneal of a test mass in COMSOL. The test mass is heated in a 1100 K oven for 48 min, then allowed to cool to room temperature, all under convective heat transfer $h_{\text{heat}} = 100\,\text{W}\,\text{m}^{-2}\,\text{K}^{-1}$. Temperature gradients of up to 200 K form between the center of the mass and its outer edges. The purple line indicates the 700 °C target of the anneal, and the grey region corresponds to peak thermal donor formation.

and we could explore increasing the thickness of the mirrors in order to gain the required mass.

This has the added benefit of increasing the barrel surface area (which is the primary actor in the radiative cooling capability of the mirrors).

Fig. 8 shows the Brownian noise of a single ETM as a function of the mirror thickness. Although there is an optimum for the substrate noise, it is *completely insignificant* compared to the coating noise, which has no local minimum. Increasing the test mass thickness has no deleterious effect on the thermal noise, but does reduce the quantum backaction noise by virtue of increased overall mass.

3.3.2 Test Mass HR Coatings

There are various options for the test mass mirror coatings. Here we describe some considerations and explain why we have chosen α-Si : SiN as the baseline configuration.

Amorphous Silicon Amorphous silicon has great mechanical properties [84, 106, 117]. It is one of the lowest mechanical loss thin films ever measured, and continues to improve due to intense development in thin films labs.

In addition, the high index contrast with Silicon nitride (3.5 : 2.17) makes it possible

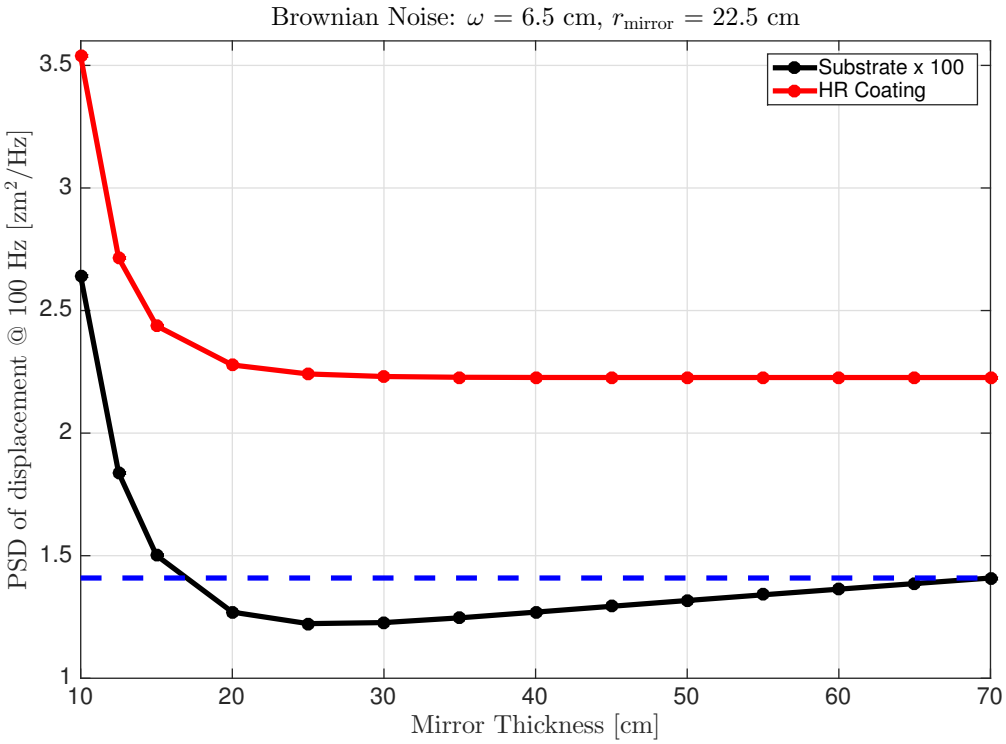

FIGURE 8: Substrate and Coating Brownian noise as a function of mirror thickness. T = 123 K, mirror diameter = 45 cm, ω_{beam} = 6.5 cm. The substrate PSD has been multiplied by 100 to match the y-axis scale.

to use a smaller number of layers than in aLIGO, while achieving the required high reflectivity. The optical absorption is high (~10 ppm), but has come down by orders of magnitude in the past few years. Some analysis of a candidate coating design using alternating layers of α-Si : SiN is given in Appendix D.

3.3.3 Recycling Cavity Optics

The SRC length fluctuations couple to DARM much more than PRC motion since it acts chiefly on the differential mode, and so here we will just concentrate on MICH & SRC noise and assume that it covers the case for the PRC. The baseline design is that all optics, except for the ITMs, ETMs, and their respective PUMs, will be at room temperature. This is possible since the noise from those optics couples into DARM ~100x less than the test masses. The PRC and SRC optics are planned to be made out of either a standard silica, or one of the silica grades with reduced 2 micron absorption. As of this writing, The Corning 7979 and Heraeus Spectrosil 2000 both have low absorption at 2 microns, but are still unsuitable for our requirements.

Beamsplitter The main IFO Beamsplitter has similar noise requirements to the SRC optics, but also lives in the PRC and so it must handle high power. There seems to be no available glass with a low enough absorption, except perhaps chalcogenides or ZBLAN, but they have thermal noise issues.

Considerations applicable to the beamsplitter design include:

1. A high-power laser beam traverses through the beamsplitter.
2. The beamsplitter's motion contributes to L_- through the MICH & SRC.
3. Bulk index fluctuations in the beamsplitter do not cancel out in the L_- readout.

Here are the list of high priority considerations for using room temperature silicon as the beamsplitter:

1. Which crystal axis is the best for 45 deg angle of incidence? <111> aligned to input beam from PRM sounds reasonable, but are there issues with fabrication?
2. What kind of measurements are necessary to determine this?
3. Contributions from "birefringence noise" reported from JILA/PTB group [163].

Below are the list of low priority considerations:

1. Controls issues, optical losses, contrast defect simulations from (inhomogeneous) birefringence (also necessary for ITM at cryogenic temperature)
2. Thermal lensing calculations (similar to ITM, but silicon properties will be at room temperature for BS)

Below are the list of considerations already addressed:

1. Beam shift from static birefringence is negligible G2200695.
2. Noise coupling to the beamsplitter roll mode, polarization rotation of the laser beam seems negligible T2200272.
3. Substrate Brownian and substrate thermo-elastic noises are small enough. However, thermo-refractive noise will be as large as that from ITM (see Fig. 9 and Table 15). Note that in this calculation, BS thickness is assumed to be the same as ITM, which is a pessimistic assumption. Also, noise from ITM is a combination of noise from ITMX and ITMY, and BS also has sqrt(2) factor from 45 deg angle of incidence.

3.4 Unresolved issues

Known issues that must be resolved in preparation for manufacturing the Voyager test masses are graphically summarized in Fig. 10, and include the following:

- Is it feasible to obtain 45 cm MCZ silicon crystals that meet the Voyager requirements? Alternatively, can a composite test mass be assembled from smaller crystals?
- Will the oxygen impurity in the silicon be high enough to result in excessive substrate absorption? If so, can the rapid annealing technique be applied on large crystals to remedy the problem? Can a subsequent coating anneal be designed so as to improve the coating properties without spoiling the substrate absorption again?
- Which combination of coating materials can achieve the absorption requirement with minimal thermal noise?

3.5 Development Approach & Timeline

- Substrate material: 45 cm MCZ
  - Optimize composition and process (target low absorption, scatter, index inhomogeneity, and birefringence)
  - Develop 2 µm cryo metrology
  - Alternative: Use 20 cm FZ silicon and develop composite test mass bonding
- Polish: select polisher
- HR/AR coatings: SiN:aSi
  - Optimize composition and process (target good adhesion; low absorption, scatter, and loss angle; high emissivity; anneal compatibility with substrate)
  - Alternative: Develop non-binary coating design or AlGaAs bonding

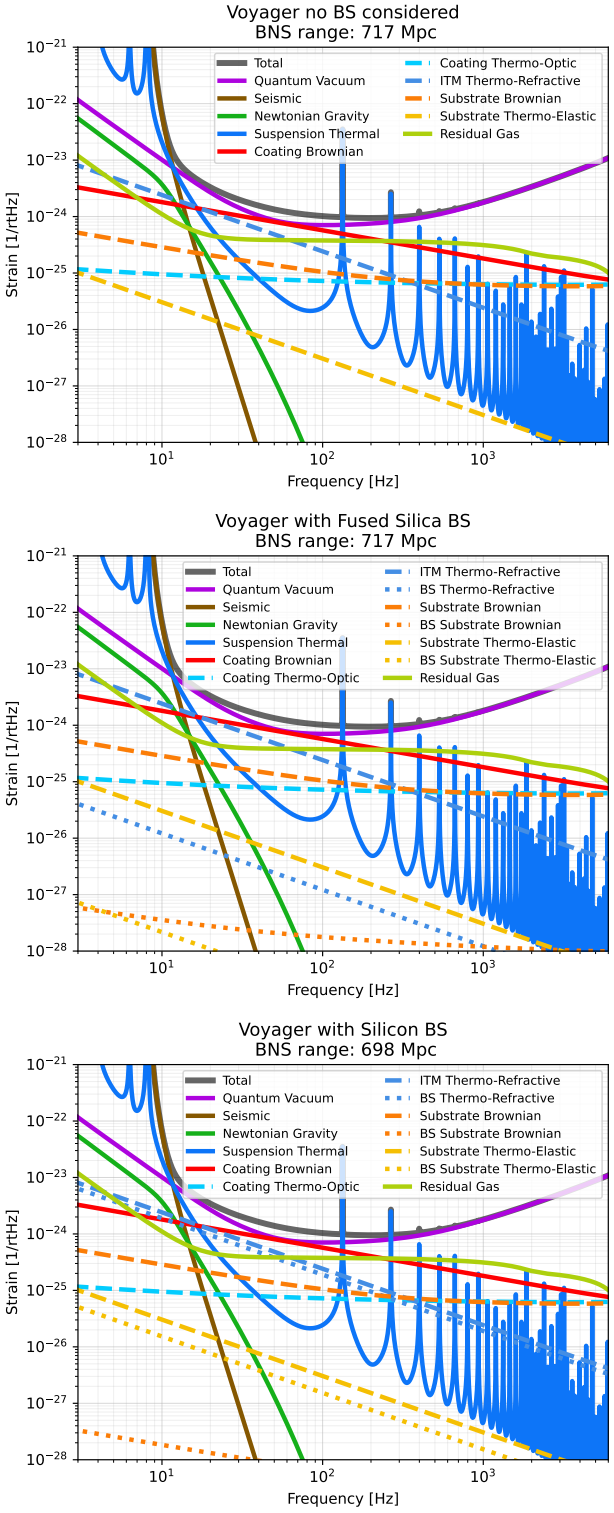

FIGURE 9: Voyager sensitivity curves with silicon BS and fused silica BS.

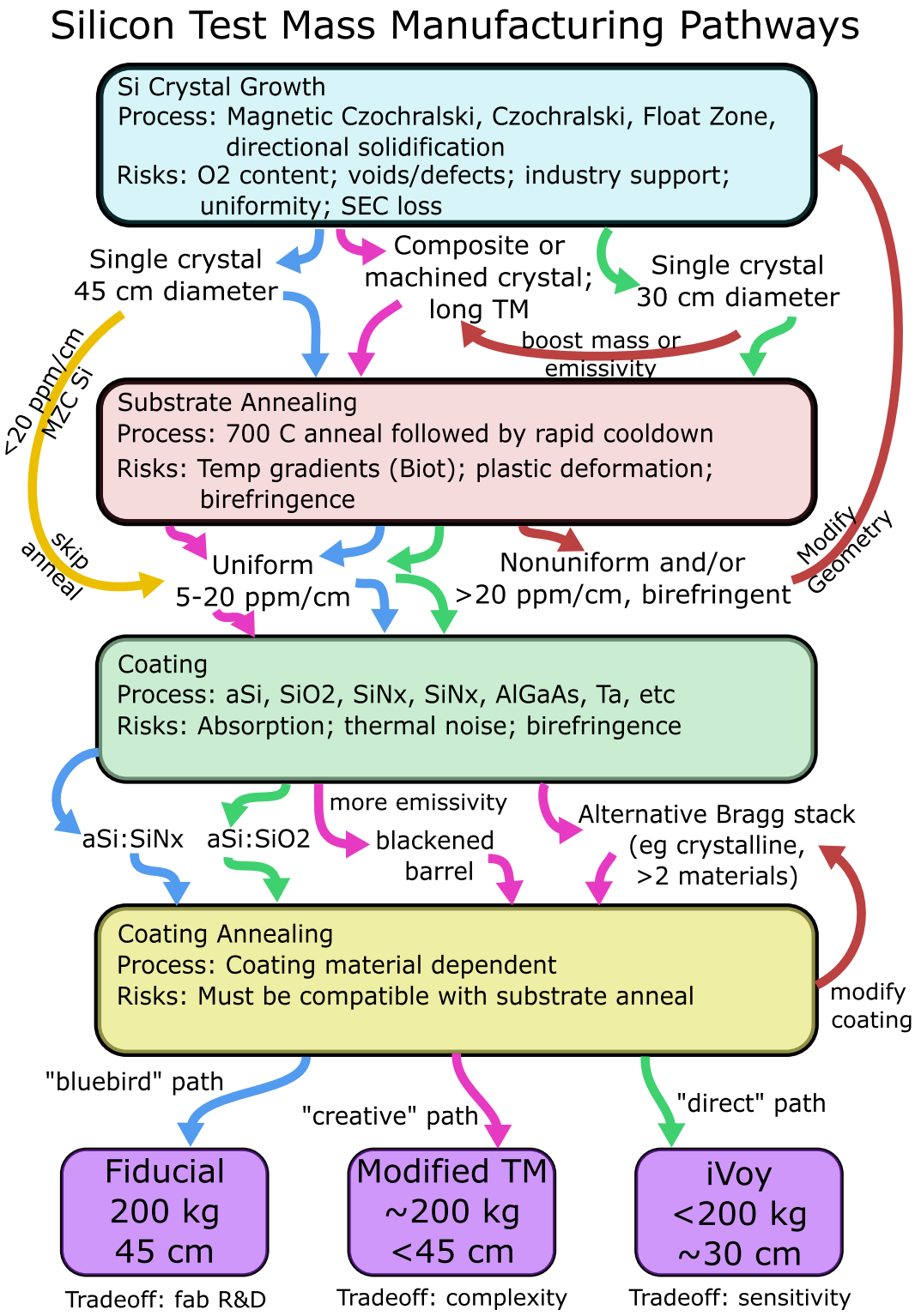

FIGURE 10: Potential pathways to meet requirements for silicon test masses. The blue arrows indicate the simplest choices of test mass and coating design assuming optimistic outcomes for process research and development; green arrows indicate a relatively low-risk pathway to achieve a functional initial Voyager; magenta arrows show some ways of circumventing obstacles that may arise while developing the "bluebird" pathway.

4 Cryogenic System

4.1 Overview

In this section, the system used to maintain the test masses at their 123 K low temperature operating point is described[2].

Two options exist for the PUM temperature, cold and warm; with a couple different suspension configuration possibilities in each case. See Fig. 11, which shows the cold PUM configuration. The related Fig. 12 shows a CAD model of certain components of the end station vacuum system. Appendix I summarizes these configurations, and the downselection choice to utilize the nominal silicon cold PUM configuration with silicon ribbons or fibers.

Within the GW field, there are several examples of using cryogenic cooling to improve the sensitivity of detectors:

1. CLIO [162]: a short cryogenic underground laser interferometer in Japan
2. KAGRA: the 3 km Japanese underground gravitational-wave observatory
3. Several resonant mass GW detectors: ALLEGRO, NIOBE, NAUTILUS, etc.
4. Rigid cavities: Caltech, JILA, PTB, Dusseldorf, etc.

In Section 4.2, we describe the thermal and noise requirements for the cryogenic system. In Section 4.3, we describe the technical details of steady-state radiative cooling of the test mass, the high emissivity coatings, and the transmission monitor. In Section 4.4, we discuss unresolved issues and work to go. In Section 4.5, we discuss the planned development timeline.

4.2 Requirements

4.2.1 Target Temperature

A target temperature of 123 K is selected due to the zero crossing of the CTE, which minimizes thermo-elastic noise. Fig. 13 shows how the variation of the CTE with temperature degrades the predicted strain noise. Increased substrate thermo-elastic noise is responsible for most of the degradation. Maintaining the temperature at the operating point within ±1 K appears sufficient, with margin, for avoiding this excess noise.

4.2.2 Temperature Fluctuations

To investigate the effect of temperature fluctuations on the noise, the derivative of the Voyager strain noise curve with respect to each material parameter in the GWINC noise

[2]The cooldown process by which they are brought to that operating point after each vacuum incursion is described in Appendix G.

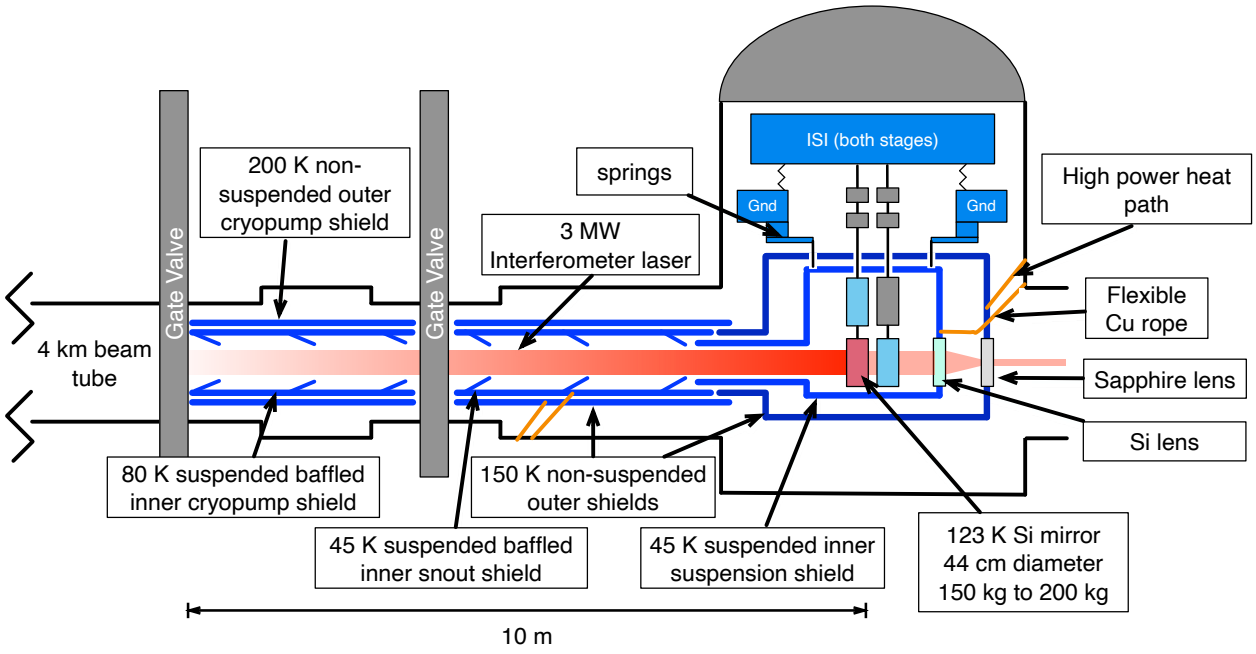

FIGURE 11: Layout of the ETM suspension in the cold PUM configuration with the cryogenic cooling elements. The test mass and reaction mass are cooled radiatively with a two layer heat shield system. The inner shield may require vibration isolation to mitigate scattered light noise. Suspending it from springs achieves this isolation above a few Hz. Active displacement feedback referenced to stage 2 of the ISI can achieve isolation below a few Hz if necessary. The outer shield is cooled with a high power thermal link while the inner is cooled with a lower power but flexible link. The inner shield is designed to reach 45 K, and the outer shield is designed to reach 150 K. Note that the ends of the snouts (away from active cooling) are marked at higher temperatures to account for temperature gradients.

model has been computed. These parameter sensitivity curves are plotted in Fig. 14. The main message to take away from the plots is that the curves are of order unity or smaller at all frequencies. Thus, modest changes in the parameters produce modest changes in the predicted strain noise.

To obtain the overall sensitivity to temperature fluctuations, each parameter sensitivity curve has to be weighted by the sensitivity of its parameter to temperature. Parameters that have a known temperature dependence are compiled in Table 2.

In general, the material parameters are only weakly sensitive to temperature fluctuations. The exception is the silicon CTE, which is extremely sensitive by design, since Voyager's operating point is tuned to be near a CTE zero crossing.

Some open temperature fluctuation questions are listed in Section 4.4.

4.2.3 Newtonian Gravitational Noise from Heat Shields

The test masses will be radiatively cooled to 123 K by inner thermal shielding at 45 K (see Section 4.3 for technical details). The geometry of the heat shields should be considered in case Newtonian noise coupling is problematic (cf. design of the STEP exper-

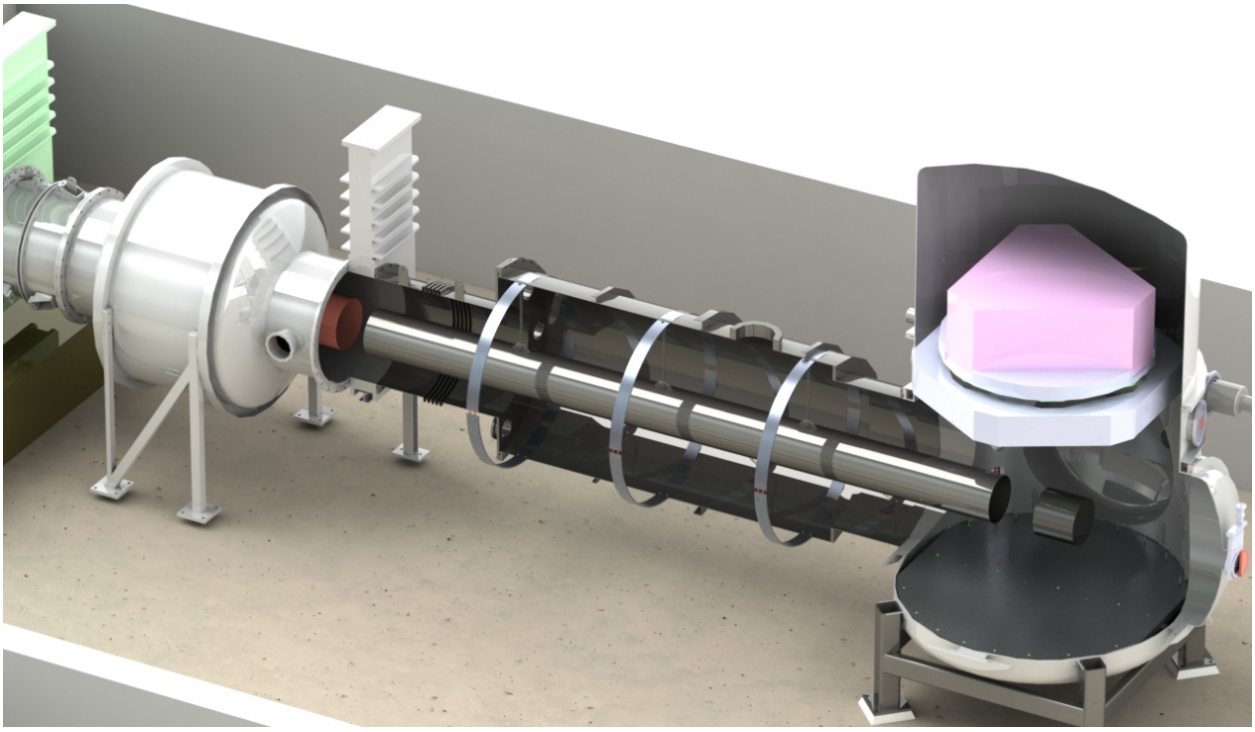

FIGURE 12: CAD drawing of end station vacuum system. Outer shield, Mirror shield, reaction chain, and suspension cage structure *not shown* for clarity.

iment [85]). Simulations done by E. Bonilla on plausible heat shield geometries and vibration levels suggest this Newtonian Noise source is not likely to be problematic. However, if liquid nitrogen is used in pipes near the test mass (which is not in the baseline design), and that nitrogen has 2-phase flow, then Newtonian Noise from this flow may be a problem. Chilling the nitrogen below its boiling point is a relatively easy and promising way to mitigate this 2-phase flow Newtonian Noise source, but it requires more investigation. Newtonian Noise simulations are summarized in G1700404 and P2100273.

4.2.4 Backscatter from Heat Shields

As observed in the early aLIGO science runs, the effects of backscattering near the test masses can be orders of magnitude larger than the phase noise due to quantum or thermal noise. Care must be taken in designing the inner shields near the test mass to minimize backscattering of the laser light.

The shields will be cooled through cold straps, which will contribute some seismic noise coupling. A calculation by D. Coyne of acoustic coupling through cables derived in T060038, and applied to cables in aLIGO HAM1 in T1300128, should be extended to inform the design of the thermal straps and their mounting. Evaluation of several types of copper braid seems promising; it seems likely that the use of several straps will allow for sufficient cooling power for both the external and internal shields without compromising the vibration isolation performance. To be confirmed by measurement, but it

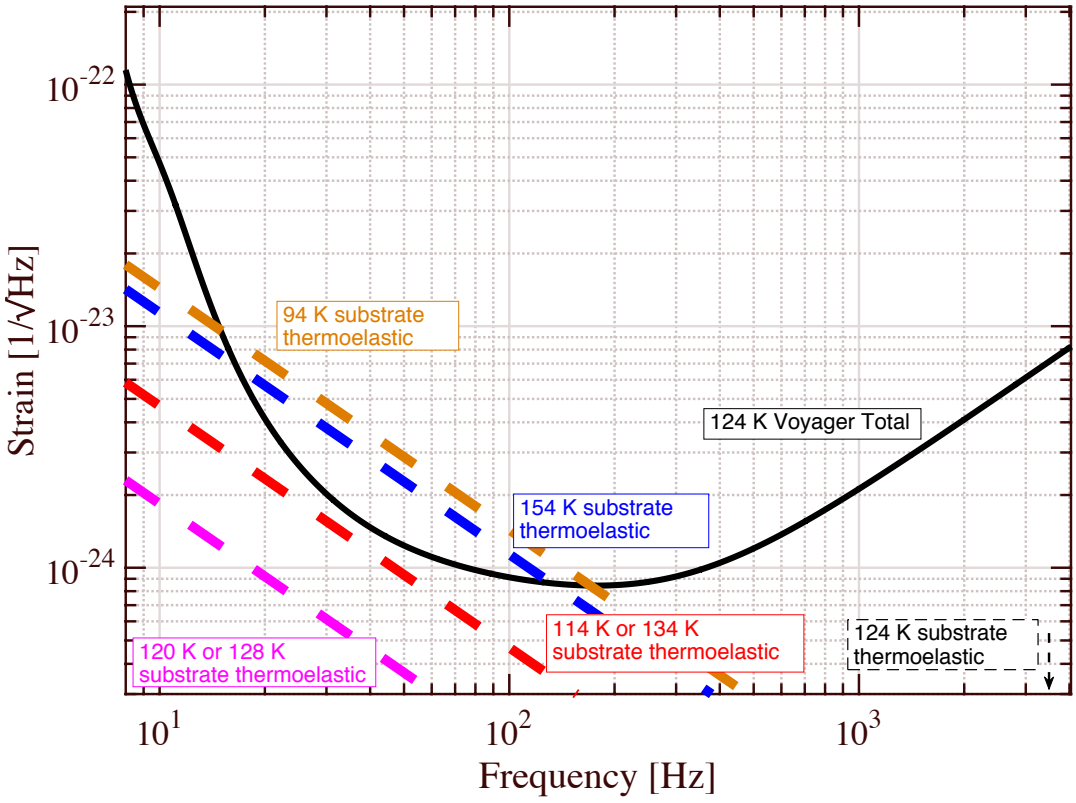

FIGURE 13: Substrate thermo-elastic noise due to variation of the silicon CTE at temperatures away from the designed operating point.

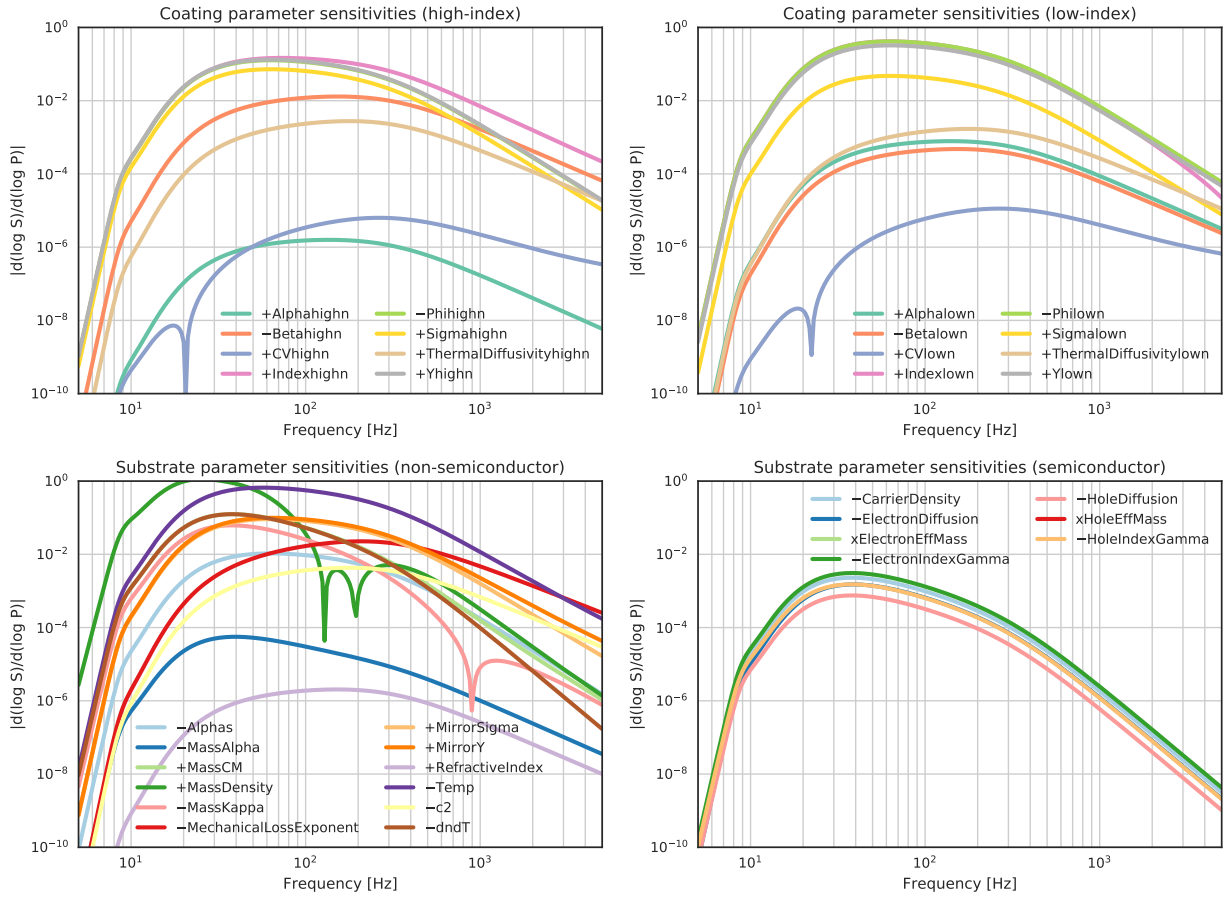

FIGURE 14: Sensitivity of the GWINC noise model to material parameters. For definitions of the variable names, see Table 2. The +/− signs in the legend indicate the direction of parameter deviation that would improve the noise.

Parameter P	Variable name	Nominal value	$d(\log P)/d(\log T)$	Ref
temperature	Temp	123 K	1	
c-Si CTE	MassAlpha	$1.0 \times 10^{-9}\,\mathrm{K}^{-1}$	2100	[74]
c-Si specific heat	MassCM	$300\,\mathrm{J\,K^{-1}\,kg^{-1}}$	1.3	[149]
c-Si thermal conductivity	MassKappa	$700\,\mathrm{W\,K^{-1}\,m^{-1}}$	−1.6	[150]
c-Si Young's modulus	MirrorY	156 GPa	−0.0034	[55]
c-Si refractive index	RefractiveIndex	3.5	0.0032	[44]
c-Si thermo-optic coefficient	dndT	$100 \times 10^{-6}\,\mathrm{K}^{-1}$	0.90	[44]
a-Si CTE	Alphahighn	$1.0 \times 10^{-9}\,\mathrm{K}^{-1}$	2100	[74]
silica CTE	Alphalown	$2.6 \times 10^{-6}\,\mathrm{K}^{-1}$	0.25	[108]
silica volume-specific heat	CVlown	$230\,\mathrm{J\,K^{-1}\,m^{-3}}$	0.49	[108]
silica thermal conductivity	ThermalDiffusivitylown	$270 \times 10^{-3}\,\mathrm{W\,m^{-1}\,K^{-1}}$	0.40	[108]
silica Young's modulus	Ylown	270 GPa	0.022	?
silica Poisson ratio	Sigmalown	0.25	0.034	?

TABLE 2: Selected material parameters and their sensitivity to temperature fluctuations.

now seems that *no liquid cryogen will be required inside the vacuum system*.

Appendix E.5 provides a discussion and preliminary estimates of the contribution of scattered light noise to the interferometer.

4.3 Technical Details

4.3.1 Test Mass Radiative Cooling

The test masses will be cooled to a target temperature of 123 K using a free piston Stirling style cryocooler. The down-select for this style is discussed in Appendix H. The input heat load from the environment and from the laser heating must be balanced with cooling of the test masses, primarily through radiative coupling. Fig. 15 illustrates the heat flow paths.

A full model of the heat balance of each ITM and ETM includes:

- Heating
  - absorption (2 μm) from the main laser into the HR coating and substrate
  - radiation from the 295 K beam tube into the HR coating and substrate
  - radiation from the 80 K reaction mass into AR coating and substrate
  - radiation from the 45 K cold shield into HR coating and substrate
  - incident radiation from TCS
- Cooling
  - radiation from the HR coating
  - radiation from the AR coating

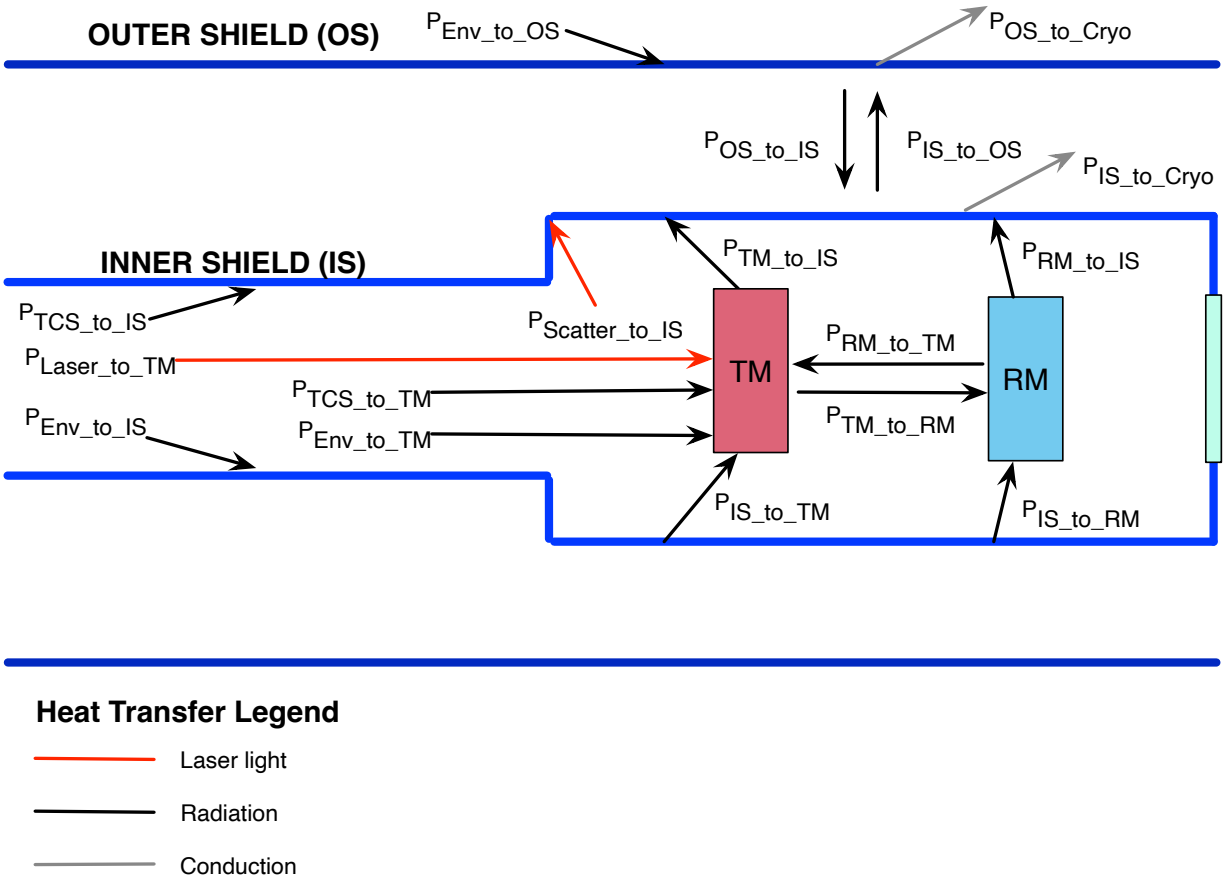

FIGURE 15: Schematic of the heat flow inside an end station vacuum chamber. Heat transfer through the ribbons/fibers is assumed negligible. TM refers to the end test mass, RM the reaction mass. Red arrows are heat transfer from the laser light, black radiation, and gray conduction. The heat transfer from the inner shield to the outer shield is radiative. Fig. 11 shows the overall layout.

- radiation from the high emissivity mirror barrel coatings
- thermal conduction up suspension ribbons (very insignificant)

A calculation by Rai Weiss (T1200093) shows that a silicon test mass with a high emissivity coating on the barrel can radiate > 3 W at a temperature of 123 K. Fig. 16 shows that this can actually be 7 – 9 W, depending upon assumptions about the wavelength dependent emissivity of our HR and AR coatings. Although the Acktar black coating is known to have a high emissivity and a low mechanical loss [4], at the moment the effective emissvity of the HR and AR coatings is not known. Since these coatings are much thinner than the low temperature blackbody peak (~ 30 μm), one needs to consider the interference effects.

The grey body radiation of a silicon test mass is non-trivial to compute, and ray-tracing models of various silicon geometries is in development.

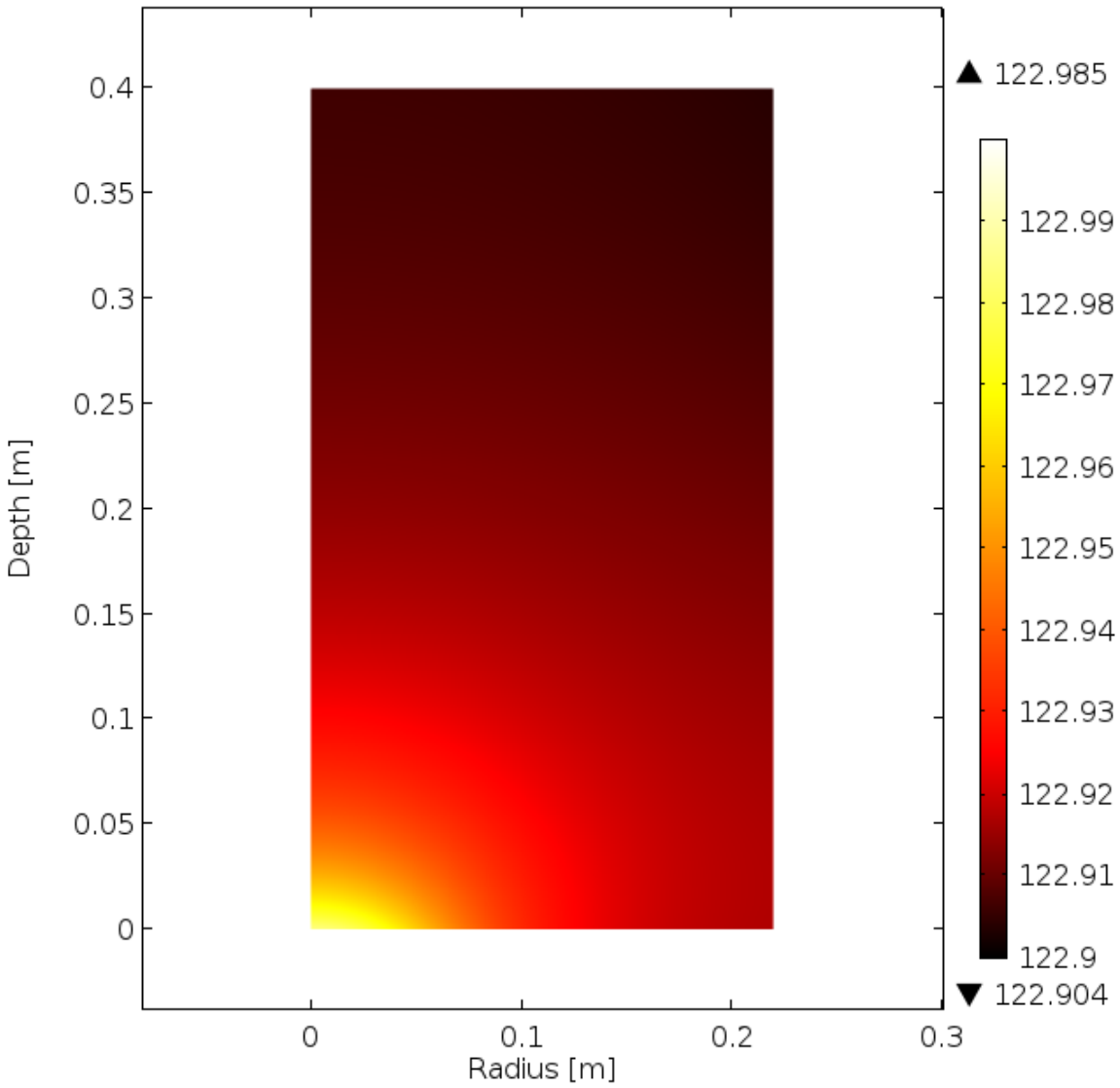

FIGURE 16: FIGURE NEEDS REPLACEMENT. Temperature gradient of silicon test mass. Heating from environment and 10 W absorbed by Gaussian laser beam on HR surface. Radiative cooling to a 45 K cold shield via the mirror barrel surfaces ($\epsilon = 0.95$) and through the HR and AR faces. Emissivity of HR and AR faces assumed to 0.3 as an initial guess. Mirror diameter = 45 cm, thickness = 40 cm, and heat shield temperature = 45 K.

4.3.2 Cryogenic Shielding and Baffling

To minimize the radiative heat load from the 295 K beam tube, the cryogenic shield will need to include a cold tube, or snout, which extends into the manifold tube. See Fig. 11. The above heat load calculations for an ETM assume a snout length of 10 m (15 m for an ITM), and a radius of 0.25 m. These parameters allow the heat load from the 295 K beam tube to be negligible (< 5 mW) in the case of the ETM; however the ITM compensation plate limits its snout length and thus its radiative shielding. The inside of the snout must include baffles, as in the KAGRA design, to reduce multiple reflection paths from the 295 K environment, as well as to minimize backscatter of the high power laser beam from the vibrating cryogenic shield.

The inside of the shield should be made with a high emissivity coating to maximize the radiative coupling to the test mass. However, there is also the consideration of 2000 nm light scattered from the arm cavity into the shield, and then scattered back into the arm cavity. This will be a source of phase and radiation pressure noise, and it is important that the high emissivity coating has a low enough BRDF such that scattered light noise is not significant. Such an effect might be mitigated through the use of a combination of specular baffling and broadband absorption. This was previously analyzed in T950087 for the heat load of the iLIGO cryopumps.

The radiative heat load from the 295 K chamber and vacuum tube onto the cryo shield is so large that a very thick thermal strap would be required to cool the heat shield. The thickness of this strap is not consistent with the vibration induced scattered light noise described in Section 4.2.4.

Instead, a double shield design has been chosen (see Fig. 11). The inner shield will have a much reduced heat load due to:

1. the low emissivity (gold) coating of the outer shield
2. cooling of the outer shield to ~ 150 K
3. the low absorptivity (gold) coating of the outer surface of the inner shield

A full heat load analysis on all chamber components is discussed in Appendix G. Radiative loads on the cold inner shield include:

- Heating
  - radiation from the 295 K vacuum tube and chamber
  - radiation from the 123 K test mass
  - radiation from the 150 K outer shield
  - absorption at 1550 nm/2000 nm from scattering off test mass
  - incident radiation from TCS

- Cooling
  - conduction to the cold head through the copper cold strap

Cooling the outer shield to 150 K significantly reduces its heat load on the inner shield. When held at 150 K, the outer shield radiates 5 times less heat to the inner shield compared to when it is at room temperature. This factor directly translates into a looser cooling requirement for the inner shield, and a thinner thermal strap can be used. A thinner strap combined with a careful choice of a low-vibration cryocooler will meet the vibration requirements described in Section 4.2.4.

Cooling the outer shields is done through a relatively thick copper strap. The vibration requirements of the outer shield are significantly less strict than those of the inner shield because 1) it will not interact optically with the interferometer, and 2) it will be mounted rigidly to the chamber or stage 0 of the ISI. A separate cryocooler or LN2 tank can be used for cooling the outer shield down to 150 K.

Cooling the outer shield by flowing cryogens around it has been proposed as well, for example with cold nitrogen gas or liquid. This has the advantage of being a relatively simple way to get a lot of heat out. However, there are some concerns with this approach, listed below, that result in the current baseline design using copper straps. These concerns are listed roughly in order of most serious to least, with the first item being the driving concern since the other two may have reasonable mitigations.

- Leaks: there is a risk of leaks into the vacuum system, if not a catastrophic bursting of a pipe or joint. A joint failure is more likely than a pipe failure. Additionally, leak hunting becomes more difficult with more sources of potential leaks.
- Vibration: the flow and/or plumbing itself may transmit some vibration. There are some possible mitigations in the geometry of the piping and perhaps by maximizing laminar flow. Boiling of liquid in flowing cryogens could be a source of vibration as well, but this could be mitigated by precooling the liquid below its boiling point [P2100273].
- Newtonian noise: although unlikely, flowing cryogens near the test mass might generate visible Newtonian noise. This issue likely would only arise from 2 phase flow. Therefore, a mitigation would be to ensure single phase by using only cold gas or a liquid cooled below its boiling point. Stanford did some work with LN2 to show that gas can be reduced, if not eliminated, from the flow by chilling it below its boiling point [P2100273].

Next we estimate the size of the various heat balance terms that are expected to be dominant.

4.3.3 Heating from Arm Cavity Laser Beam

The test masses will have some finite absorption both at their high reflectivity coatings (0.5 – 3 ppm) and in the substrate itself (10-20 ppm/cm). Due to the large circulating power in the arms, heating from arm power absorption by HR surfaces will be significant for ETMs and ITMs. However, substrate absorption is only a significant heat load for the ITMs due to the much lower power transmitted through the overcoupled arm cavity. Using Voyager Deep parameters from Section 2, we obtain the following laser heating terms:

$$\begin{aligned} P_{\text{Laser\_to\_ETM}} &\approx P_{\text{cav}}\alpha_{\text{HR}} = 3.92\,\text{MW} \times 1\,\text{ppm} = 3.92\,\text{W}, \\ P_{\text{Laser\_to\_ITM}} &\approx P_{\text{cav}}\alpha_{\text{HR}} + P_{\text{Mich}}\alpha_{\text{sub}} = 3.92\,\text{MW} \times 1\,\text{ppm} + 2.8\,\text{kW} \times 550\,\text{ppm} = 5.46\,\text{W}. \end{aligned} \tag{4}$$

The absorption of laser power in the HR coatings will be the dominant heat load in the test masses and therefore sets the limit for the total laser power available for GW detection.

4.3.4 Heating from Hot Beam Tube

Since no cold window is to be put in the arm cavities (due to scintillation / phase noise issues), the test mass will be partially exposed to the room temperature beam tube. The effect is largely mitigated by a cryogenic shield extending out from the test mass. This shield cannot extend beyond the final gate valve separating the arm volume from the end station volume. This length is ~ 34.3 m for the ITMs and ~ 10.9 m for the ETMs. For both cases, we assume a snout radius of 0.225 m. The heating is given by the Stefan-Boltzmann law multiplied by the geometric view factor from the TM face to the snout opening. This must be corrected for the non-ideal emissivity of the HR surface. The view factor $F_{\text{TM}\to\text{BT}}$ is calculated using a disk-to-disk geometry:

$$F_{\text{TM}\to\text{BT}} = \frac{1}{2}(S - (S^2 - 4(\frac{r_{\text{snout}}}{r_{\text{TM}}})^2)^{1/2})$$

where

$$S = 1 + \frac{1 + (r_{\text{snout}}/L_{\text{snout}})^2}{(r_{\text{TM}}/L_{\text{snout}})^2}$$

We consider a 10 m snout length for the ETM shielding. The power incident on the ETM from the beam tube is approximately:

$$P_{\text{ETM}} = \sigma T^4 \pi r_{\text{TM}}^2 F_{\text{TM}\to\text{BT}}\big|_{L_{\text{snout}}=10\text{m}} = 35\,\text{mW}.$$

For the ITMs, beam tube heating is deposited from both sides of the snout. The presence of the room-temperature compensation plate 3 m from the ITM limits its snout length towards the BSC. However the snout can extend 10 m towards the arm, and thus we end up with asymmetric heating terms:

$$P_{\text{ITM}_1} = \sigma T^4 \pi r_{\text{TM}}^2 F_{\text{TM}\to\text{BT}}\big|_{L_{\text{snout}}=3\text{m}} = 376\,\text{mW}.$$

$$P_{\mathrm{ITM}_2} = \sigma T^4 \pi r_{\mathrm{TM}}^2 F_{\mathrm{TM}\to\mathrm{BT}}\big|_{L_{\mathrm{snout}}=10\mathrm{m}} = 35\,\mathrm{mW}.$$

These are rough, conservative calculations (assuming most efficient radiative heating) and do not take surface emissivities into account. In reality the design emissivities of the TM HR/AR surfaces, compensation plate, and beam tube are chosen to minimize the heat load deposited on the ITM. For example an emissivity of 0.1 on the beam tube surface (current design) would roughly reduce the beam tube heating power by an order of magnitude. See Appendix G for a full TM thermal model and thorough heat budget.

4.3.5 High Emissivity Coatings

The radiative cooling aspect of the Voyager design will require coatings with high emissivity in the 10 – 100 µm wavelength band. Table 3 lists requirements for these coatings that permit the desired steady state test mass temperature. Table 4 lists details on candidate materials.

The leading high-emissivity coating candidate for the test mass barrel is amorphous alumina. Other options being explored include black silicon and silicon nitride. Emissivity testing of these candidates is in progress, and techniques for bonding the coating with bulk silicon will need to be performed.

Similarly, Table 3 lists the need for a high emissivity coating on the inner surfaces of the inner shields. Selection of this coating can be less strict than that for the test mass; however, it must similarly demonstrate low outgassing levels for vacuum compatibility. Procurement of the candidate Ball IR Black coating is in progress, which advertises an emissivity of 0.92 at 123 K for a thickness of 0.48 mm (19 mil) [70].

Surface	Emissivity (5-50 microns)	BRDF (2 microns)	Durability	Mech Q
Test Mass Barrel	>0.95	none	high	>1000?
Test Mass HR Surface	<0.3	none	none	high
Test Mass AR Surface	<0.3	none	none	high
Inner Sus Shield Inner Surface	>0.95	<0.01	high	<1000?
Inner Sus Shield Outer Surface	<0.1	none	high	none
Outer Sus Shield Inner Surface	<0.1	none	high	none
Outer Sus Shield Outer Surface	<0.1	none	high	none
Inner Snout Shield Inner Surface	>0.90	<0.01	high	none
Inner Snout Shield Outer Surface	<0.1	none	high	none
Outer Snout Shield Inner Surface	<0.1	none	high	none
Outer Snout Shield Outer Surface	<0.1	none	high	none
Inner Cryopump Shield Inner Surface	>0.90	<0.01	high	none
Inner Cryopump Shield Outer Surface	<0.1	none	high	none
Outer Cryopump Shield Inner Surface	<0.1	none	high	none
Outer Cryopump Shield Outer Surface	<0.1	none	high	none

TABLE 3: Requirements for emissivity of the shield surfaces. Different applications in the system lead to different requirements.

Material	Emissivity (50 K, 125 K)	Absorbtivity (2μm)	BRDF (2μm)	Adhesion (Si)	Adhesion (Al)	Outgas	TM Damage	Use	Refs
Amorphous Alumina	0.5, 0.66	—	—	HIGH	—	LOW	—	TM	[2], [111]
Black Silicon Black Silicon	0.4, 0.7	LOW	—	HIGH	—	HIGH w/o sealing	—	TM	[92]
Silicon Nitride	0.4, 0.56	LOW	—	HIGH	—	LOW	—	TM	[113]
Ball IR Black (0.48 mm thick)	0.86, 0.92	LOW	—	—	HIGH	MEDIUM	—	Shields	[70], [43]
Ball IR Black (2 mm thick)	0.94, 0.95	LOW	—	—	HIGH	MEDIUM	—	Shields	[152], [43]

TABLE 4: Selection matrix for high emissivity coatings. Fields with —are unknown; no references at the time of writing have been found.

4.3.6 Transmission Monitor

It will be necessary to monitor the beam transmitted through the ETM for several purposes:

1. Arm transmitted power is used for monitoring the cavity lock state
2. Transmitted beam is used in global angular controls
3. Auxiliary Locking System injection beam (perhaps)

The transmission monitor should be behind a cold window. If the reaction mass (and compensation plates for the ITMs) are used as the cold window, we may need to hang them by thicker wires and cool them by conduction down to 80 K.

4.4 Unresolved Issues

- Will temperature fluctuations lead to time varying stress/strain of the coatings?
- Will temperature fluctuations lead to troublesome excursions in the optical properties, such as thermal lensing or coating reflectivity?
- Selection of high emissivity coatings that are mechanically robust, UHV compatible, and do not contribute too much thermal noise (for the case of the test mass barrel).
- Bolted joints with reliably high thermal conductivity for thermal strap connections to the suspended shields.
- Improvements to scattered light noise performance of the cryo shields.
- Suspension cage design and how it interfaces with the shields.

4.4.1 Ice layer formation

Background One of the issues needs to be considered for cryogenic interferometers is the molecular layer formation on the cryogenic test mass surface. In the context of

gravitational wave detectors, it was first experimentally recognized at prototype interferometer for KAGRA [104, 105] as a measurement of optical loss and its trend. The issue has recently gained more attention in the actual "mirror fogging" of KAGRA's cryogenic mirror.

The arm power loss comes from the increased absorption, scattering, and the reflectivity change due to the additional thin layer on the mirror surface. The theoretical studies can be found in [60, 133, 145]. The possible influence to the mirror thermal noise was also pointed out by [137].

Experimental studies have been reported [91, 144] to relate the optical loss and the thickness of the molecular layer, where in-situ thickness was measured with ellipsometry.

Mitigation Here the solution to the ice layer formation is presented based on the references [60, 133].

First of all, quantitative investigation is needed to determine how much the ice formation will become the issue in LIGO Voyager and how it is different from ET and KAGRA cases, since the ice layer issues were investigated so far in the context of the lower cryogenic temperature like 10 K. The test mass temperature of 123 K is intermediate between room temperature and cryogenic temperature, and thus the vapor pressure of water is not completely zero. How much the impact of this difference is needed to be estimated. In addition to theoretical study, the experimental observation through table-top and prototype setups will be necessary.

Mitigation of the ice layer formation is categorized in two types: passive and active. The passive method is basically to keep the gas pressure around the test mass. The active involves some form of irradiation to the test mass surface, giving the molecules (mainly water) thermal or non-thermal kinetic energy to kick them off the mirror surface.

Passive mitigation: Reduction of the gas pressure around the test mass is achieved by the regular effort to lower the outgas from the in-vacuum materials. In addition, we can expect cryopumping by the cryo-shields to improve the vacuum pressure. This will require a proper order to cool down of the shields, the suspensions, and the test masses.

Active mitigation: Even if the passive methods can reduce the rate of layer formation, this may mean that the frequency of de-icing will only be reduced, Therefore, the occasional use of active mitigation methods should also be considered.

Temporary heating of the test mass is one way. Radiative or resistive heaters as well as CO_2 laser heating may be employed. The temperature raising and successive re-cooling will not only cause disruption of the low noise operation and the consequent detector deadtime increase, but also cause mechanical stress associated with the frequent temperature cycles.

UV or electro illumination are also considered as the non-thermal irradiation. See details in [133].

4.5 Development Approach and Timeline

While some of this work is necessarily sequential, some of it can be pursued in parallel.

R&D [3 years] The items that require the most research and development are the coatings for low and high emissivity on the shields and the test mass. All coatings need to be mechanically robust. The test mass high emissivity barrel coating needs to be low loss, though maybe there is benefit to some loss for the parametric instabilities. The high emissivity coatings on the shield inner surfaces need to have generally low BRDF for scattered light concerns.

Baffling may also be desired to help mitigate both scattering and heat transfer issues. For scattering, baffling may help direct reflected light away from the cavity. For heat transfer, baffles inside the beam tube components of the shields may prevent warm light from being funneled down the tube at low grazing angles.

Thermal modeling will also undergo further development and refinement.

Mariner40 prototype [3 years] A small scale cryogenic prototype will be developed and tested at the Caltech 40 m Laboratory.

Full scale prototype [2 years] A full size end station prototype will be developed and tested at either Caltech or MIT.

Cryogenic engineering [1 year] The cryogenic engineering for the observatories can be developed in parallel with the prototyping work.

Production and procurement [1.5 years] The production and procurement for all parts of the cryogenic shielding, baffling, heat conduction, and cooling.

Assembly and installation [1 year] Much of this work will occur simultaneously and in conjunction with the suspension assembly and installation. The cryogenic shielding work inside the beam tube will occur separately.

5 Suspension Upgrade

5.1 Overview

The LIGO Voyager test mass suspension inherits aLIGO's quad pendulum construction and vibration isolation concept. In addition, it incorporates several redesigns to be compatible with Voyager's heavier cold silicon test mass.

The performance drivers for the test mass suspension are vibration isolation and thermal noise. The parameters of the suspension here are determined to optimize these performances. However, design for assembly, maintenance, and control is equally important and must be considered as well. The penultimate mass (PUM) is also cooled down to make the entire final stage cold. (See Appendix I for the downselection of the choice to use a cold PUM with silicon ribbons/fibers.)

Matching with the heavier test mass, the weight of the upper sections is heavier. Mass and length distribution under the practical constraints have also been optimized. Along with these factors, the materials and strength of the various components have been considered.

In the following sections, the resulting suspension design and performance are discussed.

5.2 Requirements

Seismic noise and thermal noise are the two key performance indicators of a test mass suspension. The noise contribution of these has large spectral power at low frequency. The suspension design must optimize the contribution of these two such that they do not exceed the other noise contributions in the observation band. In the latest design, we set the optimization to make the total suspension noise be minimized at 12 Hz.

To facilitate parameter optimization, we assumed the following configurations as follows:

- For the seismic noise (i.e., vibration isolation), we limit the total length and weight of the pendulum so that it can be placed on the ISI.
- The coupling from the vertical vibration (or thermal noise) assumed the coupling factor of 10^{-3}.
- For the thermal noise, we assume that the bottom two masses are both cold.
- The upper three stages are suspended with steel wires while the last stage is made of silicon ribbon.
- The highest frequency bounce and roll modes are required to be less than 9 Hz in order to be outside the detection band. This requirement results in each stage needing blade springs. The vertical blade springs on the PUM are to be made of silicon,

TABLE 5: Voyager quad suspension parameters.

	Top	Intermediate	Penultimate	Final
Masses				
weight [kg]	50.0	70.0	200	200
material	SS/Al	SS/Al	Si or Al	Si
temperature [K]	123	295	123	123
length [m]	0.150	0.150	0.559	0.782
Suspension Strings				
# of strings	2	4	4	4
material	C70 steel	C70 steel	C70 steel	Si
string type	wire	wire	wire	ribbon
diameter/geometry [mm]	2.16	1.45	1.34	10×0.5
Vertical Springs				
material	Maraging	Maraging	Maraging	Si
spring constant [3] [N/m]	1.14×10^5	1.82×10^4	2.63×10^4	2.60×10^5

while all other blades are maraging steel. Other material options are considered and discussed in Section 5.4.1.

The material safety factor assumed in the design is about 3. The current parameters are calculated assuming silicon can tolerate stress of 100 MPa, but this may be improved as development progresses.

5.3 Technical Details

5.3.1 Details of the Voyager suspension design

Table 5 shows the main parameters of Voyager quad suspension.

In optimizing the mass and length of each stage based on the thermal noise and seismic noise performance, the following restrictions were imposed:

- The bottom two stages are cooled down to 123 K, while the upper two stages are left warm. This is to avoid the thermal noise injection from the upper side of the final stage.
- The total length of the suspension (from the suspension point to the beam elevation = the center of the mirror) was set to be 1.642 m, according to T1500046.
- The total weight of the main suspension chain was set to be 520 kg.
- To keep the geometry practical, the minimum length of the upper two stages is set to be 0.15 m.

- The maximum weight of PUM was set to be 200 kg.
- The diameters of the steel wires were determined by the tensile stress to be 700 MPa, which corresponds to a safety factor of three.
- The spring constants of the blade springs are scaled from aLIGO quad design according to the cumulative weight of the suspension below the stage in question.

The noise spectra of the suspension as a result of the design optimization are shown in Section 5.3.2.

Top and Intermediate stages: The upper two stages are warm metal suspension, and thus the structural concept can be similar to the aLIGO ones.

In this suspension design, the upper two stages are kept as short as possible. This is a deviation from the mass distribution optimized for vibration isolation[4]. The reason is that the final two stages must be as long as possible to minimize the impact of the thermal noise from the warm upper end of the UIM-PUM wires.

Penultimate stage: The PUM is cooled for the thermal noise reduction of the final stage pendulum. In addition, silicon blade springs are used for vertical vibration isolation and vertical thermal noise reduction.

Final stage: The test mass is suspended with silicon. This can be ribbons or fibers. Primarily because of the simpler manufacturing, ribbons are used in the design.

Thermal drift of vertical springs: The temperature of the warm vertical springs will likely decrease some amount once cooling begins, despite being outside the cryogenic shields. The springs closer to the shields will likely experience a greater impact. Consequently, it may be desirable to apply heaters and temperature control to these springs to mitigate alignment drifting. Thermal drifts will occur not just in the vertical direction but in pitch as well, since the pitch restoring force is sensitive to the vertical positions of the spring tips inside the stages. Heaters can be non-contact via radiative coupling near the springs. Sensing can be done by measuring the vertical height of each stage using OSEMs or some other displacement sensor.

The silicon springs at the penultimate mass will need to remain cold and thus will need to accept some thermal drift. Certain geometries, like blade springs, will minimize thermal expansion offsets in the vertical direction. However, there may be no geometry that can minimize vertical drift effects from changes in the Young's Modulus.

[4]For the mass distribution optimization with regard to the vibration isolation, see T1300786, T2100287, and G2300711.

5.3.2 Noise performance

Figure 17 shows the noise contributions of the seismic and suspension thermal noise. Here the seismic spectrum was supposed to be 10 times better than the aLIGO performance taking account of the sensor upgrade of the ISI.

Below 12 Hz, the seismic noise is going to be the dominant noise contribution to the sensitivity. Above 12 Hz, the suspension thermal noise is going to be above the seismic noise, but still lower than the quantum noise. All of them basically share the same cross over frequency.

Figure 18 shows the breakdown of the suspension thermal noise. The horizontal and vertical thermal noises from a particular place (not from a particular stage) are individually plotted. At the very high frequency the thermal noise from the bottom stage is going to be dominant. Below 20 Hz, however, the horizontal and vertical noise from the warm upper side of the penultimate stage is going to be dominant.

Figure 19 shows the vibration isolation ratio for the horizontal and vertical directions. In the observation band, the vertical isolation has about 1000 times higher than the horizontal one. This difference is, in fact, compensated by the coupling factor of 10^{-3}.

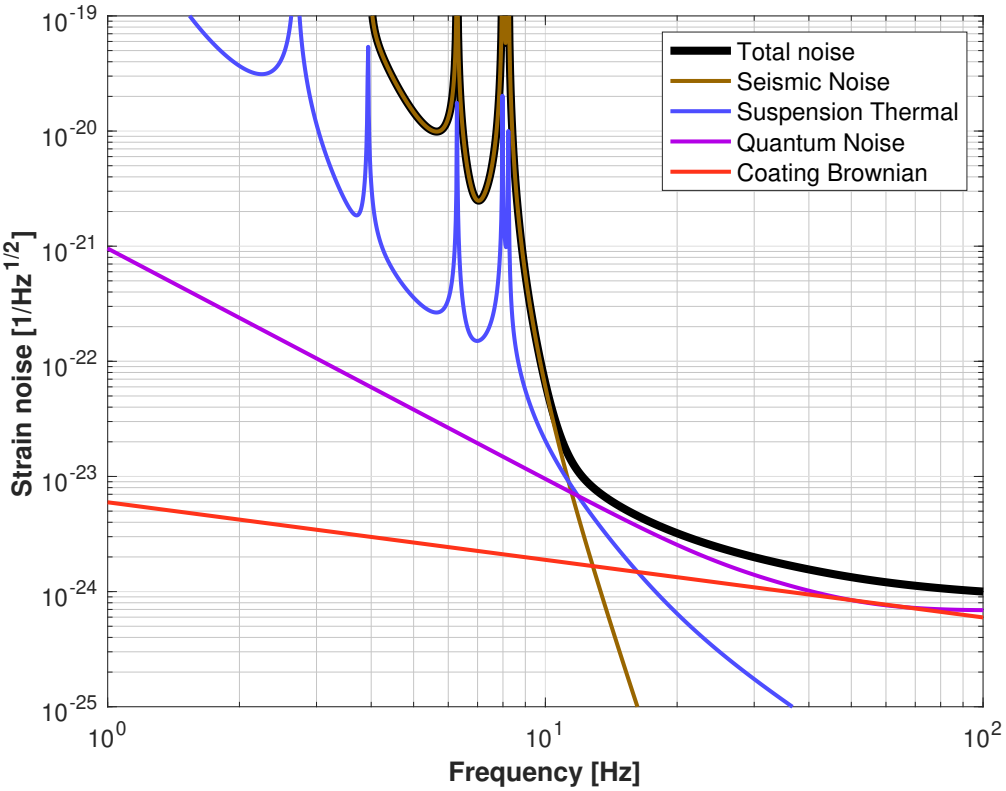

FIGURE 17: Noise budget in the low frequency band

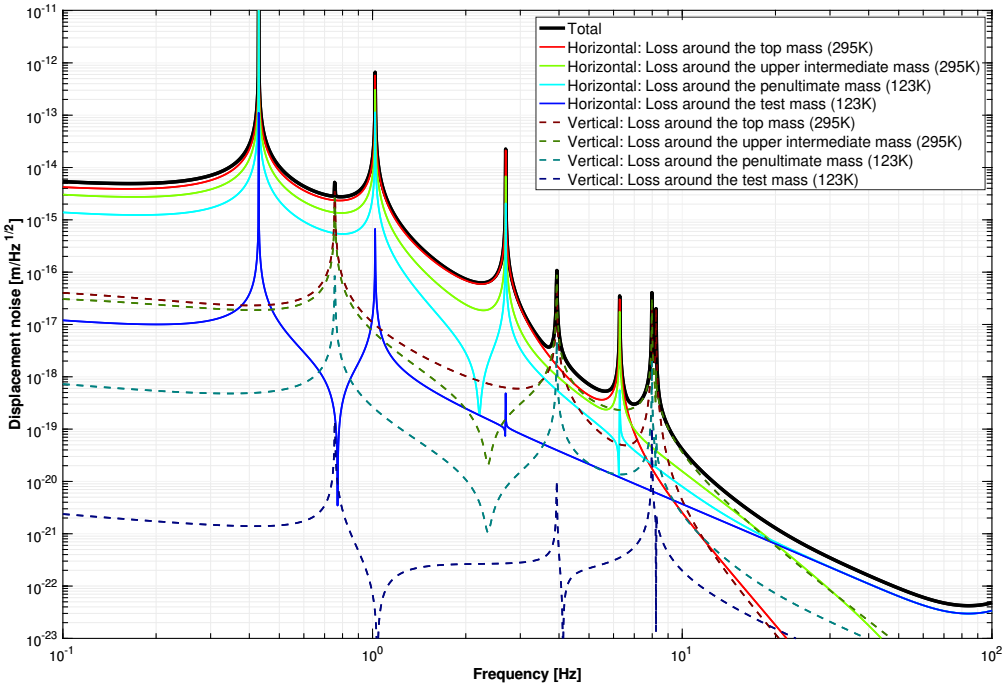

FIGURE 18: Breakdown of the suspension thermal noise by the direction and location of the noise sources

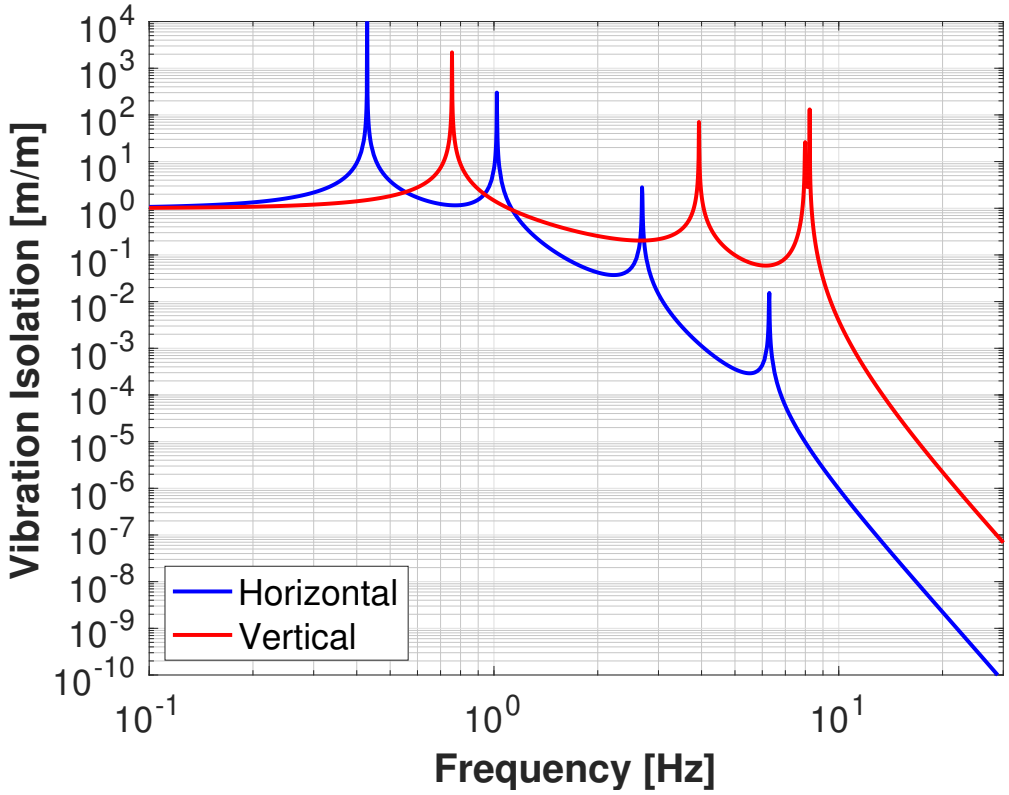

FIGURE 19: Suspension vibration isolation ratio for the horizontal and vertical directions

5.3.3 Seismic platform weight limits

The existing BSC-ISI platforms were engineered to be able to handle the additional mass that comes from having a FM (folding mirror) suspension or a TMS (Transmission Monitor Suspension). Since we no longer plan to have a second interferometer installed at the LIGO Hanford site, there is some additional capacity to have a heavier suspension there, especially if the ITM suspension is moved to the center of the ISI platform.

For the ETM ISI, there is a similar weight savings due to the TMS residing in a separate chamber. The Voyager test masses (TMs) will be enclosed by cryogenic baffles, and the connection to the TMS and the ALS laser will be made through cold windows[5] (cf. Fig. 20).

The TM's is 200 kg and the total mass of the suspension main chain is 520 kg, which is 2.6 times the Voyager TM. Considering the level of the various suspension/seismic noise sources, the mass distribution of the quad does not necessarily need to be optimized with respect to vibration isolation, as already discussed above. There is also some margin to further reduce the mass of the upper stage with a slight, concomitant increase of the seismic noise. However, the direct contribution of seismic noise in the observation band is minimal.

The mass of the reaction chain can be significantly lighter than the main chain without significant disadvantages. The main drawback is actuation nonlinearity[6] (bilinear coupling) due to the increased variability of the actuator operating distance. This effect, however, is negligible for the TM/ESD, where the noise requirement is most severe.

Thus, the combined mass of both chains is less than 700 kg and can be further reduced if necessary. Considering these factors, it is clear that the Voyager TM suspensions will fit within the weight limits of the existing ISI (1000 kg–1100 kg) [7].

The remaining weight margin is used for the suspension cages and other structural setups. Regarding cryogenics, no components will contribute to the ISI payload (cf. Fig. 20). The inner shield around the suspension chains is suspended from stage 0 of the ISI, the ISI's base structure. The outer shield and the outer shield tubes are rigidly mounted on the vacuum chamber and the main beam tube. The inner shield tubes will be suspended from the main beam tube. Therefore, only the inner shield near the mirror is added to the ISI weight budget.

5.4 Unresolved issues

[5] Similar to the existing cold windows used in our prototypes: optical quality viewport with high absorption in the MWIR and LWIR, and a high transmission in the NIR. These windows are conductively cooled via attachment to the cryogenic shields.

[6] Brett Shapiro, private communication (2022)

[7] cf. E1000032 and G2102249

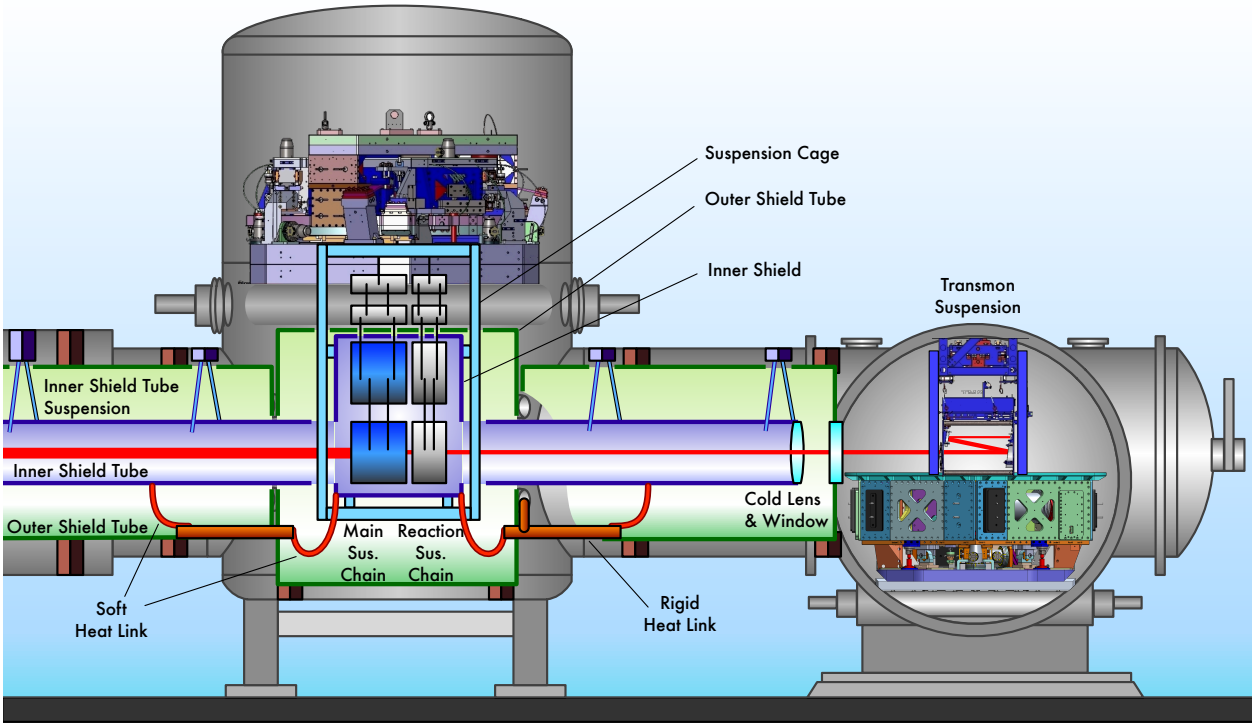

FIGURE 20: Sketch of the ETM chamber configuration. The TMS will be accommodated in an independent chamber. The main and reaction chains are suspended from the BSC-ISI. The suspension cage is rigidly attached to the BSC-ISI. The inner shield around the lower suspension is suspended from stage 0 of the ISI, the ISI's base structure. The outer shield and the outer shield tubes are rigidly mounted on the vacuum chamber and the main beam tube. This allows us to use thick, high thermal conductance connections for the main heat extraction path to the cryo-cooler for the outer shields. The inner shield tubes are suspended from the main beam tube. Soft copper links are used to extract the heat from the inner shield and the inner shield tubes. The hot radiation from the TMS is blocked with cold windows.

5.4.1 Metal final stage

Since the suspension thermal noise limits only at the lowest edge in the observation band, it is not a major problem to operate the interferometer with metal-made final stage suspensions until other noises in the low frequency band are reduced to the planned sensitivity. Thus, the suspension R&D and interferometer development can be done in parallel until the appropriate time comes.

With steel wire suspension, however, the deviation of the sensitivity from the design starts from 100 Hz (See Appendix I). If we can use a material that is easier to handle and has better Q than the Steel, the value of the intermediate metal suspension would increase.

Possible alternative materials for the vertical blades and ribbons for the final stage are Al or CuBe alloys.

Some of the aluminum arroys like 5056 and 2090 show a Q of ~ 10^6 at ~100 K [35, 138]. A heat treatment is not necessary as it is expected to change the Q below 50 K. The tensil strength is in the range of 300 MPa to 400 MPa.

Beryllium Copper (BeCu) is another promising material for the purpose. A Q factor of ~1×10^6 was observed at ~100 K for annealed C17200 [36]. BeCu is a superior material as a spring. The tensile strength is expected to be 1.3 GPa to 1.5 GPa. It is toxic during machining. Otherwise, it is stable and requires no special treatment.

Estimates of the performance of these alternative metals still need to be made.

5.4.2 Silicon ribbons and blades

Breaking strength of silicon and mode frequencies: Maximizing the breaking strength of the silicon suspension components is desirable in order to achieve a low bounce mode frequency in the blade springs, and high violin mode frequencies in the ribbons.

Silicon is intrinsically a strong material, whose full potential strength has been realized in nanoscale devices [165]. However, surface defects are generally found to limit the fracture strength on a macroscopic scale [32].

Silicon ribbons: Silicon crystal fibers grown using the micro-pulling-down technique have been studied as possible suspension wires [5, 6, 129]. Fibers and ribbons have also been grown by other methods, including chemical vapor deposition [109] and floating zone techniques [27, 160]. The surface quality of grown fibers and ribbons is consistently good at the microscale [32], but still needs to be characterized for macroscopic samples.

Silicon ribbons can be cut or etched from wafers [13, 28]. In wafers, the edge profile was found to be an important factor in increasing the resilience, rounded edges being preferable [25].

Anisotropic etching of {111} silicon is known to produce perfect, atomically flat surfaces

at the microscale [64]. However, {111} silicon with high oxygen content has a loss peak near 123 K [80, 127].

Additional work to be done for silicon ribbons includes the following items:

- Determination of the profile of the ribbon that provides reliable bonding and minimal suspension losses.
- Analysis of the loss mechanisms in silicon ribbons and the temperature and frequency dependence of those losses. These mechanisms depend on the growth method, content and type of impurities, the fabrication technique, and additional treatments.
- Determination of the minimal value of mechanical loss in silicon at 123 K caused by fundamental loss mechanisms.
- Experimental measurements of mechanical losses in ribbons for a wide range of frequencies and temperatures by fabricating of ribbon-like mechanical oscillators.
- Identification of loss sources.

Silicon blades: Alternatives to blade springs, such as geometric anti-springs or Euler springs, would also provide a way to decouple the bounce/roll mode frequency from the breaking strength [23, 101]. The bounce and roll mode frequency requirements in Section 5.2 require further detailed consideration of the blade design to be compatible with the size and strength.

Surface loss and thermal noise: Surface loss in silicon is the likely limit to thermal noise in a ribbon geometry, where the thermoelastic loss is small. It was found to be low at temperatures near 0 K [107], but apparently has not been characterized at 123 K. Further reductions may be available through improved surface quality and passivation [62, 97, 146].

Implementation Assuming ribbons can be manufactured, detailed studies of how to attach them to the TMs and PUMs are needed. The science requires sufficiently strong and low loss bonding at the interface with the TM ears and blade springs, while there are also engineering requirements such as replaceability.

See Section 5.4.3 for bonding.

Fabrication

- Ribbons instead of fibers so that they can have a 10:1 aspect ratio and thereby a large dissipation dilution. There is some trade off here because the increased aspect ratio increases the fraction of energy stored in the lossy surface region. Also, since we are operating at 123 K where the thermoelastic noise goes to zero, it can not be made to cancel the dY/dT term. Therefore we can not operate at extremely high stresses where dY/dT dominates.
- It is hoped that when working with silicon instead of silica, there will be a performance improvement by moving from round fibers to rectangular cross-section ribbons, due to the better preparation of the surface.
- Realization of techniques for fabrication of Silicon ribbons
  - Wet chemical etching
  - Dry chemical etching
  - Additional chemical treatment for reduction of mechanical losses and increasing of breaking strength.
- Realization of techniques for bonding of silicon ribbons. See Section 5.4.3.
- Fabricating and testing reduced prototypes of quasi monolithic silicon suspension.
  - Optical
  - Thermal
  - Mechanical (Young's modulus, loss angle)
- Analysis and measurement of additional mechanical losses and noise in the test masses associated with interaction of the test mass with electrostatic drive taking into account electrical conductivity of silicon at temperature of 123 K.
- Analysis of stability of the operating temperature on different noises (how stable must the local and average temperature of the test mass be).
- Comparison of the measured to required LIGO Voyager parameters.

5.4.3 Silicon bonding

The silicon bonding techniques will be required for the silicon ribbons to be attached to the test masses and the blade springs. The technique should provide reliable bonding with minimal suspension losses.

Several methods, like chemical bonding (e.g. HCB) and direct bonding (optical contact), are known. It is necessary to choose and test for breaking strength and mechanical losses.

5.4.4 Actuation of ETMs

The LIGO test masses are currently controlled via actuation of upper stages of the suspension as well as forces directly applied to the mirror. This mirror actuation is necessary for several purposes:

1. longitudinal motion to lock the DARM degree of freedom
2. angular control of the arm cavities (should be entirely handled by the PUM)
3. control of parametric instabilities

However, given the problems we have experienced with electro-static actuation, and the unknown (as of yet) problems associated with having a high voltage actuator on a semiconductor, we would like to avoid this. Doing away with an ESD also allows us to have the reaction chain of the suspension at a larger distance.

The current ESD delivers a force of ~400 uN to a 40 kg mass. For a 200 kg mass, this would require 2000 uN to achieve the same displacement (above the pendulum longitudinal eigenfrequency).

Some possible candidates for a 2 mN ETM actuator:

- photon calibrator (P = 300 kW)
- amplitude modulated field injected through the dark port
- magnets: glue would be a thermal noise source, though it may also help with damping parametric instabilities. The glue would also have to survive thermal cycling.
- ESD: this may produce heating issues in the silicon test mass via eddy currents
- Newtonian gravity actuator: may be a source of vibration

In reality, we do not use the full design range of the aLIGO actuator. Further modeling is required to determine what the actuator range requirement really is. It is possible to consider increasing the range of the upper stage actuators to compensate.

There could also be two styles of actuators, one low noise and small range, the other high noise but high range. The latter would be used for locking, or preventing lock loss during high noise times. The former would be used while in science mode. It is possible that in this case we could get away without a reaction mass altogether. For example, perhaps the high noise actuator could be mounted to the cage.

5.4.5 Detailed suspension modeling

The Voyager suspension model so far has been calculated with a point mass model. A detailed study of the suspension geometry with a rigid body model is also needed. An FEA model is also needed for more detailed study of thermal noise and strength evaluation. These are currently missing although the tools are readily available.

5.5 Development Approach & Timeline

5.5.1 Development Stages

Much of the research work can be pursued in parallel. The dates given will depend mainly on the start date and how much of the initial work is done in parallel since the initial period contains a significant amount of work.

R&D

- **Ribbon Production [3 years]**
  The development work required to produce silicon ribbons of appropriate geometry and strength is dealt with in more detail in section 5.4.2. As far as schedule is concerned, we note that this drives much of the rest of the work. Some parts of ribbon development will be done in parallel with strength testing since these are codependent. The timescale for this particular section of research is challenging to predict, though around 3 to 4 years seems a reasonable estimate.

- **Strength Testing [2 years]**
  The highest risk part of the silicon ribbon research is the tensile strength achievable. Results to date show a large variation in values and are completely dependent on surface preparation. Strength testing should be carried out as a function of temperature rather than just at room temperature. We propose to undertake testing of a large number of small silicon samples (approximately 3"×0.5"×0.02") using destructive strength testing. During this initial phase which would last for around 1 year, we will test many different surface preparations as listed in section 5.4.2. It will be crucial to complete this phase of testing early on to mitigate risk. In parallel, each stage of progress will be mirrored with strength testing of the ribbons. The final full length ribbons must have a reasonable group of results from strength testing, such that statistics can be gained to understand failure rates.

- **PUM Springs [3.5 years]**
  Silicon springs at the penultimate mass (PUM) will be needed to lower the bounce and roll mode frequencies. This is particularly important if the tensile strength of silicon ribbons proves too low to achieve frequencies below 10 Hz without springs. This work must include methods of attaching the springs to both the penultimate mass and the ribbons.

- **Silicon material losses [1 year]**
  Initial research into dissipation in silicon at cryogenic temperatures has already been done by several groups worldwide. It is likely that we will want to repeat some aspects of this using the exact material processing that we choose to use. This work can be undertaken in parallel to other research.

- **Bonding research [3 years]**
  The ribbon fibers will need to be bonded to the masses through some means, whether that involves intermediate 'ears' or direct bonding. Bonding of silicon can be done using hydroxycatalysis bonding, similar to aLIGO, however it requires oxidation of the surfaces prior to bonding. The exact method for these joints will require research including strength testing and mechanical loss measurements. The results of these will be used to produce a finite element model that can give the thermal noise from the bonds.

Suspension design

- **Seismic isolation performance [0.3 years]**
  Not a driving concern in the design, but the total noise performance including direct seismic transmission and noise pollution from the local damping loops must be considered. As-built aLIGO damping loop gains are higher than the aLIGO design, so LIGO Voyager should incorporate this knowledge.

- **Thermal Noise Modeling of Suspension Final Stage [1 year]**
  The suspension design downselection will be based on FEA modeling, including a detailed structure of the bulk and surface losses.

- **Engineering [1 year]**
  Incorporation of lessons learned in the commissioning of the aLIGO suspensions including: design of damping feedback loops for the free body modes, the bounce and roll modes, and the violin modes; minimized couplings between degrees of freedom; generally good controllability and observability; and ease of assembly and maintenance.

Monolithic suspension prototyping [2 years] We propose to build a partial prototype suspension in order to demonstrate all the technology required for the monolithic structure of the suspension and the cryogenic cooling. This does not need to be a quadruple suspension. It should include the final two stages of the suspension.

The duration given here is indicative of build time for this suspension rather than the research and engineering that would precede this phase.

Full engineering prototyping [4 years] Similar to the noise prototype suspension produced for aLIGO, we propose to produce one full-size cryogenic silicon suspension

as a prototype. At first a metal prototype should be made (1 year). This will allow us to examine the suspension performance comparing it with a model. This also provides us the mating test with a ISI platform. This prototyping can be done in parallel with the prototyping of the monolithic stage.

After (or before) the metal suspension test, the cryogenic system should be added to the facility. (1 year)

Once the technology of the monolithic stage is established at the monolithic prototype, the same technology will be incorporated to the prototype. (1.5 years)

At this point we are going to demonstrate the full cryogenic prototype mated with an ISI platform. This will be a major demonstration of the readiness of the suspension.

Production and Procurement [1.5 years] Production and procurement of parts for full suspensions, including suspension structures, all custom design mechanical parts, upper stages including vertical isolation components.

Assembly work [1.5 years] According to the experience of aLIGO Quad production, the production (assembly) process consists of three parts. 1) subassembly production, 2) metal suspension production, 3) monolithization. The total time of 15 months are expected for these steps. If we split the work between the site, this period can be shortened to ~9 months.

Refurbishing the aLIGO suspension for the Voyager purpose won't be an efficient choice. Here, the production of new suspensions is assumed as the default plan. Here the production of 10 suspensions are assumed.

1. **Subassembly production, 3 months, 8 people, per 10 suspensions:** In aLIGO total 16 suspensions were made ($4\,\mathrm{quads} \times 3\,\mathrm{IFOs} + 4\,\mathrm{spares}$). At LHO, subassembly for 10 quads have been made by 8 people working for ~ 3 months. We suppose this is the time we require for the subassembly for the Voyager suspension.
2. **Metal suspension assembling/testing/initial alignment, 0.7 months, 3 people, per suspension:** Metal suspension production is used for the basic test of the suspension functionality check including the transfer function test, initial alignment, and so on.
3. **Monolithization 0.4 months, per suspension:** The two lower metal masses are replaced with Silicon masses. Also the four silicon ribbons will be installed and bonded/welded with the final material.

Installation An assembled quad suspension will be mated with a cartridge, and installed into the chamber. After the transfer function testing, alignment, and cleaning, baffling will be done. This will also include closing of the cryostat. aLIGO experience

suggests this takes 2 to 3 weeks per suspension. Therefore it takes about ~3 months per site.

6 Arm Length Stabilization

As in all LIGO type interferometers, Arm length stabilization (ALS) is required for Voyager, in order to ease the problems of initial lock acquisition. The shift to silicon test masses and a different main laser wavelength require an ALS laser wavelength that will transmit through the test masses and is capable of being locked to the PSL beam.

6.0.1 Dichroic length reference

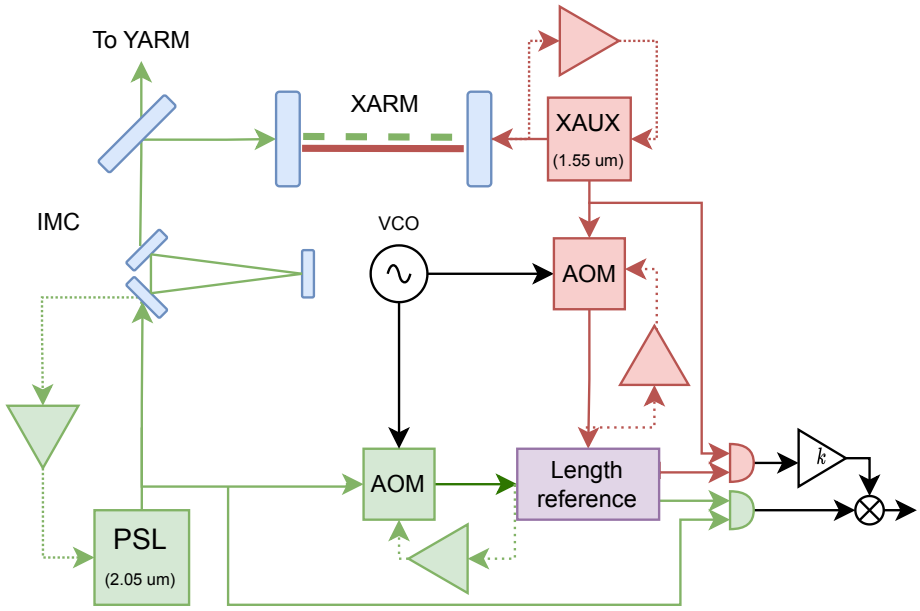

FIGURE 21: Multicolor reference cavity or delay line ALS scheme. VCO: voltage controlled oscillator, AOM: acousto-optic modulator, Ref Cav; optical delay line or reference cavity acting as frequency discriminator, PD: photodetector, IMC: input mode cleaner.

6.1 Requirements

The ALS aux field needs to transmit through the ETMs and ITMs and has to be locked to the main laser. The frequency noise on the ALS laser, relative to the main laser, needs to be $\lesssim$10 Hz RMS as in Advanced LIGO [135]. We expect the frequency stability for lock acquisition to be essentially the same for Voyager, since there are no planned changes in the coupled-cavity CARM pole.

6.2 Technical Details

Arm-length stabilization (ALS) relies on the scaled frequency comparison between the PSL and an auxiliary (AUX) laser. The AUX laser operates at a different wavelength to track the arm cavity motion independent of the rest of the interferometer. By correctly rescaling this information, a relative comparison with the PSL allows the interferometer

to approach full resonance in a controlled way. Traditionally the scaling and comparison become straightforward by letting the AUX wavelength be half the PSL wavelength, and a beatnote detection is possible after appropriate frequency doubling stages.

We consider a Voyager AUX wavelength near $\lambda_a = 1550\,\text{nm}$ to avoid the Si absorption band, and for its commercial convenience. Because of the PSL-AUX anharmonicity, a different scaling process than second harmonic generation is required before comparing the two lasers. A straightforward scheme would be to use a dichroic reference cavity (or equivalent stable length reference) acting as a transfer oscillator, schematically shown in Fig. 21. An even more general scheme would be to use an octave-spanning frequency comb stabilized in feedback or feedforward, where the latter is schematically shown in Fig. 22, making the specific AUX wavelength irrelevant.

A dichroic (multicolor) reference cavity or optical fiber acts as a common-mode delay line for the two wavelengths, and is a common way of comparing arbitrarily separated lasers when the residual length fluctuations are small. In this scheme, AUX-PSL beams are picked off and frequency shifted by the same amount before being locked to the length reference (e.g. cavity or optical fiber). Self-heterodyne frequency discrimination for PSL and AUX derives two radiofrequency signals which are scaled by the exact PSL-AUX frequency ratio k before their comparison to generate the ALS error signal.

6.2.1 Optical frequency comb

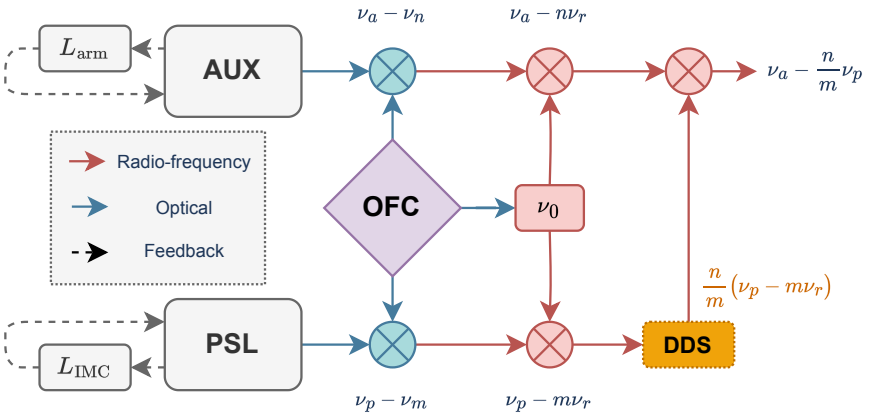

FIGURE 22: ALS error signal using optical frequency comb. IMC: input mode cleaner, DDS: digital direct synthesizer, AUX: auxiliary laser, OFC: optical frequency comb.

Optical frequency comb (OFC) teeth frequencies comprise "repetition rate" ν_r harmonics offset by a "carrier envelope offset" ν_0, which may be traced out in an octave-spanning comb. Residual OFC fluctuations may be suppressed with feedback (e.g. using the PSL as a reference), or feedforward (using the exact PSL-AUX frequency ratio k) to realize the low noise transfer oscillator. Then, the ALS error signal may be synthesized by beating PSL and AUX lasers with the OFC (i.e. scaling), and comparing the two RF signals.

6.3 Unresolved issues: ALS

1. The PSL and auxiliary lasers may be locked to each other by using the transfer oscillators described above, i.e. a dual wavelength reference cavity or an optical frequency comb.

2. A high reflectivity for the auxiliary lasers may allow high enough sensing noise to enable a calibration readout using the ALS beat signals. Such a frequency based calibration is currently under development to reject systematic errors in combination with photon calibrators.

3. Several mW level power auxiliary lasers are commercially available that can meet the frequency noise requirements if the auxiliary wavelength is chosen to be 1550 nm.

6.4 Development Approach & Timeline: ALS

1. Existing loop designs and noise budgets for the auxiliary lasers can easily be adapted

2. If the auxiliary wavelength is fixed to 1550 nm, a wide variety of commercially available options are feasible.

3. An ALS system could be prototyped with either a reference cavity of OFC at the 40m prototype (Mariner) as was done in [67]

7 Thermal Wavefront Control

As with the earlier incarnations of LIGO (Initial LIGO, Advanced LIGO and A+), LIGO Voyager requires high power to achieve the required sensitvity to GW strain. As with each of those iterations, absorption in the test mass coatings and substrates will yield temperature gradients that will alter the optical properties of the interferometer. Those earlier designs had to contend with both thermo-refractive lensing and thermo-elastic deformation, requiring correction for (1) ITM substrate lensing, (2) ITM surface deformation and (3) ETM surface deformation. However, thermal effects in Voyager appear to be easier to contend with than previously for two critical reasons:

1. a crystalline silicon test mass at 123 K has large thermal conductivity (see Fig. 41) which helps to reduce the magnitude of thermal gradients. For example, 1 ppm absorption, 3 MW incident and 3 W of absorbed power, the temperature gradient would be only ~30 mK across the beam radius.

2. the vanishing coefficient of thermal expansion at 123 K, coupled with the small thermal gradient effectively eliminates thermo-elastic deformation on surface of the test masses, removing two of the three thermal issues associated with a high power interferometer. This also removes the main issue with point absorbers on the surfaces of the optics [20].

However, the thermo-refractive coefficient (dn/dT) in silicon is *not equal to zero* at any finite temperature. Therefore, it will be important to compensate for the thermal lens in the ITMs and BS, as well as adjust the wavefronts for better matching to the other cavities and to reduce the contrast defect.

In Voyager, this thermal compensation will be achieved with room-temperature silicon compensation plates (CPs) adjacent to the beam-splitter, as illustrated in Fig. 23. The relative size of the Voyager, aLIGO and other thermal lenses are shown in Fig. 24. Despite absorbing nearly an order of magnitude more power than aLIGO, the high thermal conductivity of silicon keeps the thermal lens size to approximately 65% of that expected in A+ and just under twice what we currently see in O4.

7.1 Requirements

The thermal compensation system (TCS) will require a similar design to Advanced LIGO [19], with sensors and actuators. In order to measure thermal distortion in the test masses, the TCS requires wavefront sensors that operate at a wavelength where silicon is transparent. The sensitivity and stability requirements are expected to be the same as A+.

The thermal correction requirements for Voyager are an active area of research. As of writing this version of this document, TCS modeling is underway to determine the precision and range of compensation required for ideal IFO operation for A+ and ASharp. The requirements that emerge from that modeling will also apply to Voyager.

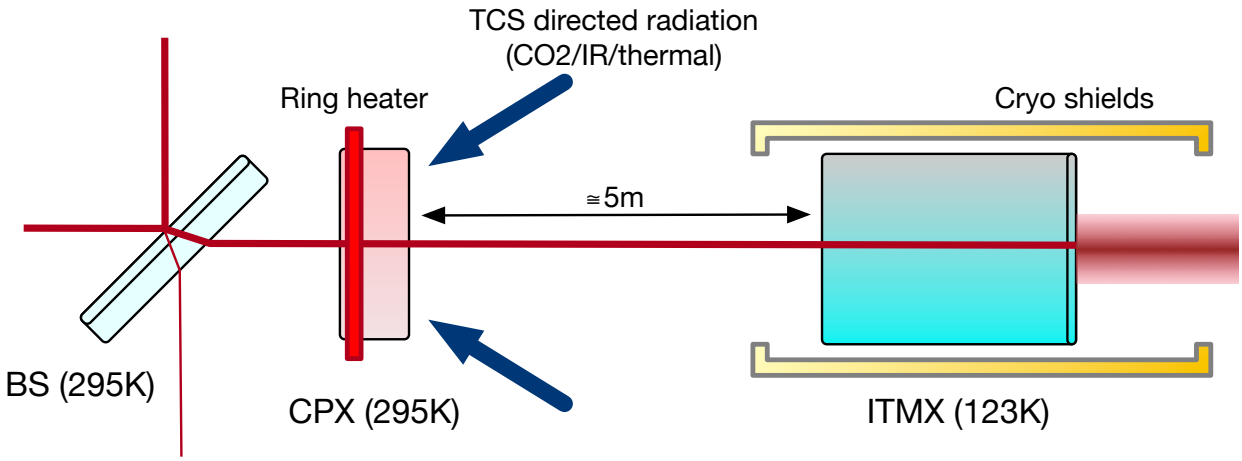

FIGURE 23: Cartoon illustrating the layout of the compensation plate and the test mass for Voyager TCS. The compensation is adjacent to the beam-splitter, approximately 5 meters from the ITM.

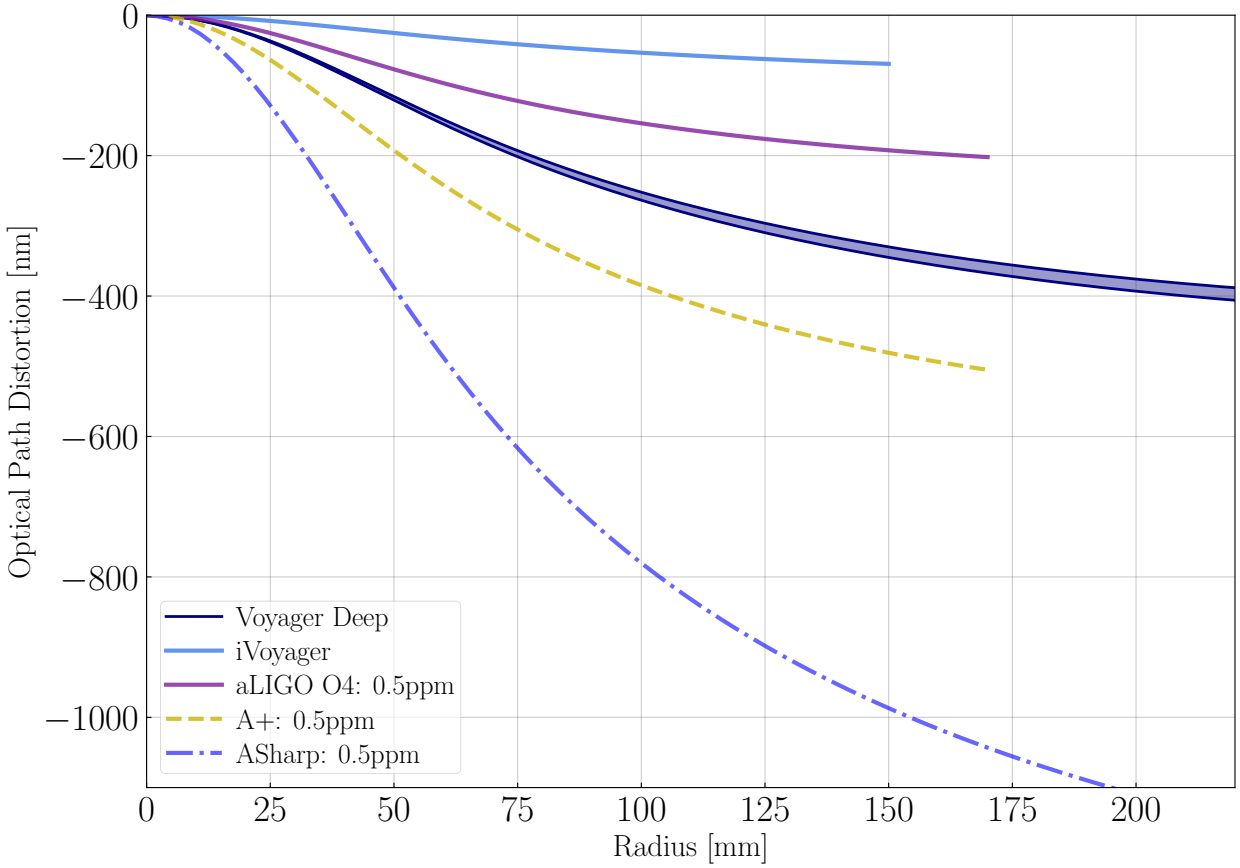

FIGURE 24: Comparison of expected optical path distortion (OPD) for aLIGO O4, A+, ASharp, iVoyager and Voyager Deep nominal operation (with the emissivity of the silicon optics ranging from 0.6 to 0.7). The relevant powers and material parameters are in Tables 6 and 7.

7.2 Technical details

The thermal compensation system for Voyager is only required to correct thermo-refractive lensing in the substrate of the ITM (and a marginal amount in the compensation plate). The inverse lens will be created in the compensation plate using a combination of ring heaters (RH) and IR lasers.

The baseline design for Voyager calls for a room-temperature silicon compensation plate located near the beam splitter. It is impractical to use a fused silica compensation plate as the additional thermal lens from self-heating alone would be larger than the lens in the ITM that we are trying to correct. Conversely, the main advantage with a room-temperature silicon CP with RH is that change in thermal conductivity and dn/dT for silicon both work in our favor when going from 123 K to 295 K. That is,

- the cryogenic silicon test mass **minimizes** the thermal lens for exposure to a large amount of self-absorbed power (ideal for minimizing the distortion we are trying to correct),
- whilst, a room temperature silicon compensation plate **maximizes** the thermal lens with power (approximately 6× stronger gain, ideal for maximizing thermal acutation).

Specifically, comparing the silicon lensing responses for annular heating at 295 K (−3.8 µD/W) and central heating at 123 K (13.4 µD/W), see Table 6, shows that we need approximately 3.5 W from the CP-ring heater for each Watt absorbed from central heating in the test mass. The absorbed power levels are given in Table 7. Given that we assume approximately 4.8 W of laser heating of the ITM from the main laser (based on a spec of 1 ppm absorption), this requires a ring heater power of approximately 17 W.

Property	Value at 295 K	Value at 123 K
Thermal conductivity, κ	150 W/m K	500 W/m K
dn/dT	1.8×10^{-4} 1/K	0.95E-4 K^{-1}
Response (dn/dT/κ)	1.2×10^{-6} m/K	1.9E-7 m/K
Central heating	85 µD/W	13.4 µD/W
Annular heating	−3.8 µD/W	−0.6 µD/W

TABLE 6: Annular heating assumes compensation plate with gold barrel

7.2.1 Example TCS compensation pattern

We assumed that the thermal control consisted of a TCS IR laser illuminating the room-temperature CP face and a ring heater (RH) around the compensation plate, as shown in Fig. 23. We calculated the intensity distribution (and RH power) required to minimize the thermo-refractive distortion for the Voyager Deep thermo-refractive lens (with 4MW in the Fabry-Perot arms). A TCS heating pattern of approximately 30 W is required with

	A+	Voyager D/WB	iVoyager
Absorption			
Substrate absorption	< 0.2 ppm/cm	$1.0\,\mathrm{km}^{-1}$	$1.0\,\mathrm{km}^{-1}$
Coating absorption	500×10^{-9}	1.0×10^{-6}	1.0×10^{-6}
Cavity powers			
Power-recycling	5.4 kW	2.8 kW	840 W
MICH. (ITM substrate)	2.7 kW	1.4 kW	420 W
Fabry-Perot Arm	750 kW	3.9 MW	1.2 MW
Absorbed power			
CP substrate	< 10 mW	280 mW	84 mW
ITM substrate	< 20 mW	840 mW	500 mW
ITM coating	380 mW	3.92 W	1.18 W
ITM total	400 mW	4.76 W	1.68 W
ETM total	380 mW	3.9 W	1.2 W

TABLE 7: Power absorbed in the Voyager optics.

a ring heater power of approximately 20 W, as illustrated in Figure Fig. 25. This simple correction leaves a residual OPD of less than 0.1 nm.

7.3 Unresolved issues

7.3.1 Control of HR Surface of TMs

The zero CTE of silicon at 123 K prevents standard ring heater techniques of control of the ROC of the test mass which precludes changing the g-factor or HOM of the arm cavities.

At the moment, there is no practical way to adjust the test mass surface (RoC and higher order terms) once the optics are manufactured. Possible ways to induce curvature changes might include mechanical and electrostatic distortion.

7.4 Development Approach & Timeline: TCS

The development approach and timeline for TCS for LIGO Voyager is expected to be similar to aLIGO. However, significant research is needed to determine what, if anything, is needed to address the lack of ability to tune the RoC of the test mass. It remains to be seen what the RoC matching requirements will be and if that can be met by initial figuring.

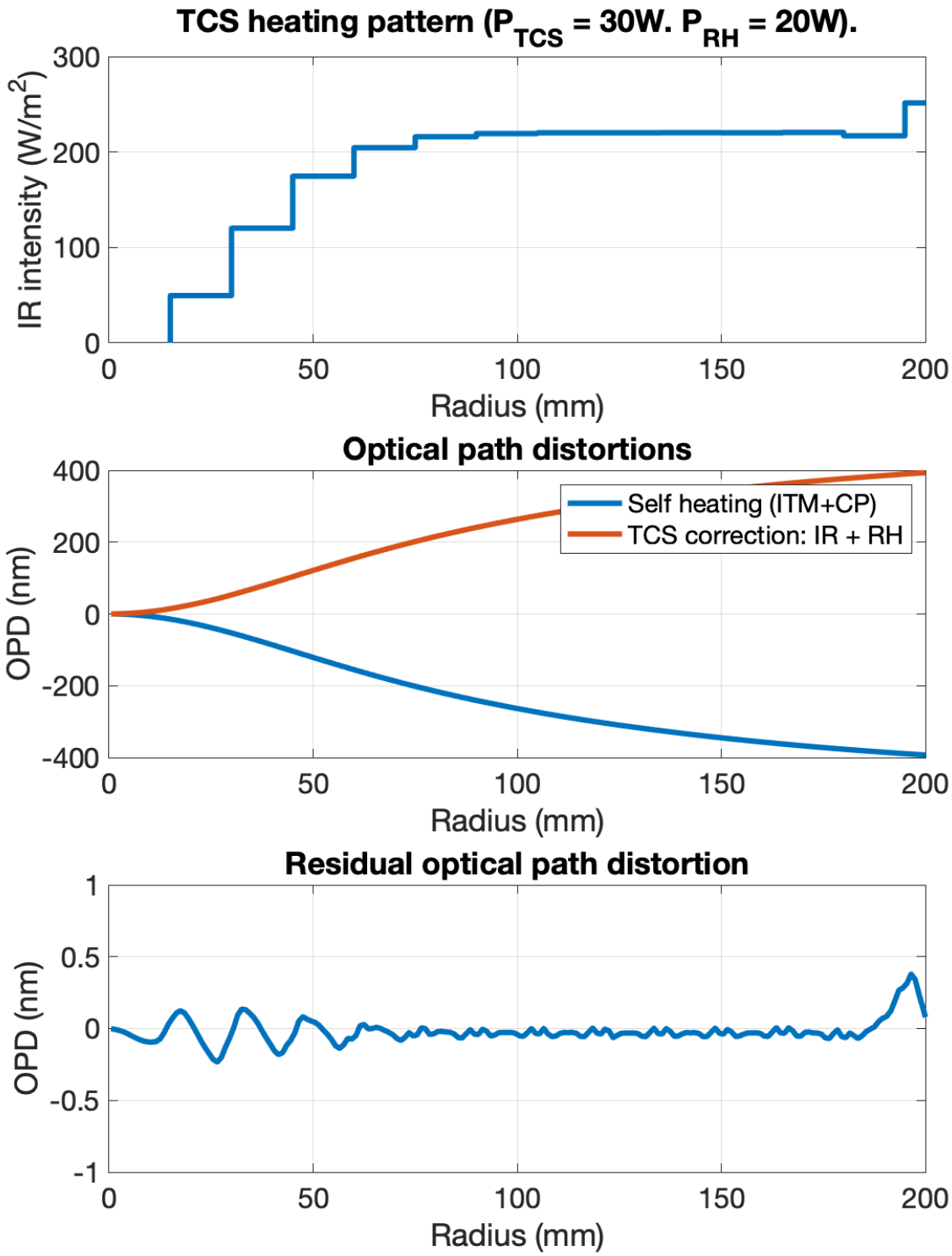

FIGURE 25: (Top) thermal compensation laser intensity pattern, (middle) optical path distortion for self heating (from ITM-coating absorption and substrate absorption in the CP and ITM) and OPD from the compensation and (bottom) the residual optical path distortion.

8 Laser Source

As described in Section 10, the laser will have a wavelength of 2050 nm. The laser output power requirement is described in Table 8.

In this section we describe the development of a pre-stabilized laser in this range: what research remains to be done and the proposed development timeline.

8.1 Overview

The selection of a laser for LIGO Voyager involves a complex decision making process which must be made in the context of a constantly evolving technological landscape. The laser requirements for LIGO Voyager are unique in that we need single frequency operation, good frequency actuation for control, high spatial coherence, high power and high reliability. These requirements will probably not be achievable in an off the shelf laser on the timescale of LIGO Voyager.

In the 2 micron region fiber laser amplifiers are attractive because of their long interaction lengths allowing efficient lasing using other dopants. Very efficient high power fiber lasers have been demonstrated using thulium [143] at ~1900 nm and holmium [61] at ~2000 nm. These laser hosts have not yet been developed for single frequency, low noise operation, nor for use in GW detectors. Reliable master oscillators must also be developed. NPROs using these dopants have been developed in YAG hosts (see below) but the resultant wavelengths are not necessarily suitable for use in glass fiber lasers.

As of the time of writing, it appears that the application of high power fiber laser amplifiers in GW detection is promising, but will require research to combine the approaches for mitigating Spontaneous Brillouin Scattering (SBS) and mode instabilities with the simultaneous requirements for reliable single frequency, polarized, low noise operation and/or make use of coherent combination of individual lower power devices. Some work [52], indicates that SBS will not be an issue at 300 W but this has not been confirmed for the extremely narrow linewidths that the Voyager laser will require.

8.2 Requirements

8.2.1 Laser Power

The laser power requirement is derived from the ultimate power handling limits of the arm cavities in cryogenic configuration; we would maximize the laser power for the high frequency sensitivity and then use a combination of squeezing and heavy mirrors to reduce the low frequency radiation pressure noise.

This power limit is estimated in Section 4 to be 4 MW in the arm cavities. Table 8 gives a breakdown for the power levels throughout the interferometer. It may be possible to reduce the required power if we can increase the amount of power recycling by reducing losses in the arms.

	Power (Voyager Deep)	Power (iVoyager)	Temperature (K)
Laser Output	290 W	88 W	300
IMC Input	270 W	80 W	300
IMC Output	200 W	60 W	300
BS	2.8 kW	840 W	300
Arm Cavity	3.9 MW	1.2 MW	123

TABLE 8: A breakdown for the power levels throughout the high power regions of the interferometer. The 300 W laser power level required for Voyager Deep will be achieved via coherent combination of high power lasers [14].

8.2.2 Noise requirements

The noise requirements (intensity, frequency and beam jitter noise) are still to be determined using a full closed-loop model of the interferometer that includes a Finesse based simulation of IFO response coupled to a model of the MIMO length sensing and control system. This is a complex and lengthy modeling task. In lieu of this being completed, initial estimates of the intensity and frequency but not jitter, noise requirements are constructed in a similar fashion to aLIGO.

The use of crystalline materials increases the risk of birefringence. As such, polarization noise needs to be considered more carefully than for aLIGO.

Intensity noise The relative intensity noise requirements for the LIGO Voyager laser can be defined in a similar manner to those for aLIGO:

- **Control band: 0.1 – 10 Hz**. The intensity noise induced radiation pressure motion should be below the equivalent ISI motion or less than $0.01/\sqrt{\text{Hz}}$, which ever is smaller.
- **GW band: 10 – 2000 Hz**. Radiation pressure from intensity noise will couple to DARM via power imbalance through the two arms. Assuming a power imbalance of 1%. The residual displacement noise must be at least 10x lower than the target displacement noise curve.
- **GW band: > 2 kHz**. The noise on the residual RF sidebands that reach the detection photodiodes must be at least 10x lower than the shot noise from the carrier.

For relative intensity noise, the main differences between Voyager and aLIGO are the change in the stored arm power, the increased mass of the test-masses and the transition to a balanced homodyne readout, the latter allowing for significant reduction of amplitude noise through common mode noise rejection.

Frequency noise The frequency noise requirements for the laser are determined in the following way:

1. **Establish suppression of frequency noise using the common mode control servo**. An excellent description of the topology of this servo is given in Evan Hall's thesis [56] and also in a series of documents by Kiwamu Izumi and Daniel Sigg [68, 69]. The goal of this step is to essentially brute-force adapt the common-mode servo to LIGO Voyager with the only tuning being adjustments to the various open-loop transfer functions of cavities that are different from aLIGO (due to changes in the finesse of those cavities).
2. **Establish transfer function of the residual frequency noise to the DARM signal** on the anti-symmetric side of the interferometer. This is achieved using a Finesse model of the interferometer along with various assumptions (given below) about differences in optical parameters (losses, BS reflectivity, ITM reflectivities, ITM ROC, etc) that cause common mode noise to couple to the anti-symmetric port.

Polarization noise Polarization noise has been explored for the silicon substrates to set the limit on allowable polarization noise in the test masses [100]. The backpropagation of this requirement to the symmetric input port of the PSL to determine the input laser polarization noise requirement is still TBD.

8.3 Technical Details

Much of the technical details for the LIGO Voyager laser are largely unresolved. The topology of the laser is likely to be similar to the aLIGO MOPA design with a low noise seed laser and two or three subsequent amplifier stages:

1. Low noise seed laser (approximately 50 mW output)
2. Low power amplifier stage (approximately 1 – 5 W output)
3. Medium power amplifier stage (approximately 10 – 50 W output)
4. High power amplifier stage (approximately 100W output)
5. Coherent combination of lasers for 300W output [14].

It is expected that we will use thulium doping for the amplifiers as this covers the wavelength range 1900 – 2050 nm.

8.3.1 Possible seed laser architectures

There are three main technologies that are being consider:

- **NPRO:** This is not a widely developed architecture for this wavelength range. However, this architecture typically provides excellent output power, polarization stability and high-speed frequency control. These laser also typically have a narrow linewidth and low frequency noise in the RF band.

- **Fiber laser source:** Fiber-Bragg grating laser sources are easily manufactured and tuned for a given wavelength. They provide reasonable output power. They do not, inherently, allow for fast frequency control without additional opto-electronics. Their inherent frequency noise is not well known. Can be polarization selective.
- **DFB diode laser sources:** Relatively low cost. Minimal output power (10mW-50mW range). Fiber coupled output. Polarization stability is unknown. Fast frequency control is possible via feedback to the current supply of the laser. Relatively low frequency noise [9].

8.3.2 Amplifier stages

As of this writing in 2024, Advanced LIGO is operating with around half of the initial design input power (125 W into the PRM). To embrace this phased approach, we will likely utilize coherent beam combination [14], with each of the amplifiers having an output power of ~75 – 100 W.

8.4 Unresolved issues

- Exact topology (fiber/free space interface). We have yet to determine the exact configuration of free-space/fiber sources and where interfaces will be.
- Coherent beam recombination meeting all requirements.
- Polarization control with fiber laser. Polarization selective fiber laser sources exist [15], but the control authority and requirements for polarization are uncertain.
- Fiber coupling issues with high power. We will require 300 W of CW laser power - how significant is this when coupling fibers together?

8.5 Development Approach & Timeline

8.5.1 Development Approach

Essentially, we are reusing as much as possible from the existing aLIGO system, meaning:

- KEEP all wavelength independent components, both physical (e.g. opto-mechanics) and abstract (e.g. engineering designs and procedures).
- REPLACE all wavelength dependent components (e.g. optics, opto-electronics, etc).

A nearly complete list of what we will keep and replace is detailed in Table 9.

KEEP	REPLACE
Laser enclosure/clean environment	Optics (mirrors/lenses/beamsplitters, wave plates, PMC mirrors)
Optical topology / equipment footprint	Electro-optics (photodiodes, EOMs, AOMs)
Electronics	Pump diodes
Optical table	Fiber optics
Engineering design	Laser source (master oscillator, mid-power amplifier, high-power stage)
Control strategy	Chillers
Data acquisition	Mode-matching layout
Opto-mechanics (mounts, PMC spacer, four-axis tilt aligners)	Output power control
Reference cavity vacuum	reference cavity mirrors
Digital control (remote control)	Internal controls
Laser safety procedures	Laser safety equipment
Facilities interfaces (electrical, environmental, plumbing)	

TABLE 9: List of the laser items to be kept and replaced

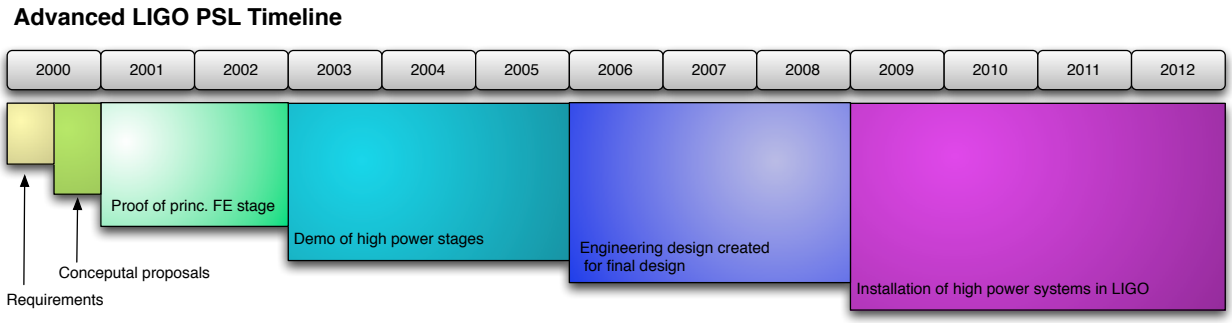

FIGURE 26: Advanced LIGO PSL development timeline.

8.5.2 Development Timeline

The aLIGO high power laser requirements are documented in G000121. The final design review for the aLIGO laser took place around 2010 (cf. T0900649 and Fig. 26). The installation was complete by the end of 2012. We use this framework as our baseline for estimating the development timeline for the LIGO Voyager laser.

The proposed timeline of laser development for the Voyager PSL is shorter than the aLIGO one, as illustrated in Fig. 27. We believe that by reusing most of the aLIGO PSL engineering and infrastructure, we can radically reduce the required engineering and the time required to install the equipment (for example, no new laser enclosures will need to be built).

The laser operation will be staged in a similar way to aLIGO: (T1200307):

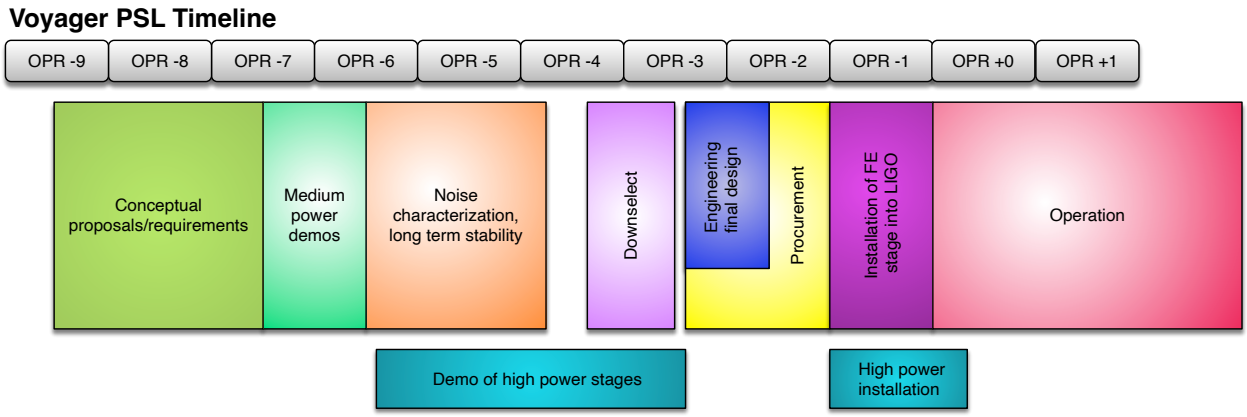

FIGURE 27: LIGO Voyager timeline for laser work.

1. starting at low power for a year or two
2. graduating to medium power for another 12 months
3. followed by an increase to full power

allowing for an additional 3 years or so from the start of 3rd generation commissioning until full power is required). As the high-power stage will not be needed for several years, we can develop this stage in parallel with the testing and engineering to expedite Voyager operations.

9 Quantum Noise Engineering

9.1 Overview

Future GW interferometers will be limited by quantum noise above ~ 10 Hz. Reductions of quantum noise (phase noise at high frequencies and radiation pressure fluctuations at low frequencies) will improve the GW sensitivity over nearly the entire detection band.

Extensive research has been carried out in the last decade to find solutions to reduce quantum noise in gravitational wave detectors complementary to increasing the laser power stored in the arm cavities. There are essentially two main (not exclusive) approaches that have been identified:

- Squeezed light [88] injection from the dark port
- interferometer optical topologies alternative to recycled Michelson interferometers.

After the demonstrations in GEO600 and in the H1 LIGO interferometer [3, 83], squeezing at 1064 nm is now a mature technology for application in gravitational wave detectors, and the use of frequency dependent squeezing has even spread the improvement to the radiation pressure dominated frequency band (10 – 100 Hz).

9.2 Requirements

High levels of squeezing covering the frequency band from 0.01 –10 kHz can be routinely generated at 1064 nm in an Optical Parametric Oscillator (OPO) by parametric down-conversion from 532 nm. In table top experiments, squeezing levels higher than 10 dB have been measured [136, 155]. However, the amount of *useful* squeezing is strongly dependent on the amount of loss that the squeezed beam encounters in the path from the squeezed light source to the measurement photodetector. In gravitational wave detectors, reducing these optical losses below 20% is a non-trivial practice, due to the large number of optical loss sources.

Based on the analysis described in [98] and the success of the filter cavity, the Voyager design relies on injection of frequency dependent squeezed light as a baseline solution to achieve a broadband reduction of quantum noise with respect to Advanced LIGO. The significant reduction in scatter loss which comes with increased wavelength, however, may yet drive the design towards something more complicated in the future: i.e. frequency dependent squeezing input may not be the optimum choice for low loss interferometers.

9.3 Technical Details

The design sensitivity curve shown in Fig. 3 is obtained by injection of 10 dB of pure squeezed state at 2000 nm into a 300 m long filter cavity with 10 ppm (cf. Fig. 53) round

trip loss. The losses between the squeezed light source and the interferometer are 5%, while the readout losses (common to the squeezed field and the interferometer signal field) are 5%.

9.3.1 Filter Cavities for Input Squeezing

In Advanced LIGO, quantum noise appears in two flavors: shot noise and radiation pressure (back-action) noise. Due to the Heisenberg Uncertainty Principle, reduction of high frequency quantum "shot noise" will correspond to an increase of low frequency quantum "radiation pressure" noise. Direct squeezed light injection [3, 83] will not, therefore, be suitable for LIGO Voyager. However, squeezed light can be manipulated so as to generate "frequency-dependent squeezing" by rotating the squeezed field relative to the interferometer field in a frequency dependent way. This can be achieved by reflecting the squeezed beam from a high finesse, detuned *filter cavity* before injection into the interferometer [77].

Filter cavities and their properties have been extensively studied theoretically [39, 58, 76]. The performance of a filter cavity can be described in terms of its intra-cavity losses per unit length. The lower the losses per unit length, the better the filter cavity is able to "rotate" the squeezing ellipse without degrading it.

Extensive work has gone into characterizing optical losses in high quality fused silica optics with IBS coatings. Absorption losses are typically less than 0.5 ppm; scatter losses are significantly higher and also depend on the laser beam spot size [66, 90]. Direct measurements report round-trip losses of 10 ppm (5 ppm per bounce) for beam spot sizes in the 1 – 3 mm range (corresponding to confocal lengths of 5 – 25 m range), giving losses per unit length of 0.5 ppm/m with a 20 m long filter cavity [66].

Frequency dependent squeezing at 1064 nm has been experimentally demonstrated in the kHz – MHz regime [24, 110] and in gravitational wave detectors at audio frequencies with a crossover frequency near 43 Hz [49]. Technical noise sources including phase noise, optical loss, and mode mismatch can limit the realistic performance of a filter cavity [79]. Ongoing work continues to characterize the noise coupling mechanisms for frequency dependent squeezing in existing gravitational wave detectors. Much of this development work translates directly into the development of a squeezing system for LIGO Voyager in the 1550 – 2000 nm band.

9.3.2 Loss Control

Every optical loss in the path from the squeezed light source to the measuring photodetector allows vacuum fluctuations to degrade the squeezed state. Reducing optical losses is the only way to ensure high levels of measured squeezing. Moreover, phase noise between the squeezed field and the interferometer field also becomes a loss mechanisms [37].

The following are the components which introduce most of the losses observed in

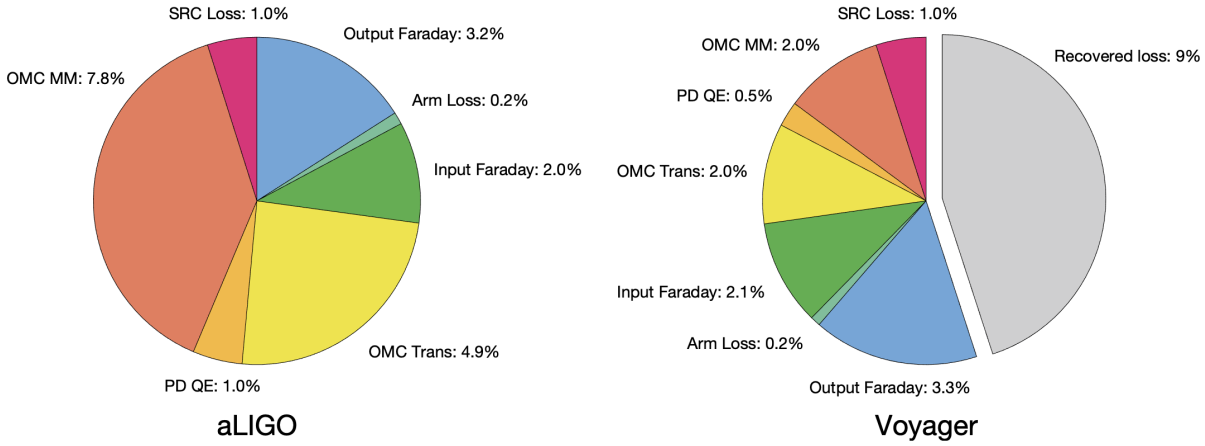

FIGURE 28: Breakdown of sources of quantum decoherence. On the left, the circa 2017 losses (total = 20%) in aLIGO. On the right, the estimated losses (total = 11%) for LIGO Voyager.

Component	Adv LIGO	Adv LIGO +	Voyager
SQZ Input Faraday	2.1	0.5-1%	2%
Arm Loss	0.2	0.2%	0.2%
Output Faraday	3.3	0.5-1%	3.3%
SRC Loss	1.0	1%	1%
OMC MM	8.0	2.5%	2%
OMC Trans	5.0	2%	2%
PD QE	1%	2%	0.5%
Phase Noise	~ 15 mrad	20 mrad	20 mrad

TABLE 10: Optical Losses which limit the measured squeezing improvement.

squeezing injection into the interferometers (fused silica, 1064 nm):

- mode mismatch (squeezed beam to OMC)
- OMC throughput
- polarizing components (Faradays rotators, polarized beam splitters)
- photodetector efficiency
- OPO internal losses

To achieve 10% total losses, as currently assumed in the LIGO Voyager baseline curve, all of these loss sources need to be of the order of 1 – 3%. This seems feasible, albeit with some development required in the next several years:

1. InGaAs photodetectors with extremely high quantum efficiency at 1550 nm (QE > 99%) are already available [95]. Either extended InGaAs or a suitable replacement

detector for 2 μm with a QE > 99% will need to be developed. Alternatively, optical domain pre-amplification either through homodyne phase-sensitive amplification or sum frequency generation could permit use of existing lower QE photodiodes at 2 um or high QE photodiodes at shorter wavelength, respectively [10, 21]. SFG is more described in Section 9.3.3.

2. Faraday isolators for 1550 nm are commercially available and have typical throughput of 95%. 98%-99% loss single passes are required. There is no fundamental limit here; as before with aLIGO, we will have to work with vendors to develop and select high efficiency components.

3. Losses in the OMC and the OPO need to be below 2 – 3%. The throughput of the aLIGO OMCs during the O2 run were 96 – 97%. It is expected that the losses will decrease by a factor of ~ 2 with the longer wavelength. Low loss OPOs for 1.5 – 2.2 μm squeezing are under development [93] within the LSC.

A more thorough accounting of losses as they are related to mode matching and wavefront correction is contained in the Active Wavefront Correction whitepaper (T1500188).

9.3.3 Nonlinear upconversion

Sum-frequency generation (SFG) provides an alternative path for high QE photodetection. By mixing a strong (e.g. resonantly enhanced) pump, for example at 1064 nm, the 2 µm fields may be upconverted to 700 nm. After upconversion, traditional InGaAs or Si PDs may be used to achieve ≥ 99% QE. Light upconversion for improved photodetection has been demonstrated and exploited in other applications including imaging [11], environmental monitoring [96], and quantum enhanced sensing [158]. Work on similar schemes has been considered and conducted within the LIGO collaboration, namely led by M. M. Fejer [40]. Figure 29 shows a schematic for a pump-resonant SFG scheme using

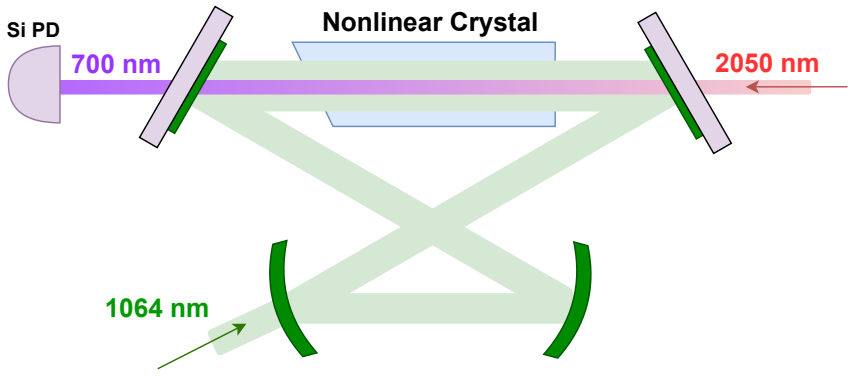

FIGURE 29: Bowtie cavity for pump resonant SFG upconversion. A 2 micron signal passes once through a nonlinear crystal with strong pump intensity. The output can be upconverted to 700 nm with near-unity efficiency.

a $\chi^{(2)}$ nonlinear crystal embedded in a bowtie cavity for maximum single-pass upcon-

version efficiency. Because the signal is not resonant, it has no cavity mode-matching requirements, and its upconversion efficiency depends solely on its overlap with the circulating pump intensity. With a modestly low power seed < 1 W, a pump finesse of ≤ 1000 should provide enough optical gain to achieve an SFG QE of ≥ 95% [72, 73, 103, 142] thus overcoming the native PD QE limits.

Loss mechanism	$L/2$ at λ_s	$L/2$ at λ_o	Total
Bulk absorption [81]	300 ppm	500 ppm	800 ppm
Fresnel scattering	≤ 1000 ppm	≤ 1000 ppm	≤ 2000 ppm
Coating absorption	≤200 ppm	≤200 ppm	≤400 ppm
Total	**1500 ppm**	**1700 ppm**	**3200 ppm**

TABLE 11: Estimated quantum inefficiencies for a 2 cm long PPLN crystal.

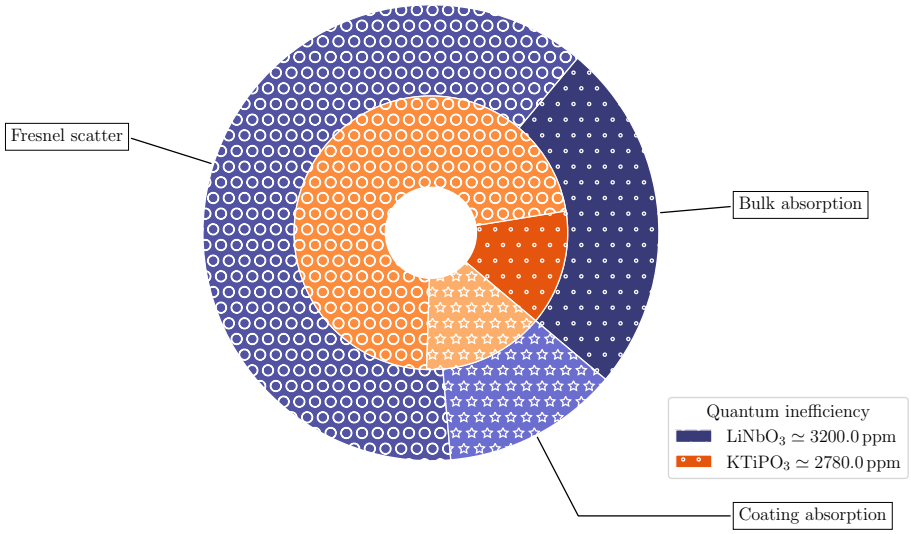

FIGURE 30: SFG upconversion for improved photodetection

Loss mechanism	$L/2$ at λ_s	$L/2$ at λ_o	Total
Bulk absorption [8]	100 ppm	280 ppm	380 ppm
Fresnel scattering	≤ 1000 ppm	≤ 1000 ppm	≤ 2000 ppm
Coating absorption	≤200 ppm	≤200 ppm	≤400 ppm
Total	**1300 ppm**	**1480 ppm**	**2780 ppm**

TABLE 12: Estimated quantum inefficiencies for a 2 cm long PPKTP crystal.

The fundamental quantum inefficiency stems from the various loss channels experienced by upconverting photons, including the nonlinear crystal bulk absorption, coating absorption [8, 81], inelastic bulk scattering [51, 116, 131], and Fresnel (surface) scattering. Considering a 20 mm long periodically poled lithium niobate (PPLN) and potassium

titanyl phosphate (PPKTP) crystals, we estimate loss budgets for the two crystal types in Figure 30 using the numbers from Table 11, and Table 12. The estimated maximum theoretical SFG QE is 99.68% for PPLN and 99.72% for PPKTP assuming near-perfect pump beam overlap, and AR coated crystal faces with $R \leq 0.1\%$, nearly approaching the extrinsic Si devices QE [164].

9.4 Unresolved issues

The above filter cavity loss of 10 ppm has not been witnessed before in LIGO suspended cavities, but has been demonstrated in cavities of a ~few m length. One of the key pieces of research is to demonstrate the reduction of scatter loss which comes from the increased wavelength, both for small beams ($< 1\,cm$) and for large beams ($> 5\,cm$).

9.5 Development Approach & Timeline

9.5.1 Squeezed Light generation for 1800–2200 nm

The baseline Voyager design includes a laser with a wavelength in the 1800 – 2200 nm range (cf. § 8 and § 10). The generation of squeezed light in this wavelength band is not yet as well as established for 1064 and 1550 nm, but it is expected that 10-15 dB of squeezing can be achieved with several years of R&D. Figure 31 shows the evolution of squeezing technology at a few different wavelengths over time to give some perspective on the history.

The on-going effort to establish an improved squeezed light source and control scheme for the squeezed beam relative to the interferometer beam (P1400064) will inform the final design for the LIGO Voyager squeezed light source.

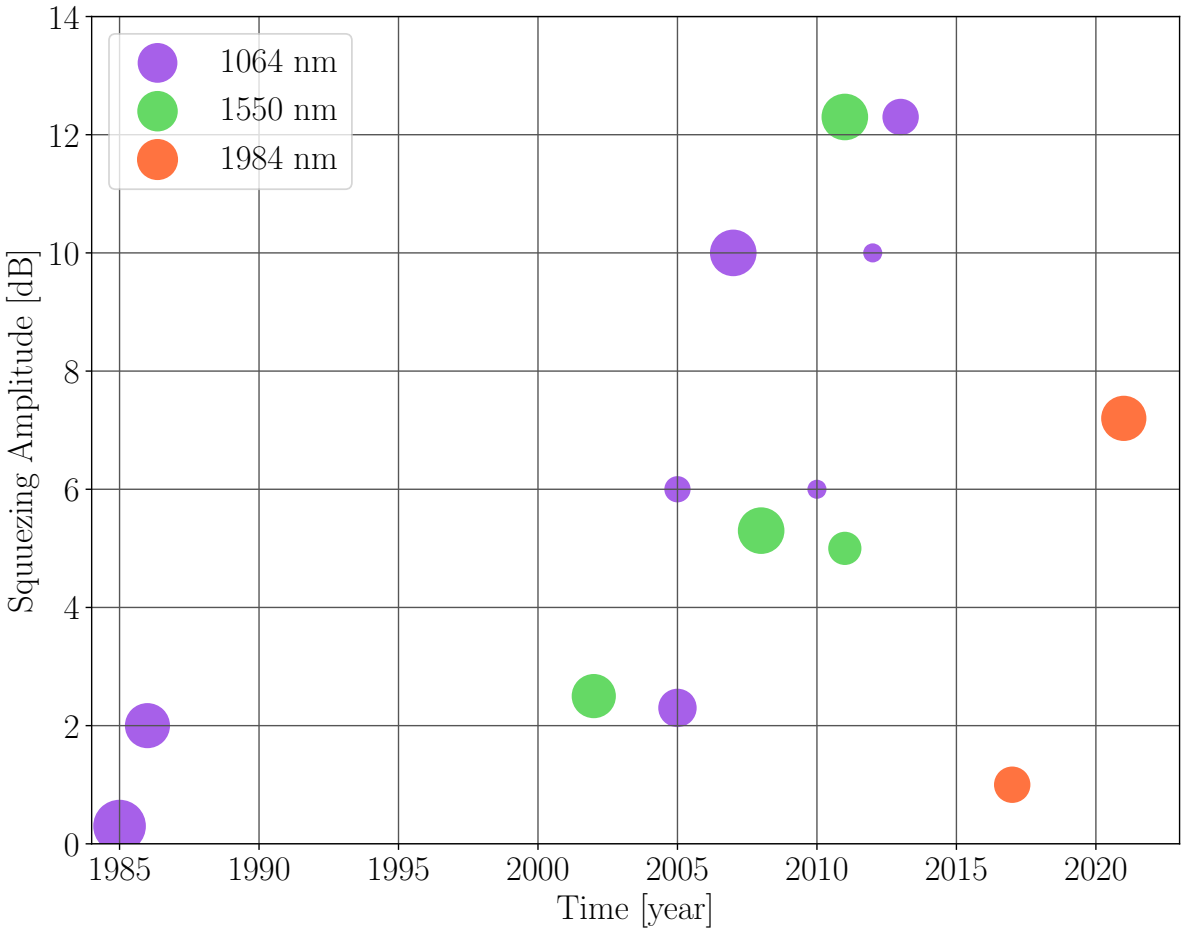

FIGURE 31: Squeezing amplitude for various audio frequencies and laser wavelengths as a function of time over the past 30 years. The area of each circle is proportional to the log of the frequency at which the noise reduction was measured.

10 Choice of Laser Wavelength

The baseline operating wavelength of 2050 nm has been chosen by balancing several competing drivers. In Section 10.1 below, we go into detail on these criteria.

10.1 Wavelength Choice Considerations

Contents

10.1.1 Quantum noise

One of the primary effects of changing the wavelength is in the quantum noise.

Ignoring all complicating factors related to materials and scattering, the quantum noise curve (including radiation pressure backaction and shot noise) scales with the wavelength in the following way:

Increasing the wavelength by a factor of 2, *decreases* the radiation pressure noise and *increases* the shot noise contribution to the phase noise by a factor of 2 (in units of strain/rHz). So, 1 MW at 1 micron is equivalent to 2 MW at 2 microns.

This quantum noise picture alone is too naive, and so we have to include thermal noise, power handling, backscatter, and other factors to get the whole picture.

10.1.2 Absorption in test masses

The absorption of the laser power in the test mass substrate and mirror coatings (c.f. Section 3.3.1), along with the cryogenic cooling capacity (Section 4.3.1), determines the actual arm cavity power.

The substrate absorption actually increases with wavelength, which would favor 1550 nm over our choice of 2050 nm.

The coating absorption is the dominant heat load on the mirrors, and so the minimization of the overall absorption drives the choice to ~2 microns. This is largely due to the strong wavelength dependence in the absorption of the high-index amorphous silicon layer (see Fig. 32).

10.1.3 Coating Thermal Noise

For longer wavelengths, the coating will be thicker, and so the thermal noise ASD will increase as $\lambda^{1/2}$ (assuming no changes in materials). That would be a 15% increase going from 1550 to 2000 nm. This *might* be significant driver towards 1550 nm, but is too small of an effect to be considered in choosing among 2050 and 2128 nm. Coating thermal noise is not a significant determiner of the laser wavelength.

10.1.4 Photodetection quantum efficiency

The quantum efficiency for 1550 nm is very high in standard InGaAs. The quantum efficiency of InGaAs for longer wavelengths can be tuned by adjusting the In/Ga ratio (Fig. 33), however, this leads to strain in the material due to lattice mismatch. The strain creates defects in the lattice during the growth, with the result being a greatly increased dark noise level (Fig. 34),.

Alternatively, nonlinear downconversion of the signal light into higher optical frequency using sum frequency generation is considered as a promising technology. Details are described in Section 9.3.3.

10.1.5 Optical (scatter) loss

The optical scatter loss does not have an appreciable difference between 1.9 and 2.1 microns, so is not a strong determiner of the laser wavelength in the 2 micron band.

Here we consider optical losses and their dependence on the laser wavelength. In most cases, the scatter loss dominates over the absorption loss[8], so we will not consider absorption here. Optical losses affect the interferometer sensitivity in a number of ways:

1. power recycling gain: clipping losses in the DRMI and scatter losses in the arm cavities influence the overall carrier buildup
2. squeezing: losses experienced by the squeezed field injected from the dark port limit the squeeze factor
3. differential arm cavity loss -> contrast defect -> laser noise coupling
4. scattered light -> backscatter noise (cf. Appendix E)

[8] cf. Section 7, Section 3.3.1, and Appendix D for more on absorption

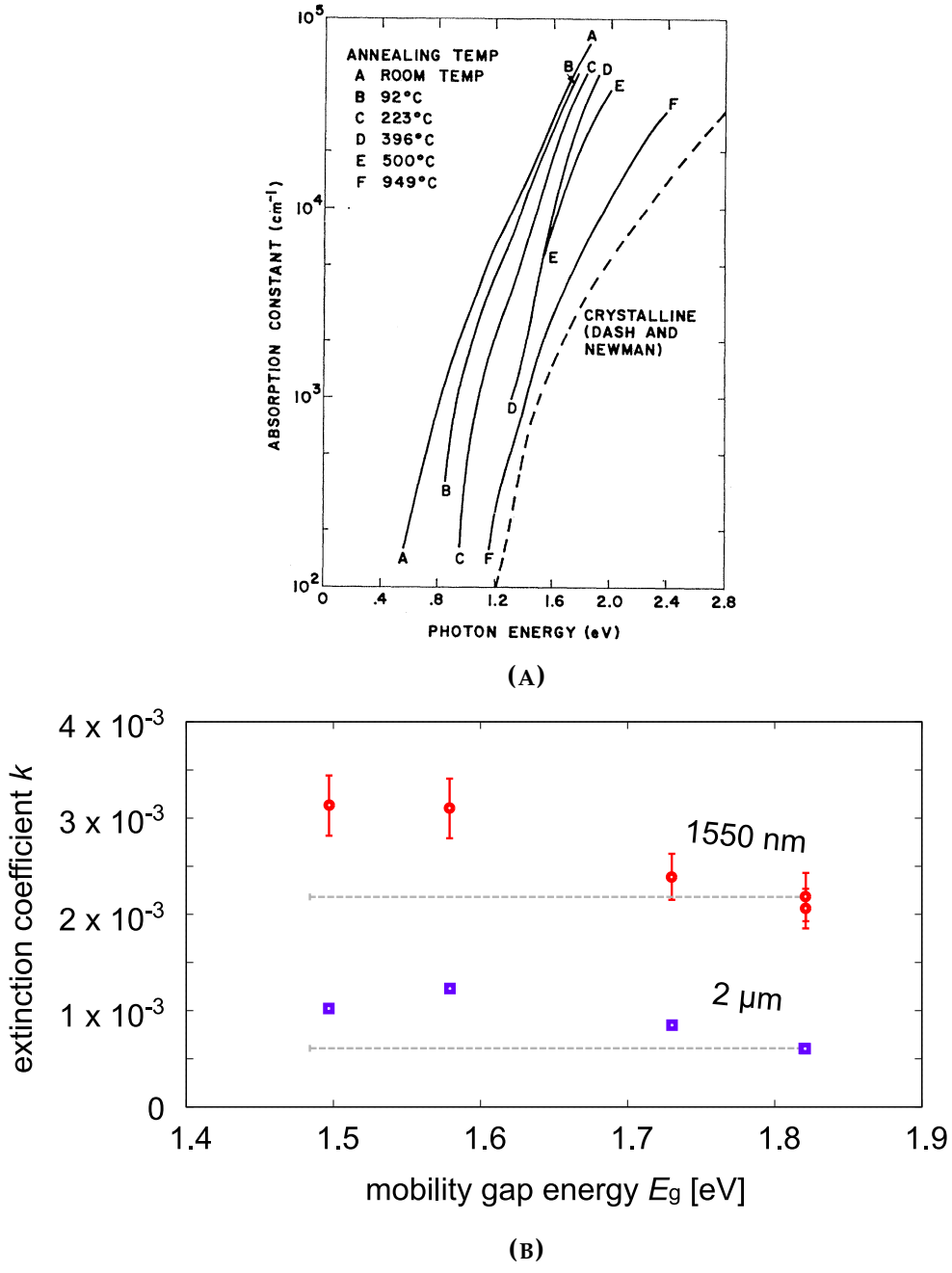

FIGURE 32: (A) Absorption spectra of various amorphous silicon films [18], illustrating the material's steep wavelength dependence and sensitivity to sample preparation conditions. (B) Wavelength comparison between 1550 and 2000 nm in amorphous silicon samples across a range of mobility gap energies [147].

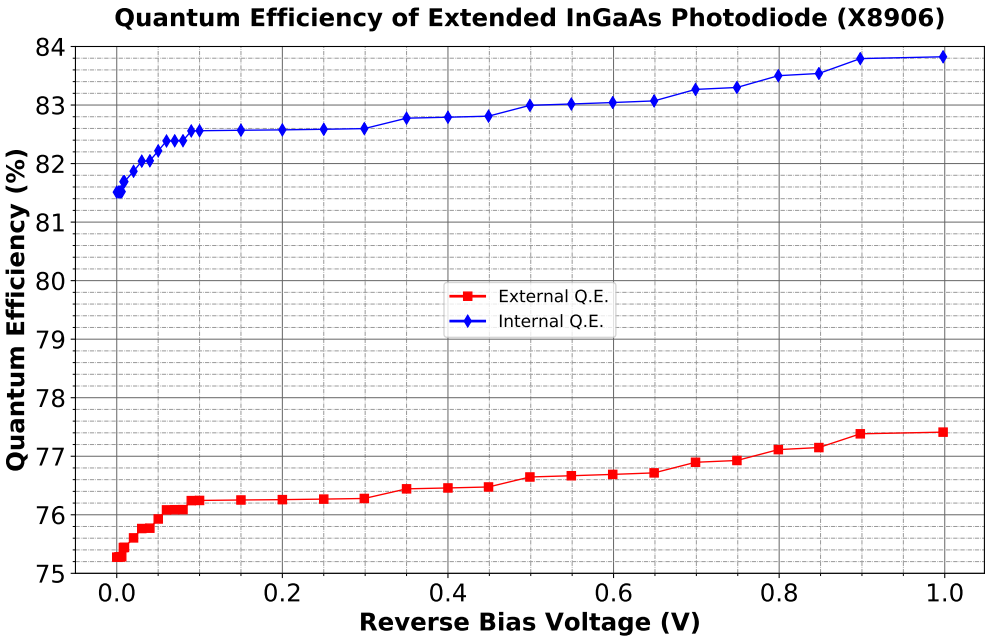

FIGURE 33: Example measurement of the quantum efficiency for an exInGaAs photodiode at 2 µm[132]. Photodiode: Laser Components IG22X2000T9. Wavelength 2004 nm. Measurement temperature: room temperature.

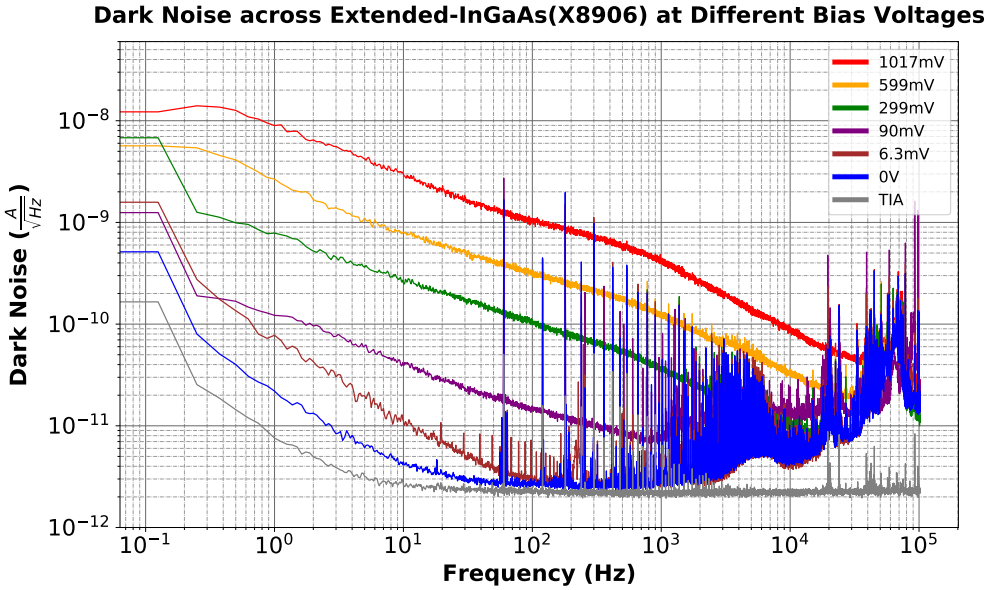

FIGURE 34: Example measurement of the dark noise levels for an exInGaAs photodiode with various bias voltages[132]. Photodiode: Laser Components IG22X2000T9. Measurement temperature: room temperature.

Overall, transitioning from 1 to 2 microns is beneficial to interferometer performance in several ways (cf. Appendix E):

- the wide angle scatter loss is due mainly to microroughness and is expected to scale as $1/\lambda^2$, according the the Golden Rule.
- This allows for a higher power recycling gain, reducing the requirements on the input laser power.
- lower wide angle backscatter noise,
- lower loss in the arm cavity
- lower small angle noise (less backscatter from the beam tube)
- a lower loss in the squeezing filter cavity

This assumes that the figure and roughness of the silicon mirrors is comparable to that of the existing aLIGO optics, but this has yet to be shown.

10.1.6 Clipping loss

What is the maximum beam size on the mirrors? This is *increased* to minimize the thermal noise, but *decreased* to reduce the angular and parametric instabilities.

10.1.7 Residual gas noise

The wavelength dependence of the polarizability of H_2 is quite weak as it is for most molecules [9]. The main dependence is related to the beam geometry. Holding the beam size on the test masses fixed, the beam profile in the arm cavities has a wavelength dependence.

The ultimate sensitivity of Voyager would be limited by the residual H_2 in the arms. We are currently exploring the idea of pumping along the beam tube at multiple points in a manner similar to what has been proposed for Cosmic Explorer (for similar reasons).

10.1.8 Sigg-Sidles angular instabilities

Going to large (100 – 200 kg) masses, moves all of the unstable modes into the stable regime, and so this effect does not influence the wavelength choice (cf. Section 11.2)

- Absorption (ppm/cm) vs wavelength
- Fundamental to SiO_2

[9] However, see Appendix F for some subtleties with water

  - Heavier molecular weights have lower energy mechanical modes
  - Have lower phonon energies
  - Pushes out multi-phonon absorption edge

10.2 Laser amplifier issues

- Peak in emission spectrum is around 2015 nm.
- Emission at 2128 nm requires a lot of pumping and filtering of ASE to get amplification of 2128 nm

10.3 2040 nm vs 2050 nm

- Holmium doped amplifiers rule at 2 um, but their efficiency drops fast after 2100 nm; therefore 2128 nm may be problematic for Voyager.
- Better suited wavelength that can use existing amplifier technologies near 2.05 um.

10.4 Laser sources at 2050 nm

- Fiber laser
  - NP Photonics: 2 Micron Fiber Laser Source (25 mW, < 50 kHz linewidth)
  - RMPC: MFL-2 (< 40 W, < 70 GHz linewidth)
- Fiber laser
  - Free space laser diodes (suitable for ECDL). Frankfurt Laser Co (15mW, 5MHz linewidth)
  - Fiber coupled: Eblana (2mW, no linewidth specified)

10.5 Summary of Wavelength Choice

Considering all of these criteria, we have chosen 2050 nm as a baseline wavelength.

If a suitable coating can be found which has an HR stack absorption of 1 ppm or less at 1550 nm, then the Voyager design could change to this wavelength with a very little change in the sensitivity curves. Using a more standard laser wavelength would be advantageous for technical reasons having to do with cameras and IR cards, and would increase the commissioning speed.

11 Systems and auxiliary issues

11.1 Systems

The Systems design of Voyager is, in most respect, identical to aLIGO and A+, as summarized in T010075 and M1800040 respectively.

The major subsystems, including the cryogenic subsystem, which is the most notable addition, have already been described in the respective sections. Here we provide a brief overview of a few more subsystems.

11.1.1 Facility

- The cryocoolers and LN2 reservoirs will occupy LVEA space. They'll need some level of vibration isolation.
- The facility will need the plumbing for the LN2 supply.

11.1.2 Vacuum

- The vacuum system will need retrofitting to be compatible with the cryo system.
- How much acceleration will we gain for the initial pumping speed due to the cryopumping?
- Need to add ETM Transmon chamber. (See Figure Fig. 20)

11.1.3 Physical Environment Monitor

- Deploy more PEM sensors along with the cryogenics and cryocoolers.

11.1.4 Interferometer Sensing and Control

- The existing ISC system is adequate, except for the optical sensors.
- exInGaAs sensors can be used at 2 µm. They need to be inspected with regard to the noise level and the dark current in DC applications. In addition to that in RF applications, junction capacitance, response time, noise level at RF must be inspected.

11.2 Opto-Mechanical Angular Instability

Optical power, circulating in the arm cavities, applies torque on the mirrors and changes the dynamics of the suspended mirrors [33, 65, 130].

The magnitude of this radiation pressure induced optical torque depends upon the optical power and g-factors of the cavities. The circulating power acts as a spring with either positive or negative stiffness. The sign of the feedback depends on the misalignment mode. In the case when two test masses have equal radius of curvature, a tilt of the axis produces a restoring torque; if the optical axis shifts, then radiation pressure torque tends to further misalign the mirrors. In one case the torque induced by radiation pressure makes the suspension mode stiffer (hard), while in the other case it tends to make the mode less stiff (soft).

Fig. 35 shows the eigenfrequencies of hard and soft modes for different power levels. Here the nominal laser wavelength of 2000 nm for Voyager and 1064 nm for Advanced LIGO is assumed. When the optical power is high enough, the soft mode becomes unstable. A robust feedback control loop should have enough bandwidth to suppress the instability. Simulations show that if the frequency of the unstable mode is f_{soft}, then the bandwidth of the control loop needs to be ~3 f_{soft}, and significant filtering of the sensing noise (~ $60\,dB$) can be achieved at ~ $10 f_{soft}$. Since the frequency of the soft mode is less than 1 Hz for the Voyager design at 3 MW, sensing noise from angular loops should not limit the sensitivity.

If the cavity g-factor approaches 1, then instability occurs at higher power. At the same time, the beam size on the optic increases and the coupling of angular motion to power fluctuations become more significant. Table 13 summarizes these parameters for different cavity g-factors in the range of 0.1 – 0.9 and intracavity power of 3 MW. Angle $\Delta\alpha_{FP}$ shows the sensitivity of the cavity power to angular fluctuations. If the mirror is misaligned by this angle, then the resonating power is reduced from the maximum to zero in the Fabry-Perot configuration. In the full lock with coupled cavities, this angle is smaller by a factor of ~6. For Advanced LIGO $\Delta\alpha_{FP} \approx 3.2\,\mu rad$.

The parameter, f_{HOM}, denotes the transverse mode frequency spacing, and can be optimized to avoid excitation of parametric instabilities in the arm cavities. The clipping loss, computed per test mass, becomes significant if the beam size approaches 9 cm (for a mirror radius is 22.5 cm).

The hard/soft frequencies are functions only of the cavity g-factors, and not explicitly the laser wavelength. However, if the laser beam spot size on the mirrors is kept to a maximum value, ω_{max}, due to clipping losses, then the cavity g-factor will be smaller for

g-factor	Waist [cm]	Beam size [cm]	Clipping loss [ppm]	f_{soft} [Hz]	$\Delta\alpha_{FP}$ [urad]	f_{HOM} [kHz]
0.9	1.4	9.0	4	-0.10	3.2	3.84
0.7	1.9	6.8	0	-0.16	7.2	6.92
0.5	2.3	6.0	0	-0.21	10.6	9.4
0.3	2.6	5.5	0	-0.27	13.7	11.8
0.1	3.0	5.2	0	-0.36	16.5	14.9

TABLE 13: List of optical parameters v. g-factor for mirror masses of 143 kg

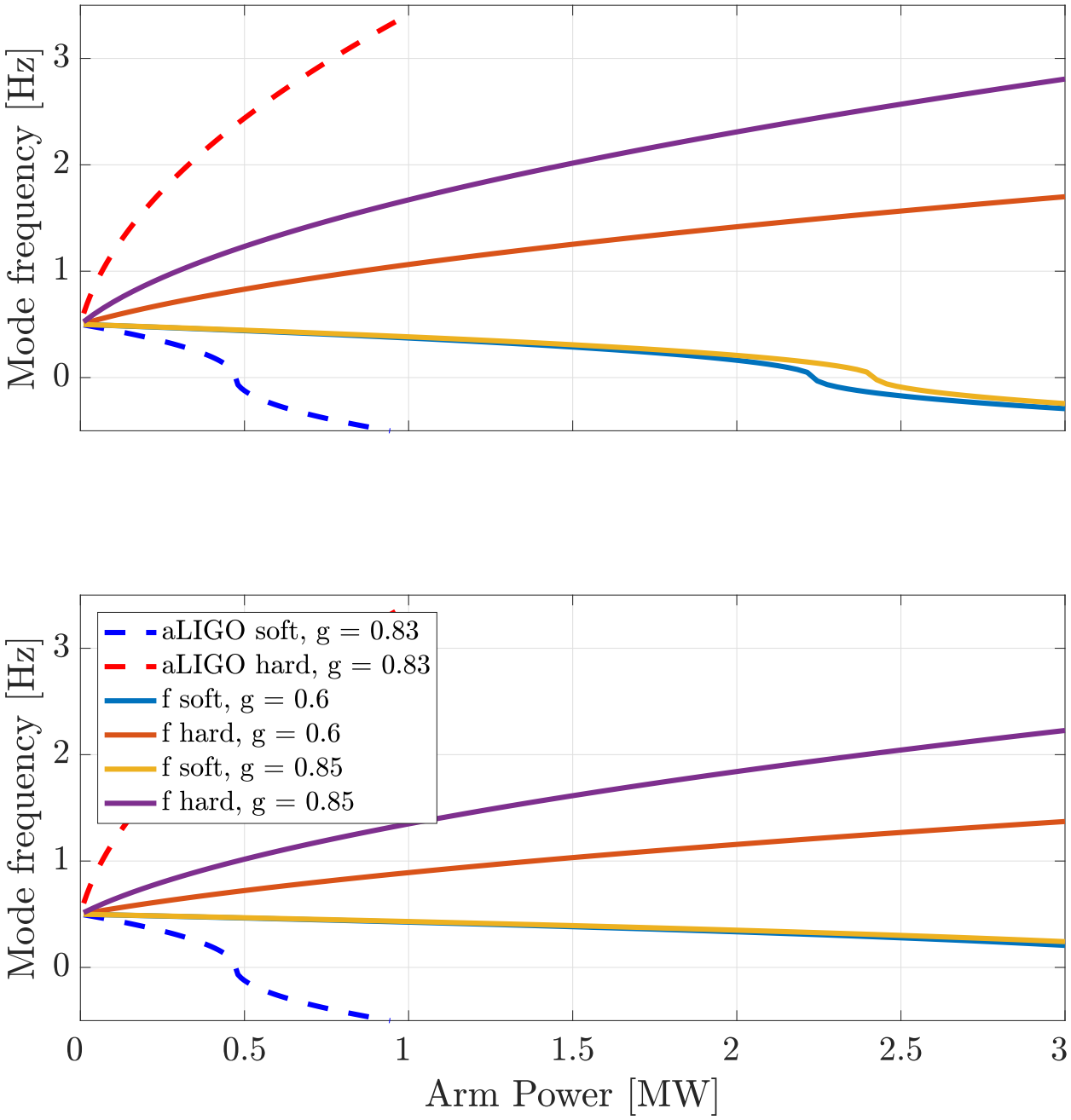

FIGURE 35: Frequencies of the hard and soft modes vs. arm power for various g-factors. Radii of curvature of input and end test masses are set to be the same in this simulation. Upper plot show the instability for a mirror of 40 cm thickness (143 kg) and the lower plot a mirror of 50 cm thickness (200 kg).

a longer wavelength. Stated another way, if the beam spot size is maximized to reduce the thermal noise, the longer wavelength results in a somewhat less unstable interferometer.

This is not a very strong effect.

11.2.1 Auxiliary Optics System

- **Sensor Cards:** Sensor cards that operate at 2 µm exist, but they are temperature-based and have a weak and slow response.
- **Beam profiler:** Scanning-slit type beam profiler with an InGaAs PD works very well with the 2 um beam.
- **Image sensors:** Regular CCDs have no sensitivity at 2 µm. HgCdTe imagers are commercially available, but they are expensive.
- 2050 nm **laser for testing:** For simple table-top tests, commercial fiber coupled 2050 nm lasers are available. For the noise sensitive tests, 2050 nm ECDL can be useful, although the gain chip (light source) is not easily available and requires custom production.

11.2.2 Computer and Data Systems

- Basically, we can keep using what we have now.
- Advancements in digital technology have expanded the range of applications for digital control to the high frequency end. We should explore the use of the high speed digital control in the fast loops like PI/ISS/FSS/Common mode servo/Digital mod-demod and so on.

11.3 Issues that span multiple subsystems

11.3.1 Parametric Instabilities

The LIGO Voyager baseline design has an arm cavity power of 4 MW. With such a high stored power level, acousto-optic parametric instabilities can potentially become more troublesome than for lower power, room temperature interferometers.

An ANSYS model (from S. Gras) first computes the complex mechanical impedance of the mirrors. This model includes mechanical losses due to the coatings on the HR, AR, and barrel surfaces. The baseline dimensions of the Voyager test mass have been used.

The optical model considers the round-trip optical gain, including scatter losses and clipping losses inside the arm cavities, as well as the optical transmissivities of the nominal Voyager design (cf. Table 14).

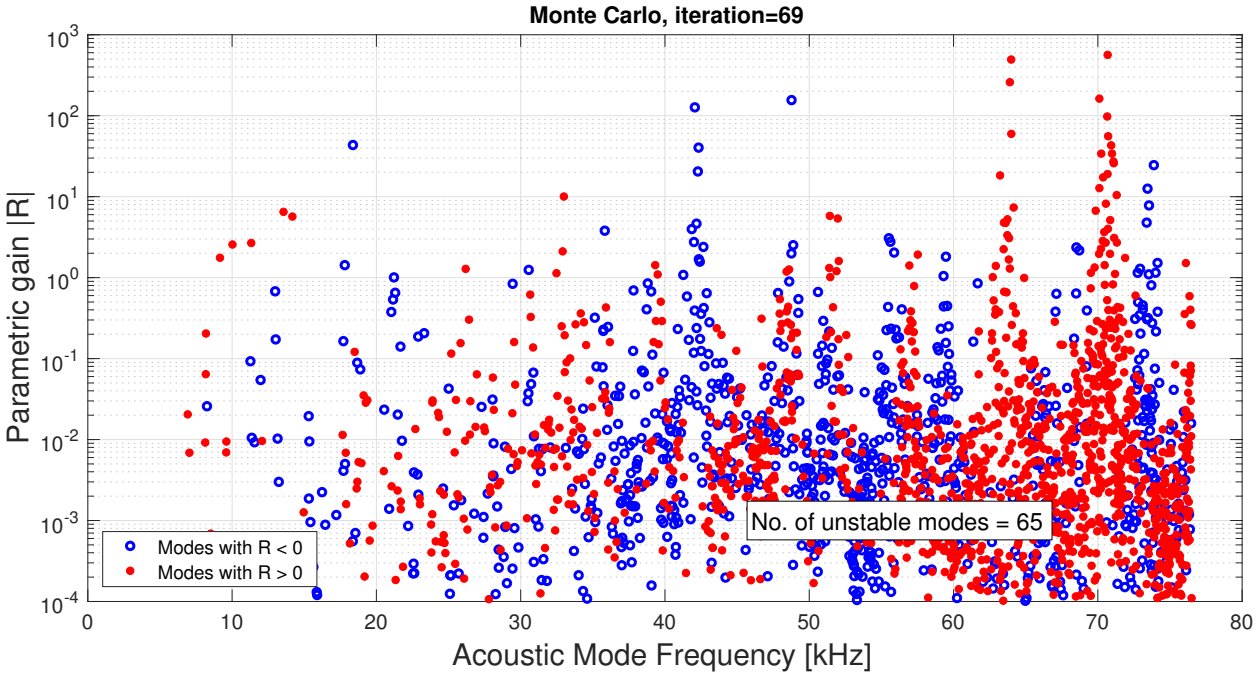

FIGURE 36: Estimation of parametric gain for all of the opto-mechanical modes for LIGO Voyager. All of the modes with positive gain (RED) greater than unity are considered to be unstable. For this simulation, random perturbations have been added to the RoC of the test mass optics.

Mitigation Strategies

- Conventional AMDs
- Better AMDs
- Ohmic damping
- Gouy phase tuning

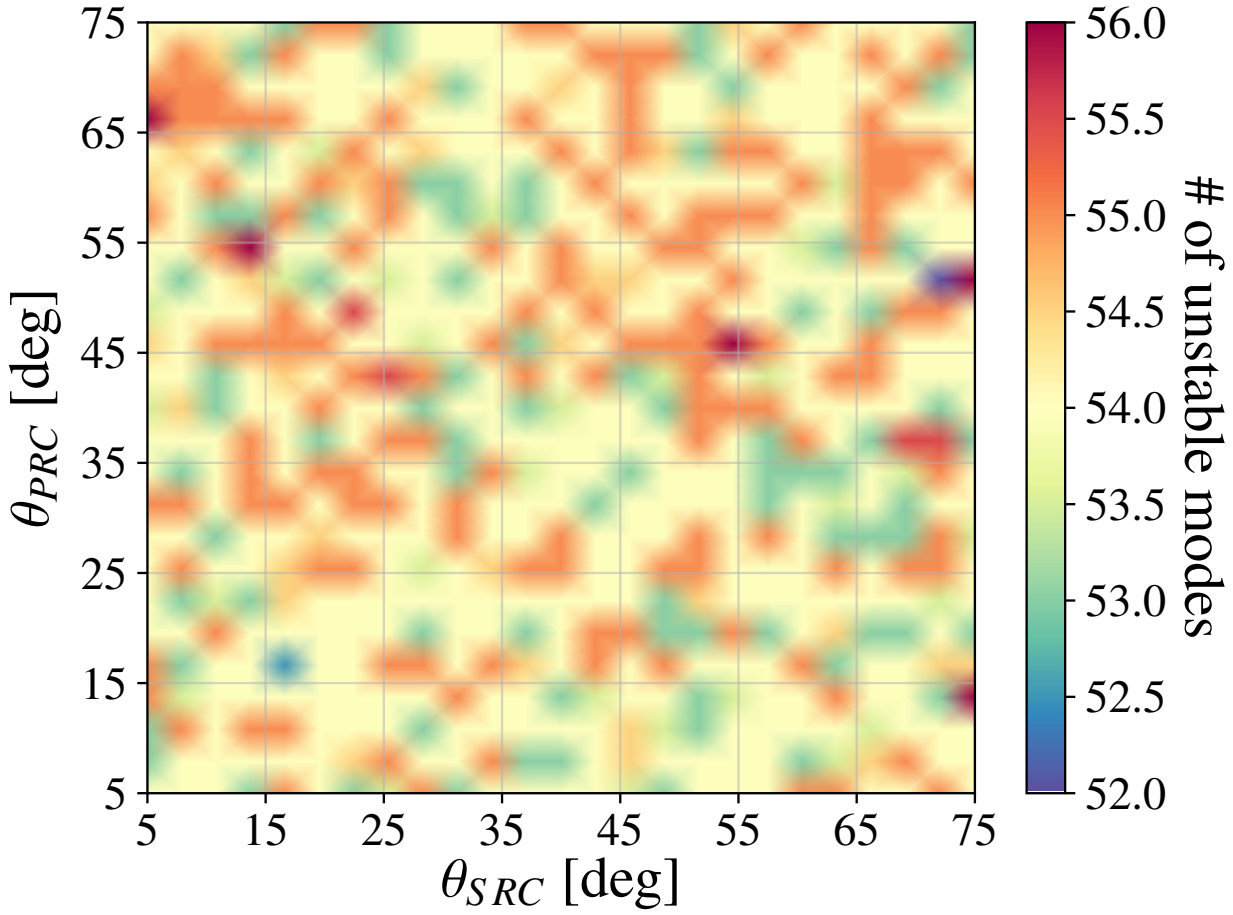

FIGURE 37: Estimation of number of unstable PI modes as a function of the PRC and SRC Gouy phase. There is a less than 10% effect on the number of unstable modes by changing the Gouy phase.

References

[1] URL https://git.ligo.org/voyager/voyagergwinc/-/tree/master/VoyagerBS.

[2] Aarik L. *Mechanical properties of crystalline and amorphous aluminum oxide thin films grown by atomic layer deposition*. *Surface & Coatings Technology* (2022).

[3] Aasi J *et al.* *Enhancing the sensitivity of the LIGO gravitational wave detector by using squeezed states of light*. *Nature Photon.*, 7:613–619 (2013). URL http://dx.doi.org/10.1038/nphoton.2013.177. 1310.0383.

[4] Abernathy MR, Smith N, Korth WZ, Adhikari RX, Prokhorov LG, Koptsov DV, and Mitrofanov VP. *Measurement of mechanical loss in the Acktar Black coating of silicon wafers*. *Classical and Quantum Gravity*, 33 (18):185002 (2016). URL http://stacks.iop.org/0264-9381/33/i=18/a=185002.

[5] Alshourbagy M, Toncelli A, Tonelli M, and Marchetti F. *Silicon crystal fibers: difficulties and progress*. *Crystal Research and Technology*, 42 (7):641–647 (2007). URL http://dx.doi.org/10.1002/crat.200610881.

[6] Amico P, Bosi L, Gammaitoni L, *et al.* *Monocrystalline fibres for low thermal noise suspension in advanced gravitational wave detectors*. *Classical and Quantum Gravity*, 21 (5):S1009–S1013 (2004). URL http://dx.doi.org/10.1088/0264-9381/21/5/094.

[7] Anthony FM. *High heat load optics: an historical overview*. *Optical Engineering*, 34 (2):313 (1995). URL http://dx.doi.org/10.1117/12.194032.

[8] Ast S, Nia RM, Schönbeck A, Lastzka N, Steinlechner J, Eberle T, Mehmet M, Steinlechner S, and Schnabel R. *High-efficiency frequency doubling of continuous-wave laser light*. *Opt. Lett.*, 36 (17):3467–3469 (2011). URL http://dx.doi.org/10.1364/OL.36.003467.

[9] Bagheri M, Spiers GD, Frez C, Forouhar S, and Aflatouni F. *Linewidth Measurement of Distributed-Feedback Semiconductor Lasers Operating Near 2.05 μm*. *IEEE Photonics Technology Letters*, 27 (18):1934–1937 (2015). URL http://dx.doi.org/10.1109/LPT.2015.2447286.

[10] Bai Y, Venugopalan G, Kuns K, Wipf C, Markowitz A, Wade AR, Chen Y, and Adhikari RX. *Phase-sensitive optomechanical amplifier for quantum noise reduction in laser interferometers*. *Phys. Rev. A*, 102:023507 (2020). URL http://dx.doi.org/10.1103/PhysRevA.102.023507.

[11] Barh A, Rodrigo PJ, Meng L, Pedersen C, and Tidemand-Lichtenberg P. *Parametric upconversion imaging and its applications*. *Adv. Opt. Photon.*, 11 (4):952–1019 (2019). URL http://dx.doi.org/10.1364/AOP.11.000952.

[12] Bilderback DH, Freund AK, Knapp GS, and Mills DM. *Journal of Synchrotron Radiation*, (2):53–60. URL http://dx.doi.org/10.1107/S0909049500000650.

[13] Birney R, Cumming AV, Campsie P, *et al.* *Coatings and surface treatments for enhanced performance suspensions for future gravitational wave detectors*. *Classical and Quantum Gravity*, 34 (23):235012 (2017). URL http://dx.doi.org/10.1088/1361-6382/aa9354.

[14] Bode N, Holmes Z, Ng S, von Behren B, Ottaway D, and Willke B. *Multiple beam coherent combination via an optical ring resonator*. *Opt. Lett.*, 48 (17):4717–4720 (2023). URL http://dx.doi.org/10.1364/OL.500684.

[15] Bolingbroke G. *Single frequency thulium fiber lasers between 1900 nm and 2050 nm [GWADW 2023]*. Technical report, University of Adelaide, https://dcc.ligo.org/LIGO-G2301122-v1 (2023).

[16] Bonilla E. *Progress on the practical integration of cryogenics to gravitational-wave detectors*. Ph.D. thesis, Stanford University (2022). URL https://searchworks.stanford.edu/view/14237911.

[17] Bristow AD, Rotenberg N, and van Driel HM. *Two-photon absorption and Kerr coefficients of silicon for 850–2200nm*. *Applied Physics Letters*, 90 (19):191104 (2007).

[18] Brodsky MH, Title RS, Weiser K, and Pettit GD. *Structural, Optical, and Electrical Properties of Amorphous Silicon Films*. *Phys. Rev. B*, 1:2632–2641 (1970). URL http://dx.doi.org/10.1103/PhysRevB.1.2632.

[19] Brooks AF, Abbott B, Arain MA, *et al.* *Overview of Advanced LIGO adaptive optics*. *Appl. Opt.*, 55 (29):8256–8265 (2016). URL http://dx.doi.org/10.1364/AO.55.008256.

[20] Brooks, Aidan, et al. *Point absorbers in Advanced LIGO*. *Applied Optics*, 60:4047–4063 (2021). URL http://dx.doi.org/10.1364/AO.419689.

[21] Carcoba F. *SFG for high quantum efficiency photodetection at 2 um*. Technical report, LIGO, https://dcc.ligo.org/LIGO-G2301240 (2023).

[22] Cella G. *Off-Line Subtraction of Seismic Newtonian Noise*. In *Recent Developments in General Relativity*, pp. 495–503. Springer Milan (2000). URL http://dx.doi.org/10.1007/978-88-470-2113-6_44.

[23] Cella G, Sannibale V, DeSalvo R, Márka S, and Takamori A. *Monolithic geometric anti-spring blades*. *Nuclear Instruments and Methods in Physics Research Section A: Accelerators, Spectrometers, Detectors and Associated Equipment*, 540 (2-3):502–519 (2005). URL http://dx.doi.org/10.1016/j.nima.2004.10.042.

[24] Chelkowski S, Vahlbruch H, Hage B, Franzen A, Lastzka N, Danzmann K, and Schnabel R. *Experimental characterization of frequency-dependent squeezed light*. *Phys. Rev. A*, 71:013806 (2005). URL http://dx.doi.org/10.1103/PhysRevA.71.013806.

[25] Chen PY, Tsai MH, Yeh WK, Jing MH, and Chang Y. *Relationship between wafer edge design and its ultimate mechanical strength*. *Microelectronic Engineering*, 87 (11):2065–2070 (2010). URL http://dx.doi.org/10.1016/j.mee.2009.12.083.

[26] Cheng JL, Rioux J, and Sipe JE. *Full band structure calculation of two-photon indirect absorption in bulk silicon*. *Applied Physics Letters*, 98 (13):131101 (2011).

[27] Ciszek T and Wang T. *Growth and properties of silicon filaments for photovoltaic applications*. In *Conference Record of the Twenty Sixth IEEE Photovoltaic Specialists Conference - 1997*, pp. 103–106. IEEE, Anaheim, CA, USA (1997). URL http://dx.doi.org/10.1109/PVSC.1997.653935.

[28] Cumming AV, Cunningham L, Hammond GD, Haughian K, Hough J, Kroker S, Martin IW, Nawrodt R, Rowan S, Schwarz C, and van Veggel AA. *Silicon mirror suspensions for gravitational wave detectors*. *Classical and Quantum Gravity*, 31 (2):025017 (2014). URL http://dx.doi.org/10.1088/0264-9381/31/2/025017.

[29] Degallaix J, Flaminio R, Forest D, Granata M, Michel C, Pinard L, Bertrand T, and Cagnoli G. *Bulk optical absorption of high resistivity silicon at 1550 nm*. *Optics letters*, 38 (12):2047 (2013).

[30] Degallaix J, Komma J, Forest D, Hofmann G, Granata M, Heinert D, Schwarz C, Nawrodt R, Pinard L, Michel C, Flaminio R, and Cagnoli G. *Measurement of the optical absorption of bulk silicon at cryogenic temperature and the implication for the Einstein Telescope*. *Classical and Quantum Gravity*, 31 (18):185010 (2014).

[31] Della Valle F, Milotti E, Ejlli A, Gastaldi U, Messineo G, Piemontese L, Zavattini G, Pengo R, and Ruoso G. *Extremely long decay time optical cavity*. *Optics Express*, 22 (10):11570–11577 (2014).

[32] DelRio FW, Cook RF, and Boyce BL. *Fracture strength of micro- and nano-scale silicon components*. *Applied Physics Reviews*, 2 (2):021303 (2015). URL http://dx.doi.org/10.1063/1.4919540.

[33] Dooley KL, Barsotti L, Adhikari RX, Evans M, Fricke TT, Fritschel P, Frolov V, Kawabe K, and Smith-Lefebvre N. *Angular control of optical cavities in a radiation-pressure-dominated regime: the Enhanced LIGO case*. *Journal of the Optical Society of America A*, 30:2618 (2013). URL http://dx.doi.org/10.1364/JOSAA.30.002618. 1310.3662.

[34] Driggers JC, Harms J, and Adhikari RX. *Subtraction of Newtonian noise using optimized sensor arrays*. *Phys. Rev. D*, 86:102001 (2012). URL http://dx.doi.org/10.1103/PhysRevD.86.102001.

[35] Duffy J William. *Acoustic quality factor of aluminum alloys from 50 mK to 300 K*. *Journal of Applied Physics*, 68 (11):5601–5609 (1990). URL http://dx.doi.org/10.1063/1.346971. https://pubs.aip.org/aip/jap/article-pdf/68/11/5601/8014810/5601_1_online.pdf.

[36] Duffy W. *Acoustic quality factor of copper, brass and beryllium copper from 50 mK to 300 K*. *Cryogenics*, 32 (12):1121–1124 (1992). URL http://dx.doi.org/https://doi.org/10.1016/0011-2275(92)90325-5.

[37] Dwyer S, Barsotti L, Chua SSY, *et al. Squeezed quadrature fluctuations in a gravitational wave detector using squeezed light*. *Opt. Express*, 21 (16):19047–19060 (2013). URL http://dx.doi.org/10.1364/OE.21.019047.

[38] Euser TG and Vos WL. *Spatial homogeneity of optically switched semiconductor photonic crystals and of bulk semiconductors*. *Journal Of Applied Physics*, 97 (4):043102 (2005).

[39] Evans M, Barsotti L, Kwee P, Harms J, and Miao H. *Realistic filter cavities for advanced gravitational wave detectors*. *Physical Review D*, 88 (2):022002 (2013).

[40] Fejer MM. *Nonlinear Optical Frequency Conversion*. *Physics Today* (1994).

[41] Flanagan EE and Thorne KS. *Scattered-Light Noise for LIGO*. Technical Report T950102, LIGO (1995). URL https://dcc.ligo.org/LIGO-T950102/public.

[42] Fowle A, Haggerty J, Perron R, Strong P, and Swanson J. *Float-zone processing in a weightless environment*. Technical report, NASA (1976).

[43] Franck R. *Cryogenic emissivity properties of Ball Infrared Black*. *AIP Conference Proceedings*, 1434 (2012).

[44] Frey BJ, Leviton DB, and Madison TJ. *Temperature-dependent refractive index of silicon and germanium*. In E Atad-Ettedgui, J Antebi, and D Lemke, eds., *Optomechanical Technologies for Astronomy*. SPIE (2006). URL http://dx.doi.org/10.1117/12.672850.

[45] Frey BJ, Leviton DB, and Madison TJ. *Temperature-dependent refractive index of silicon and germanium*. In *Society of Photo-Optical Instrumentation Engineers (SPIE) Conference Series*, volume 6273 of *Society of Photo-Optical Instrumentation Engineers (SPIE) Conference Series*, p. 2 (2006). URL http://dx.doi.org/10.1117/12.672850. physics/0606168.

[46] Fricke TT, Smith-Lefebvre ND, Abbott R, Adhikari R, Dooley KL, Evans M, Fritschel P, Frolov VV, Kawabe K, Kissel JS, Slagmolen BJJ, and Waldman SJ. *DC readout experiment in Enhanced LIGO*. *Classical and Quantum Gravity*, 29 (6):065005 (2012). URL http://dx.doi.org/10.1088/0264-9381/29/6/065005. 1110.2815.

[47] Fritschel P, Evans M, and Frolov V. *Balanced homodyne readout for quantum limited gravitational wave detectors*. *Optics express*, 22 (4):4224–4234 (2014).

[48] Fritschel P, Gonzalez G, Lantz B, Saha P, and Zucker M. *High power interferometric phase measurement limited by quantum noise and application to detection of gravitational waves*. *Physical review letters*, 80 (15):3181 (1998).

[49] Ganapathy D, Jia W, Nakano M, *et al.* *Broadband Quantum Enhancement of the LIGO Detectors with Frequency-Dependent Squeezing*. *Phys. Rev. X*, 13:041021 (2023). URL http://dx.doi.org/10.1103/PhysRevX.13.041021.

[50] Glassbrenner C and Slack GA. *Thermal conductivity of silicon and germanium from 3 K to the melting point*. *Physical Review*, 134 (4A):A1058 (1964).

[51] Golubovia A, Gajia R, Hinia I, and Aepanovia MA. *IR and Raman spectra of poled and unpoled LiNbO3 single crystals*. *Journal of Alloys and Compounds*, 460 (1):74–78 (2008). URL http://dx.doi.org/https://doi.org/10.1016/j.jallcom.2007.06.036.

[52] Goodno GD, Book LD, and Rothenberg JE. *Low-phase-noise, single-frequency, single-mode 608 W thulium fiber amplifier*. *Opt. Lett.*, 34 (8):1204–1206 (2009). URL http://dx.doi.org/10.1364/OL.34.001204.

[53] Götz W, Pensl G, Zulehner W, Newman RC, and McQuaid SA. *Thermal donor formation and annihilation at temperatures above 500°C in Czochralski-grown Si*. *Journal of Applied Physics*, 84 (7):3561–3568 (1998). URL http://dx.doi.org/10.1063/1.368586. https://doi.org/10.1063/1.368586.

[54] Green M. *Silicon Solar Cells: Advanced Principles & Practice*. Centre for Photovoltaic Devices and Systems (1995).

[55] Gysin U, Rast S, Ruff P, Meyer E, Lee DW, Vettiger P, and Gerber C. *Temperature dependence of the force sensitivity of silicon cantilevers*. *Phys. Rev. B*, 69:045403 (2004). URL http://dx.doi.org/10.1103/PhysRevB.69.045403.

[56] Hall E. *Long-baseline laser interferometry for the detection of binary black-hole mergers*. Ph.D. thesis, California Institute of Technology (2016). URL http://resolver.caltech.edu/CaltechTHESIS:01302017-113507797.

[57] Harms J. *Terrestrial Gravity Fluctuations*. *Living Reviews in Relativity*, 18 (1) (2015). URL http://dx.doi.org/10.1007/lrr-2015-3.

[58] Harms J, Chen Y, Chelkowski S, Franzen A, Vahlbruch H, Danzmann K, and Schnabel R. *Squeezed-input, optical-spring, signal-recycled gravitational-wave detectors*. *Physical Review D*, 68 (4):042001 (2003).

[59] Harvard University. *HITRAN: high-resolution transmission molecular absorption database*.

[60] Hasegawa K, Akutsu T, Kimura N, Saito Y, Suzuki T, Tomaru T, Ueda A, and Miyoki S. *Molecular adsorbed layer formation on cooled mirrors and its impacts on cryogenic gravitational wave telescopes*. *Phys. Rev. D*, 99 (2):022003 (2019). URL http://dx.doi.org/10.1103/PhysRevD.99.022003.

[61] Hemming A, Simakov N, Davidson A, Oermann M, Corena L, Stepanov D, Carmody N, Haub J, Swain R, and Carter A. *Development of high-power holmium-doped fibre amplifiers*. In S Ramachandran, ed., *Fiber Lasers XI: Technology, Systems, and Applications*, volume 8961, p. 89611A. International Society for Optics and Photonics, SPIE (2014). URL http://dx.doi.org/10.1117/12.2042963.

[62] Henry JA, Wang Y, Sengupta D, and Hines MA. *Understanding the Effects of Surface Chemistry on Q: Mechanical Energy Dissipation in Alkyl-Terminated (C_1–C_{18}) Micromechanical Silicon Resonators*. *The Journal of Physical Chemistry B*, 111 (1):88–94 (2007). URL http://dx.doi.org/10.1021/jp0654011.

[63] Hild S, Chelkowski S, Freise A, Franc J, Morgado N, Flaminio R, and DeSalvo R. *A xylophone configuration for a third-generation gravitational wave detector*. *Classical and Quantum Gravity*, 27 (1):015003 (2010). URL http://dx.doi.org/10.1088/0264-9381/27/1/015003.

[64] Hines MA. *In Search of Perfection: Understanding the Highly Defect-Selective Chemistry of Anisotropic Etching*. *Annual Review of Physical Chemistry*, 54 (1):29–56 (2003). URL http://dx.doi.org/10.1146/annurev.physchem.54.011002.103849.

[65] Hirose E, Kawabe K, Sigg D, Adhikari R, and Saulson PR. *Angular instability due to radiation pressure in the LIGO gravitational-wave detector*. *Appl. Opt.*, 49 (18):3474–3484 (2010).

[66] Isogai T, Miller J, Kwee P, Barsotti L, and Evans M. *Loss in long-storage-time optical cavities*. *Optics express*, 21 (24):30114–30125 (2013).

[67] Izumi K, Arai K, Barr B, *et al. Multicolor cavity metrology*. *Journal of the Optical Society of America A*, 29:2092 (2012). 1205.1257.

[68] Izumi K, Sigg D, and Kawabe K. *Frequency Response of the aLIGO Interferometer: part2*. Technical report, LIGO Scientific Collaboration (2015). URL https://dcc.ligo.org/LIGO-T1500461/public.

[69] Izumi K, Sigg D, and Kawabe K. *Frequency Response of the aLIGO Interferometer: part3*. Technical report, LIGO Scientific Collaboration (2015). URL https://dcc.ligo.org/LIGO-T1500559/public.

[70] Kauder L. *Spacecraft Thermal Control Coatings References*. Technical report, NASA, https://ntrs.nasa.gov/citations/20070014757 (2005).

[71] Kawado S, Maruyama T, Suzuki T, Isawa N, and Hoshi K. *Crystal Perfection of Silicon Single Crystals Grown by the Magnetic-Field-Applied Czochralski Method*. *Journal of The Electrochemical Society*, 133 (1):171–174 (1986). URL http://dx.doi.org/10.1149/1.2108515.

[72] Kerdoncuff H, Christensen JB, Brasil TB, Novikov VA, Polzik ES, Hald J, and Lassen M. *Cavity-enhanced sum-frequency generation of blue light with near unity conversion efficiency*. *Opt. Express*, 28 (3):3975–3984 (2020). URL http://dx.doi.org/10.1364/OE.385826.

[73] Kerdoncuff H, Christensen JB, Brasil TB, Novikov VA, Polzik ES, Hald J, and Lassen M. *Cavity-enhanced sum-frequency generation of blue light with near unity conversion efficiency*. *Opt. Express*, 28 (3):3975–3984 (2020). URL http://dx.doi.org/10.1364/OE.385826.

[74] Kessler T, Hagemann C, Grebing C, Legero T, Sterr U, Riehle F, Martin MJ, Chen L, and Ye J. *A sub-40-mHz-linewidth laser based on a silicon single-crystal optical cavity*. *Nat Photon*, 6 (10):687–692 (2012). URL http://dx.doi.org/10.1038/nphoton.2012.217.

[75] Kestner B. *Zygo on Silicon*. personal communication (2012).

[76] Khalili FY. *Optimal configurations of filter cavity in future gravitational-wave detectors*. *Phys. Rev. D*, 81:122002 (2010). URL http://dx.doi.org/10.1103/PhysRevD.81.122002.

[77] Kimble HJ, Levin Y, Matsko AB, Thorne KS, and Vyatchanin SP. *Conversion of conventional gravitational-wave interferometers into quantum nondemolition interferometers by modifying their input and/or output optics*. *Phys. Rev. D*, 65:022002 (2001).

[78] Kissinger G. *Oxygen Precipitation in Silicon*. In *Defects and Impurities in Silicon Materials*, pp. 273–341. Springer Japan (2015).

[79] Kwee P, Miller J, Isogai T, Barsotti L, and Evans M. *Decoherence and degradation of squeezed states in quantum filter cavities*. *Phys. Rev. D*, 90 (6):062006 (2014). URL http://dx.doi.org/10.1103/PhysRevD.90.062006. 1704.03531.

[80] Lam CC and Douglass DH. *Observation of oxygen impurities in single-crystal silicon by means of internal friction*. *Journal of Low Temperature Physics*, 44 (3-4):259–264 (1981). URL http://dx.doi.org/10.1007/BF00120776.

[81] Leidinger M, Fieberg S, Waasem N, hnemann FK, Buse K, and Breunig I. *Comparative study on three highly sensitive absorption measurement techniques characterizing lithium niobate over its entire transparent spectral range*. *Opt. Express*, 23 (17):21690–21705 (2015). URL http://dx.doi.org/10.1364/OE.23.021690.

[82] Leviton DB and Frey BJ. *Temperature-dependent absolute refractive index measurements of synthetic fused silica*. *ArXiv e-prints* (2008). 0805.0091.

[83] LIGO Scientific Collaboration, Abadie J, Abbott BP, Abbott R, Abbott TD, Abernathy M, Adams C, Adhikari R, Affeldt C, Allen B, and et al. *A gravitational wave observatory operating beyond the quantum shot-noise limit*. *Nature Physics*, 7:962–965 (2011). URL http://dx.doi.org/10.1038/nphys2083.

[84] Liu X, Queen DR, Metcalf TH, Karel JE, and Hellman F. *Hydrogen-Free Amorphous Silicon with No Tunneling States*. *Physical Review Letters*, 113 (2):025503 (2014).

[85] Lockerbie NA. *Gravitational quadrupolar coupling to equivalence principle test masses: the general case*. *Classical and Quantum Gravity*, 19 (8):2063–2077 (2002).

[86] Londos CA, Binns MJ, Brown AR, McQuaid SA, and Newman RC. *Effect of oxygen concentration on the kinetics of thermal donor formation in silicon at temperatures between 350 and 500°C*. *Applied Physics Letters*, 62 (13):1525–1526 (1993). URL http://dx.doi.org/10.1063/1.108628. https://doi.org/10.1063/1.108628.

[87] Lu Z and Kimbel S. *Growth of 450mm diameter semiconductor grade silicon crystals*. *Journal of Crystal Growth*, 318 (1):193–195 (2011). URL http://dx.doi.org/https://doi.org/10.1016/j.jcrysgro.2010.10.122. The 16th International Conference on Crystal Growth (ICCG16)/The 14th International Conference on Vapor Growth and Epitaxy (ICVGE14).

[88] Lvovsky AI. *Squeezed light*. *arXiv.org* (2014). 1401.4118v1.

[89] Madau P and Dickinson M. *Cosmic Star-Formation History*. *Annual Review of Astronomy and Astrophysics*, 52 (1):415–486 (2014). URL http://dx.doi.org/10.1146/annurev-astro-081811-125615. https://doi.org/10.1146/annurev-astro-081811-125615.

[90] Magaña-Sandoval F, Adhikari RX, Frolov V, Harms J, Lee J, Sankar S, Saulson PR, and Smith JR. *Large-angle scattered light measurements for quantum-noise filter*

cavity design studies. *Journal of the Optical Society of America A*, 29:1722 (2012). URL http://dx.doi.org/10.1364/JOSAA.29.001722. 1204.2528.

[91] Magnozzi M, Bisio F, Gemme G, Granata M, Michel C, Pinard L, and Canepa M. *Detecting ultrathin ice on materials for optical coatings at cryogenic temperatures*. *J. Phys. D: Appl. Phys.*, 56 (47):475105 (2023). URL http://dx.doi.org/10.1088/1361-6463/acef35.

[92] Maloney P. *Emissivity of microstructured silicon*. *Optica*, 49 (2010).

[93] Mansell GL, McRae TG, Altin PA, Yap MJ, Ward RL, Slagmolen BJJ, Shaddock DA, and McClelland DE. *Observation of Squeezed Light in the* 2 μm *Region*. *Phys. Rev. Lett.*, 120:203603 (2018). URL http://dx.doi.org/10.1103/PhysRevLett.120.203603.

[94] Markosyan A and Bell A. *Optical properties of a float-zone rectified and Czochralski grown in a steady magnetic field crystalline Si*. Technical report, LIGO Scientific Collaboration (2017). URL https://dcc.ligo.org/LIGO-G1700480.

[95] Mehmet M, Ast S, Eberle T, Steinlechner S, Vahlbruch H, and Schnabel R. *Squeezed light at 1550 nm with a quantum noise reduction of 123 dB*. *Optics Express*, 19 (25):25763 (2011).

[96] Meng L, Fix A, Wirth M, gstedt LH, Tidemand-Lichtenberg P, Pedersen C, and Rodrigo PJ. *Upconversion detector for range-resolved DIAL measurement of atmospheric CH4*. *Opt. Express*, 26 (4):3850–3860 (2018). URL http://dx.doi.org/10.1364/OE.26.003850.

[97] Metcalf TH, Liu X, and Abernathy MR. *Improving the mechanical quality factor of ultra-low-loss silicon resonators*. *Journal of Applied Physics*, 123 (23):235105 (2018). URL http://dx.doi.org/10.1063/1.5027486.

[98] Miao H, Yang H, Adhikari RX, and Chen Y. *Quantum limits of interferometer topologies for gravitational radiation detection*. *Classical and Quantum Gravity*, 31 (16):165010 (2014). URL http://dx.doi.org/10.1088/0264-9381/31/16/165010. 1305.3957.

[99] Michel J and Kimerling L. *Electrical Properties of Oxygen in Silicon*. In R Willardson, AC Beer, and ER Weber, eds., *Oxygen In Silicon*, volume 42 of *Semiconductors and Semimetals*, chapter 7, pp. 251 – 287. Elsevier (1994). URL http://dx.doi.org/https://doi.org/10.1016/S0080-8784(08)60250-1.

[100] Michimura Y, Wang H, Salces-Carcoba F, Wipf C, Brooks A, Arai K, and Adhikari RX. *Effects of mirror birefringence and its fluctuations to laser interferometric gravitational wave detectors*. *Phys. Rev. D*, 109 (2):022009 (2024). URL http://dx.doi.org/10.1103/PhysRevD.109.022009. Publisher: American Physical Society.

[101] Middlemiss RP, Bramsiepe SG, Douglas R, Hild S, Hough J, Paul DJ, Samarelli A, Rowan S, and Hammond GD. *Microelectromechanical system gravimeters as a new tool for gravity imaging*. *Philosophical Transactions of the Royal Society A: Mathematical, Physical and Engineering Sciences*, 376 (2120):20170291 (2018). URL http://dx.doi.org/10.1098/rsta.2017.0291.

[102] Miller J, Barsotti L, Vitale S, Fritschel P, Evans M, and Sigg D. *Prospects for doubling the range of Advanced LIGO*. *Phys. Rev. D*, 91:062005 (2015). URL http://dx.doi.org/10.1103/PhysRevD.91.062005.

[103] Mimoun E, Sarlo LD, Zondy JJ, Dalibard J, and Gerbier F. *Sum-frequency generation of 589 nm light with near-unit efficiency*. *Opt. Express*, 16 (23):18684–18691 (2008). URL http://dx.doi.org/10.1364/OE.16.018684.

[104] Miyoki S, Tomaru T, Ishitsuka H, Ohashi M, Kuroda K, Tatsumi D, Uchiyama T, Suzuki T, Sato N, Haruyama T, Yamamoto A, and Shintomi T. *Cryogenic contamination speed for cryogenic laser interferometric gravitational wave detector*. *Cryogenics*, 41 (5):415–420 (2001). URL http://dx.doi.org/10.1016/S0011-2275(01)00084-4.

[105] Miyoki S, Uchiyama T, Tomaru T, *et al.* *Cryogenic contamination of an ultra-low loss mirror for cryogenic laser interferometric gravitational wave detector*. *Cryogenics*, 40 (1):61–66 (2000). URL http://dx.doi.org/10.1016/S0011-2275(00)00011-4.

[106] Murray PG, Martin IW, Craig K, Hough J, Robie R, Rowan S, Abernathy MR, Pershing T, and Penn S. *Ion-beam sputtered amorphous silicon films for cryogenic precision measurement systems*. *Physical Review D*, 92 (6):062001 (2015).

[107] Nawrodt R, Schwarz C, Kroker S, *et al.* *Investigation of mechanical losses of thin silicon flexures at low temperatures*. *Classical and Quantum Gravity*, 30 (11):115008 (2013). URL http://dx.doi.org/10.1088/0264-9381/30/11/115008.

[108] Nikogosyan DN. *Properties of Optical and Laser-Related Materials: A Handbook*. John Wiley & Sons (1997).

[109] Nordine PC, Veaux SC, and Wallenberger FT. *Silicon fibers produced by high-pressure LCVD*. *Applied Physics A Solids and Surfaces*, 57 (1):97–100 (1993). URL http://dx.doi.org/10.1007/BF00331224.

[110] Oelker, Eric, Isogai, Tomoki, Miller, John, Tse, Maggie, Barsotti, Lisa, Mavalvala, Nergis, and Evans, Matthew. *Audio-band frequency-dependent squeezing*. *arXiv*, quant-ph (2015).

[111] Orosco J. *Optical response of thin amorphous films to infrared radiation*. *Phys. Rev. B* (2018).

[112] Ottaway DJ, Fritschel P, and Waldman SJ. *Impact of upconverted scattered light on advanced interferometric gravitational wave detectors*. *Opt. Express*, 20 (8):8329–8336 (2012). URL http://dx.doi.org/10.1364/OE.20.008329.

[113] Pan HW. *Silicon nitride films fabricated by a plasma-enhanced chemical vapor deposition method for coatings of the laser interferometer gravitational wave detector*. *Phys. Rev. D*, 97 (2018).

[114] Pankove J. *Optical Processes in Semiconductors*. Dover books explaining science and mathematics. Dover (1971). URL https://books.google.com/books?id=HHM9Vo0DYZAC.

[115] Pearl S, Rotenberg N, and van Driel HM. *Three photon absorption in silicon for 2300–3300nm*. *Applied Physics Letters*, 93 (13):131102 (2008).

[116] Pelc JS, Ma L, Phillips CR, Zhang Q, Langrock C, Slattery O, Tang X, and Fejer MM. *Long-wavelength-pumped upconversion single-photon detector at 1550 nm: performance and noise analysis*. *Opt. Express*, 19 (22):21445–21456 (2011). URL http://dx.doi.org/10.1364/OE.19.021445.

[117] Pohl RO, Liu X, and Thompson E. *Low-temperature thermal conductivity and acoustic attenuation in amorphous solids*. *Rev. Mod. Phys.*, 74:991–1013 (2002).

[118] Qin H, Sutter P, and Zhou G. *The Crystallization of Amorphous Aluminum Oxide Thin Films Grown on NiAl(100)*. *Journal of the American Ceramic Society*, 97 (9):2762–2769 (2014).

[119] Reid S and Martin IW. *Development of mirror coatings for gravitational wave detectors*. *Coatings*, 6 (4):61 (2016).

[120] Rempe G, Thompson RJ, Kimble HJ, and Lalezari R. *Measurement of ultralow losses in an optical interferometer*. *Optics Letters*, 17:363–366 (1992). URL http://dx.doi.org/10.1364/OL.17.000363.

[121] Ridley BK. *Quantum Processes in Semiconductors*. Oxford University Press (2013). URL http://dx.doi.org/10.1093/acprof:oso/9780199677214.001.0001.

[122] Rowan S, Byer RL, Fejer MM, Route RK, Cagnoli G, Crooks DR, Hough J, Sneddon PH, and Winkler W. *Test mass materials for a new generation of gravitational wave detectors*. p. 292. Waikoloa, Hawai'i, United States (2003). URL http://dx.doi.org/10.1117/12.459019.

[123] Schilling R, Schnupp L, Winkler W, Billing H, Maischberger K, and Rudiger A. *A method to blot out scattered light effects and its application to a gravitational wave detector*. *Journal of Physics E: Scientific Instruments*, 14 (1):65 (1981). URL http://stacks.iop.org/0022-3735/14/i=1/a=018.

[124] Schinke C, Christian Peest P, Schmidt J, Brendel R, Bothe K, Vogt MR, Kröger I, Winter S, Schirmacher A, Lim S, Nguyen HT, and MacDonald D. *Uncertainty analysis for the coefficient of band-to-band absorption of crystalline silicon*. *AIP Advances*, 5 (6):067168–23 (2015).

[125] Schnabel R, Britzger M, Brückner F, *et al. Building blocks for future detectors: Silicon test masses and 1550 nm laser light*. *Journal of Physics: Conference Series*, 228:012029 (2010). URL http://dx.doi.org/10.1088/1742-6596/228/1/012029.

[126] Schroder DK, Thomas RN, and Swartz JC. *Free carrier absorption in silicon*. *IEEE Transactions on Electron Devices*, 25 (2):254–261 (1978). URL http://dx.doi.org/10.1109/T-ED.1978.19066.

[127] Schwarz C, Heinert D, Haughian K, Hofmann G, Komma J, Martin IW, Murray P, Rowan S, Seidel P, and Nawrodt R. *Mechanical Spectroscopy of Silicon as a Low Loss Material for High Precision Mechanical and Optical Experiments*. *Solid State Phenomena*, 184:443–448 (2012). URL http://dx.doi.org/10.4028/www.scientific.net/SSP.184.443.

[128] Shapiro B, Adhikari RX, Aguiar O, Bonilla E, Fan D, Gan L, Gomez I, Khandelwal S, Lantz B, MacDonald T, and Madden-Fong D. *Cryogenically cooled ultra low vibration silicon mirrors for gravitational wave observatories*. *Cryogenics*, 81:83–92 (2017). URL http://dx.doi.org/https://doi.org/10.1016/j.cryogenics.2016.12.004.

[129] Shimamura K, Uda S, Yamada T, Sakaguchi S, and Fukuda T. *Silicon Single Crystal Fiber Growth by Micro Pulling Down Method*. *Japanese Journal of Applied Physics*, 35 (Part 2, No. 6B):L793–L795 (1996). URL http://dx.doi.org/10.1143/JJAP.35.L793.

[130] Sidles JA and Sigg D. *Optical torques in suspended Fabry Perot interferometers*. *Physics Letters A*, 354:167–172 (2006). URL http://dx.doi.org/10.1016/j.physleta.2006.01.051.

[131] Sidorov N, Teplyakova N, Palatnikov M, Aleshina L, Sidorova O, and Kadetova A. *Raman spectroscopy and X-Ray analysis of non-stoichiometric lithium niobate crystals*. *Journal of Solid State Chemistry*, 282:121109 (2020). URL http://dx.doi.org/https://doi.org/10.1016/j.jssc.2019.121109.

[132] Singh S, Arai K, Adhikari RX, and Tao D. *2-micron, HIGH QE Photodetector for Quantum Metrology*. Technical report, LIGO Scientific Collaboration (2019). URL https://dcc.ligo.org/LIGO-T1900380.

[133] Spallino L, Angelucci M, Pasqualetti A, Battes K, Day C, Grohmann S, Majorana E, Ricci F, and Cimino R. *Cryogenic vacuum considerations for future gravitational wave detectors*. *Phys. Rev. D*, 104 (6):062001 (2021). URL http://dx.doi.org/10.1103/PhysRevD.104.062001.

[134] Spitzer W and Fan HY. *Infrared Absorption in n-Type Silicon*. *Physical Review*, 108 (2):268–271 (1957).

[135] Staley A, Martynov D, Abbott R, *et al.* *Achieving resonance in the Advanced LIGO gravitational-wave interferometer*. *Classical and Quantum Gravity*, 31 (24):245010 (2014). URL http://dx.doi.org/10.1088/0264-9381/31/24/245010.

[136] Stefszky MS, Mow-Lowry CM, Y Chua SS, Shaddock DA, Buchler BC, Vahlbruch H, Khalaidovski A, Schnabel R, Lam PK, and McClelland DE. *Balanced homodyne detection of optical quantum states at audio-band frequencies and below*. *Classical and Quantum Gravity*, 29 (14):145015 (2012). URL http://dx.doi.org/10.1088/0264-9381/29/14/145015. 1205.3229.

[137] Steinlechner J and Martin IW. *Thermal noise from icy mirrors in gravitational wave detectors*. *Phys. Rev. Research*, 1 (1):013008 (2019). URL http://dx.doi.org/10.1103/PhysRevResearch.1.013008.

[138] Suzuki T, Tsubono K, and Hirakawa H. *Quality factor of vibration of aluminum alloy disks*. *Physics Letters A*, 67 (1):2–4 (1978). URL http://dx.doi.org/https://doi.org/10.1016/0375-9601(78)90549-2.

[139] Svantesson KG and Nilsson NG. *Determination of the temperature dependence of the free carrier and interband absorption in silicon at 1.06μm*. *Journal of Physics C: Solid State Physics*, 12 (18):3837–3842 (1979).

[140] Takahashi R, Saito Y, Fukushima M, Ando M, Arai K, Tatsumi D, Heinzel G, Kawamura S, Yamazaki T, and Moriwaki S. *Direct measurement of residual gas effect on the sensitivity in TAMA300*. *Journal of Vacuum Science and Technology A: Vacuum, Surfaces, and Films* (2002).

[141] Tan DTH, Qian G, Gosciniak J, Venkatram N, Wang T, Ji W, and Cui Y. *Multi-photon absorption and third-order nonlinearity in silicon at mid-infrared wavelengths*. *Optics Express*, 21 (26):32192–32198 (2013).

[142] Tan W, Qiu X, Zhao G, *et al.* *High-efficiency frequency upconversion of 1.5 μm laser based on a doubly resonant external ring cavity with a low finesse for signal field*. *Applied Physics B*, 123 (2):52 (2017). URL http://dx.doi.org/10.1007/s00340-016-6626-2.

[143] Tang Y, Huang C, Wang S, Li H, and Xu J. *High-power narrow-bandwidth thulium fiber laser with an all-fiber cavity*. *Opt. Express*, 20 (16):17539–17544 (2012). URL http://dx.doi.org/10.1364/OE.20.017539.

[144] Tanioka S and Aso Y. *Optical loss study of the cryogenic molecular layer using a folded cavity for future gravitational-wave detectors*. *Opt. Express*, 29 (5):6780 (2021). URL http://dx.doi.org/10.1364/OE.415921.

[145] Tanioka S, Hasegawa K, and Aso Y. *Optical loss study of molecular layer for a cryogenic interferometric gravitational-wave detector*. *Phys. Rev. D*, 102 (2):022009 (2020). URL http://dx.doi.org/10.1103/PhysRevD.102.022009. Publisher: American Physical Society.

[146] Tao Y, Navaretti P, Hauert R, Grob U, Poggio M, and C L Degen. *Permanent reduction of dissipation in nanomechanical Si resonators by chemical surface protection*. *Nanotechnology*, 26 (46):465501 (2015). URL http://dx.doi.org/10.1088/0957-4484/26/46/465501.

[147] Terkowski L, Martin IW, Axmann D, *et al.* *Influence of deposition parameters on the optical absorption of amorphous silicon thin films*. *Phys. Rev. Res.*, 2:033308 (2020). URL http://dx.doi.org/10.1103/PhysRevResearch.2.033308.

[148] Thorne KS. *Light Scattering and Proposed Baffle Configuration for the LIGO*. LIGO technical report, Caltech, http://www.ligo.caltech.edu/docs/T/T890017-00.pdf (1989).

[149] Touloukian YS. *Specific heat: metallic elements and alloys*. Plenum Press (1970).

[150] Touloukian YS. *Thermal Conductivity: metallic elements and alloys*. Plenum Press (1970).

[151] Tsai C. *Interband and Intraband Absorption Coefficients of Silicon: Theoretical Frameworks and Formulations*. *IEEE Journal of Selected Topics in Quantum Electronics*, 26 (2):1–10 (2020). URL http://dx.doi.org/10.1109/JSTQE.2019.2943389.

[152] Tuttle J, Canavan ER, DiPirro M, Li X, Franck R, and Green D. *A high-resolution measurement of the low-temperature emissivity of ball infrared black*. *AIP Conference Proceedings*, 1434 (1):1505–1512 (2012). URL http://dx.doi.org/10.1063/1.4707079. https://pubs.aip.org/aip/acp/article-pdf/1434/1/1505/12871301/1505_1_online.pdf.

[153] Tyler NA, Sinclair G, Villarreal GE, Gough G, Baretto J, Sahin D, and Thompson M. *Determining the Optical Nonlinearity of Silicon at Cryogenic Temperatures for Applications in Integrated Photonics*. In *Conference on Lasers and Electro-Optics*, p. JTh1E.5. OSA, Washington, D.C. (2017).

[154] Uehara N, Ueda A, Ueda K, Sekiguchi H, Mitake T, Nakamura K, Kitajima N, and Kataoka I. *Ultralow-loss mirror of the parts-in-10^6 level at 1064 nm*. *Optics Letters*, 20:530–532 (1995). URL http://dx.doi.org/10.1364/OL.20.000530.

[155] Vahlbruch H, Mehmet M, Chelkowski S, Hage B, Franzen A, Lastzka N, Goßler S, Danzmann K, and Schnabel R. *Observation of Squeezed Light with 10-dB Quantum-Noise Reduction*. *Phys. Rev. Lett.*, 100:033602 (2008). URL http://dx.doi.org/10.1103/PhysRevLett.100.033602.

[156] Vinet JY, Brisson V, and Braccini S. *Scattered light noise in gravitational wave interferometric detectors: Coherent effects*. *Phys. Rev. D*, 54:1276–1286 (1996).

[157] Vinet JY, Brisson V, Braccini S, Ferrante I, Pinard L, Bondu F, and Tournié E. *Scattered light noise in gravitational wave interferometric detectors: a statistical approach*. *Physical Review D*, 56 (10):6085 (1997).

[158] Vollmer CE, Baune C, Samblowski A, Eberle T, Händchen V, Fiurášek J, and Schnabel R. *Quantum Up-Conversion of Squeezed Vacuum States from 1550 to 532 nm*. *Phys. Rev. Lett.*, 112:073602 (2014). URL http://dx.doi.org/10.1103/PhysRevLett.112.073602.

[159] Ward RL, Adhikari R, Abbott B, *et al.* *DC readout experiment at the Caltech 40m prototype interferometer*. *Classical and Quantum Gravity*, 25 (11):114030 (2008).

[160] Yablonovitch E and Gmitter T. *Ribbon-to-ribbon float zone single crystal growth stabilized by a thin silicon dioxide skin*. *Applied Physics Letters*, 45 (1):63–65 (1984). URL http://dx.doi.org/10.1063/1.95012.

[161] Yamamoto H. *Core Optics related loss hierarchy of aLIGO*. Technical report, LIGO Scientific Collaboration (2014). URL https://dcc.ligo.org/LIGO-G1400162.

[162] Yamamoto K, Uchiyama T, Miyoki S, Ohashi M, Kuroda K, Ishitsuka H, Akutsu T, Telada S, Tomaru T, Suzuki T, *et al.* *Current status of the CLIO project*. In *Journal of Physics: Conference Series*, volume 122, p. 012002. IOP Publishing (2008).

[163] Yu J, Häfner S, Legero T, Herbers S, Nicolodi D, Ma CY, Riehle F, Sterr U, Kedar D, Robinson JM, Oelker E, and Ye J. *Excess Noise and Photoinduced Effects in Highly Reflective Crystalline Mirror Coatings*. *Phys. Rev. X*, 13:041002 (2023). URL http://dx.doi.org/10.1103/PhysRevX.13.041002.

[164] Zalewski EF and Duda CR. *Silicon photodiode device with 100% external quantum efficiency*. *Appl. Opt.*, 22 (18):2867–2873 (1983). URL http://dx.doi.org/10.1364/AO.22.002867.

[165] Zhang H, Tersoff J, Xu S, Chen H, Zhang Q, Zhang K, Yang Y, Lee CS, Tu KN, Li J, and Lu Y. *Approaching the ideal elastic strain limit in silicon nanowires*. *Science Advances*, 2 (8):e1501382 (2016). URL http://dx.doi.org/10.1126/sciadv.1501382.

[166] Zucker ME and Whitcomb SE. *Measurement of Optical Path Fluctuations due to Residual Gas in the LIGO 40 Meter Interferometer*. *Proceedings of the Seventh Marcel Grossman Meeting on General Relativity* (1996).

A Open questions and R&D items

A.1 Core Optics

Known issues that must be resolved in preparation for manufacturing the Voyager test masses are graphically summarized in Figure 10, and include the following:

- Is it feasible to obtain 45 cm MCZ silicon crystals that meet the Voyager requirements? Alternatively, can a composite test mass be assembled from smaller crystals?
- Will the oxygen impurity in the silicon be high enough to result in excessive substrate absorption? If so, can the rapid annealing technique be applied on large crystals to remedy the problem? Can a subsequent coating anneal be designed so as to improve the coating properties without spoiling the substrate absorption again?
- Which combination of coating materials can achieve the absorption requirement with minimal thermal noise?

A.2 Cryogenics

These items are also listed in Section 4.4.

- **High emissivity coatings:** High emissivity coatings for the cryogenic shields and the test mass barrel need to be selected for radiative heat transfer that are mechanically robust, UHV compatible. In the case of the test mass barrel, the coating also needs to not contribute significant thermal noise. (Section 4.3.5 and Table 4)
- **Bolted joints:** Bolted joints with reliably high thermal conductivity for thermal strap connections to the suspended shields.
- **Suspension cage:** The design of the suspension cage must take into account how it interfaces with the cryogenic shields, especially since parts of it will be cold and other parts warm.
- **Ice layer formation:** Test mass ice layer formation mitigation needs further work. This may be mitigated by careful design of the cooldown procedure, but further active mitigation steps may be required, eg heating of the test mass. (Section 4.4.1)
- **Scattered light:** Laser light scattering off the insides of the cryogenic shields has significant potential to create noise in the interferometer. Requirements need to be set on the BRDF and geometry; and decisions need to be made on whether passive vibration isolation is sufficient or if active isolation is needed. Each shield segment will need its own requirements. (Section 4.2.4)

A.3 Suspension

- **Bulk Si strength:** The bulk Si strength is limited at the level far low from the ultimate Si strength. This yields the current practical stress of the blades and ribbons limited to ~100 MPa. The research to pursuit the stronger bulk Si is necessary. (Section 5.4.2)
- **Si blade/ribbon design and fabrication:** Design and fabrication of practically feasible Si blades and ribbons are still necessary. Eventually they are supposed to be tested regarding the thermal noise performance. (Section 5.4.2)
- **Si Bonding:** Development of thermal-noise-safe Si bonding technology and the tests. (Section 5.4.3)
- **Consideration of the metal final stage:** While we wait for the further development of Si final stage, we can also consider a intermediate upgrade of the final stage using metal material. BeCu is the promising material. (Section 5.4.1)
- **Down select of the ETM actuators:** Section 5.4.4
- **Detailed suspension modeling:** The suspension model need improvement including rigid-body and elastic-body models. Section 5.5.1

A.4 Arm Length Stabilization

- **Auxiliary wavelength laser source:** Meet relative intensity and laser frequency noise requirements to lock arm cavity and auxiliary lasers. Section 8.2.2
- **Arm cavity AUX finesse:** What should the auxiliary laser reflectivity requirements be, and what approximate sensing noise will that result in. Section D
- **ALS system:** How should the auxiliary and pre-stabilized laser frequency comparison be made and what new noise sources are introduced in the final scheme? Section 6

A.5 Thermal Wavefront Control

- Active control of ROC for the test masses is challenging. Section Section 7.3.1

A.6 Laser Source

- Exact topology (fiber/free space interface)
- How we'll inject sidebands for RF control
- Polarization control with fiber laser
- Fiber coupling issues with high power

- SBS - doesn't look like it will be an issue but TBD.
- Other ...

A.7 Quantum Noise

- **Optical loss budget** Several technologies that have reduced optical loss in 1064 nm GWIFO must now be demonstrated at 2 um, including Faraday isolators, mode matching, and optical coatings. An updated, detailed accounting of optical losses in the current interferometer, analogous to T1500188, would help guide this work.
- **Squeezed light sources** Squeezed light sources at 2 um are not yet as developed as at 1064 nm, but further progress is expected to continue as in Fig. 31.
- **Filter cavity loss** Can we demonstrate the reduction of scatter loss at 2 um needed to achieve 10 ppm optical loss in the squeezer filter cavity? See section 9.4 for details.
- **Readout quantum efficiency** InGaAs photodiodes are available with better than 99% quantum efficiency at 1064 and 1550 nm, but not at 1800-2200 nm. Further development is required for either 2 um photodetectors, optical-domain preamplification or upconversion followed by photodetection.

B Tables of Parameters

Parameter	A+	iVoyager	Voyager Deep
Laser wavelength	1064 nm	2050 nm	2050 nm
Input laser power	125 W	60.0 W	200 W
Arm cavity power	751 kW	1.18 MW	3.92 MW
Mirror substrate	fused silica	silicon	silicon
Mirror radius	17.0 cm	15.0 cm	22.5 cm
ITM transmission	0.014	0.0014	0.0014
PRM transmission	0.03	0.07	0.072
SRM transmission	0.33	0.048	0.040
Mirror thickness	20.0 cm	60.0 cm	30.0 cm
Beam radius on ITM/ETM	5.5 cm/6.2 cm	5.6 cm/5.6 cm	5.9 cm/8.5 cm
Mass per stage	22/22/40/40 kg	120/83/100/100 kg	50/70/200/200 kg
Final stage temperature	290 K	123 K	123 K
Final stage construction	fused silica fiber	BeCu ribbon	silicon ribbon
Final stage length	0.59 m	0.60 m	0.78 m
Newtonian noise suppression	N/A	2.0	10
Squeeze factor	12 dB	18 dB	18 dB
Squeeze injection loss	0.05	0.04	0.04
Squeeze filter cavity length	300 m	300 m	300 m
Squeeze filter cavity loss (RT)	60×10^{-6}	10×10^{-6}	10×10^{-6}

TABLE 14: Parameters varied by the iVoyager and Voyager designs, relative to A+.

C Material Properties Summary

Summary of relevant material properties.

C.1 Optical and thermal properties for silicon and fused silica

Property	Silicon at 123 K	Silicon at 295 K	Fused silica at 295 K
Thermal expansion (1/K)	1×10^{-9}	2.6×10^{-6}	3.9×10^{-7}
Specific heat (J/kg/K)	300	700	739
Thermal conductivity (W/m/K)	700	130	1.38
Refractive index	3.5	3.45	1.438
dn/dT	1×10^{-4}	1.78×10^{-4}	1.1×10^{-5}

TABLE 15: Optical and thermal properties for silicon or fused silica used for sensitivity calculations in Fig. 9. See [1] for details.

C.2 Infrared Blackbody Radiation

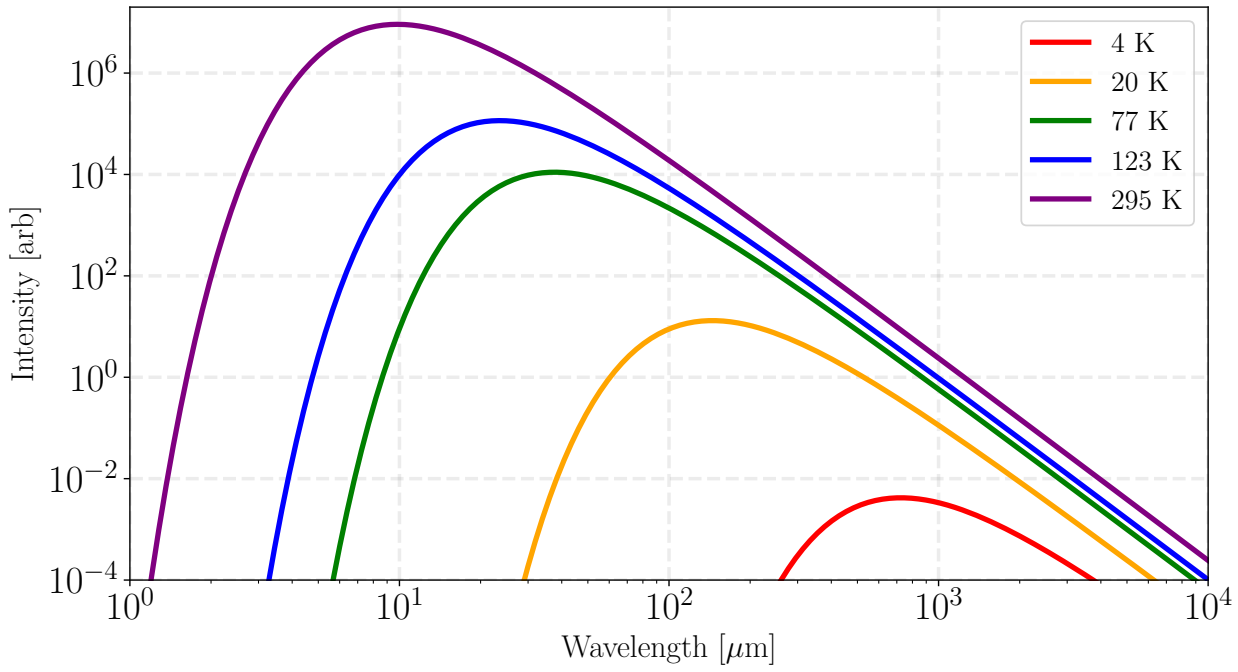

FIGURE 38: Black Body Radiation Spectrum for a few different temperatures.

C.3 Thermal Expansion

C.4 Thermal Conductivity

C.5 Thermo-Refractive Coefficient

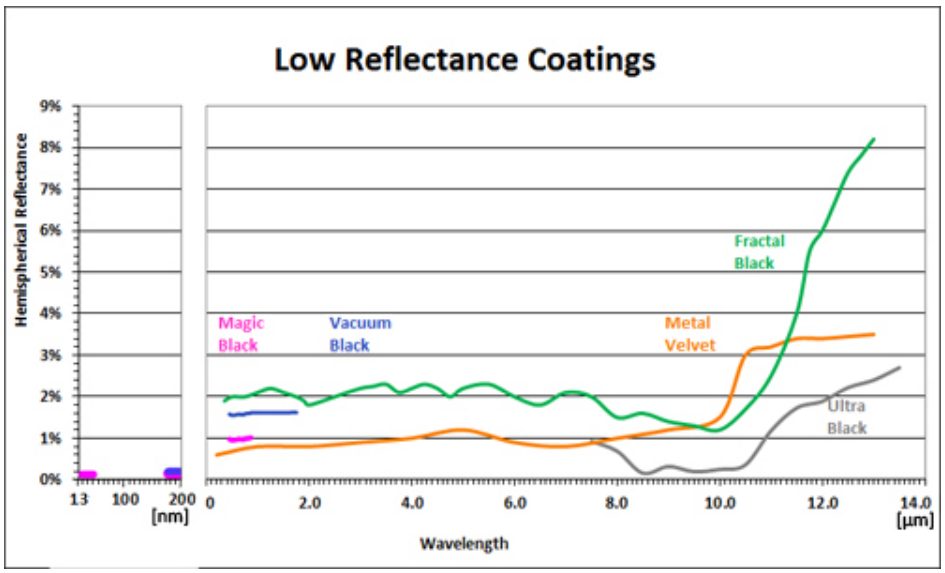

FIGURE 39: Reflectance of commercial high emissivity coatings available from Acktar.

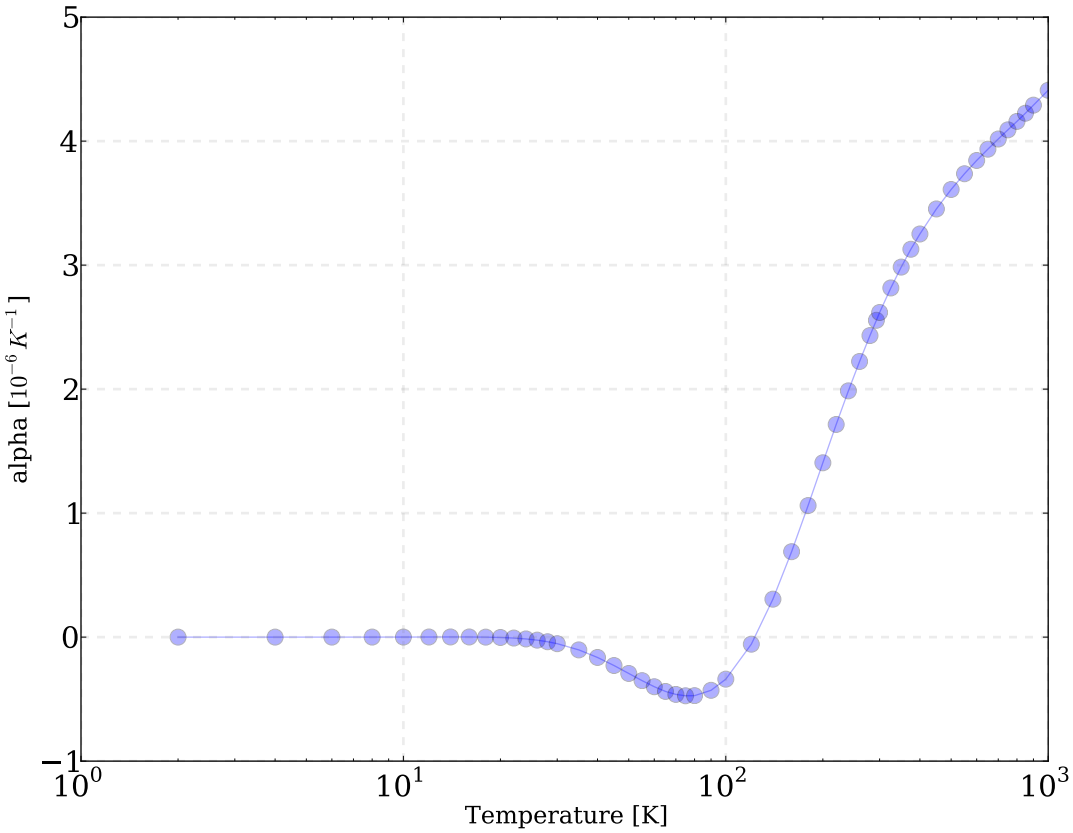

FIGURE 40: Thermal Expansion coefficient of silicon as a function of temperature. From NIST / CODATA Swenson (1983)

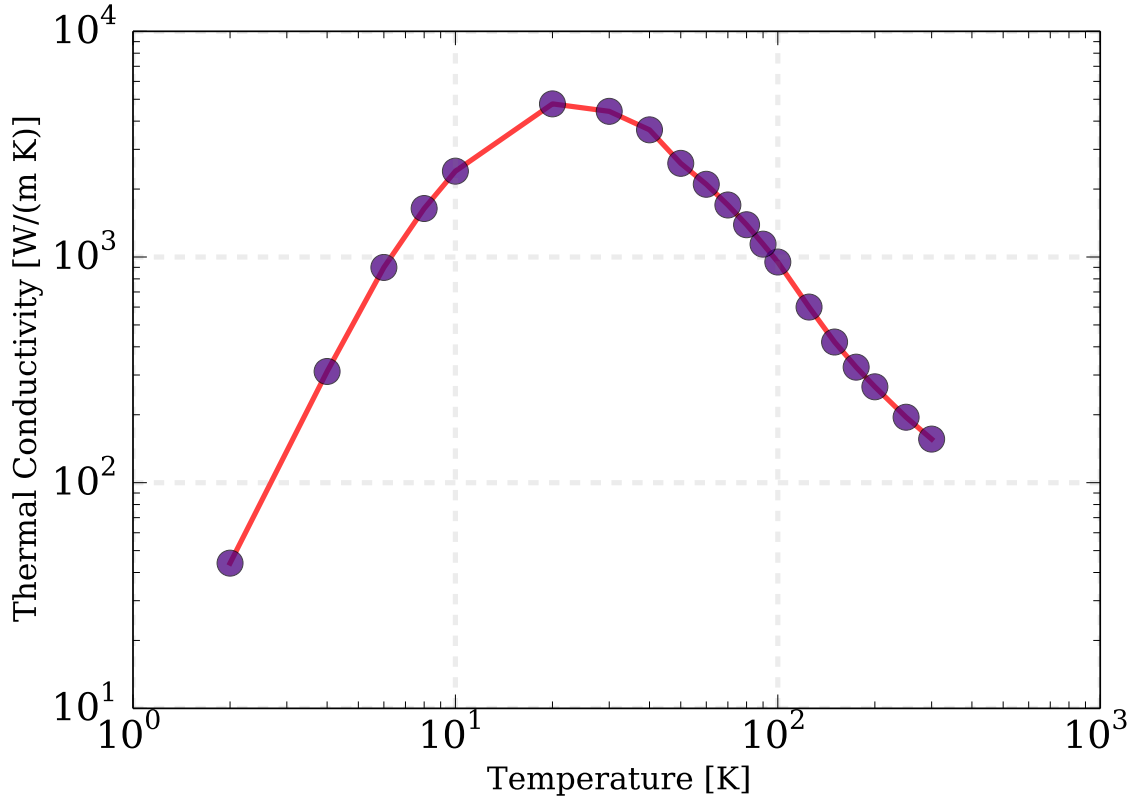

FIGURE 41: Thermal Conductivity of single crystal silicon [50]

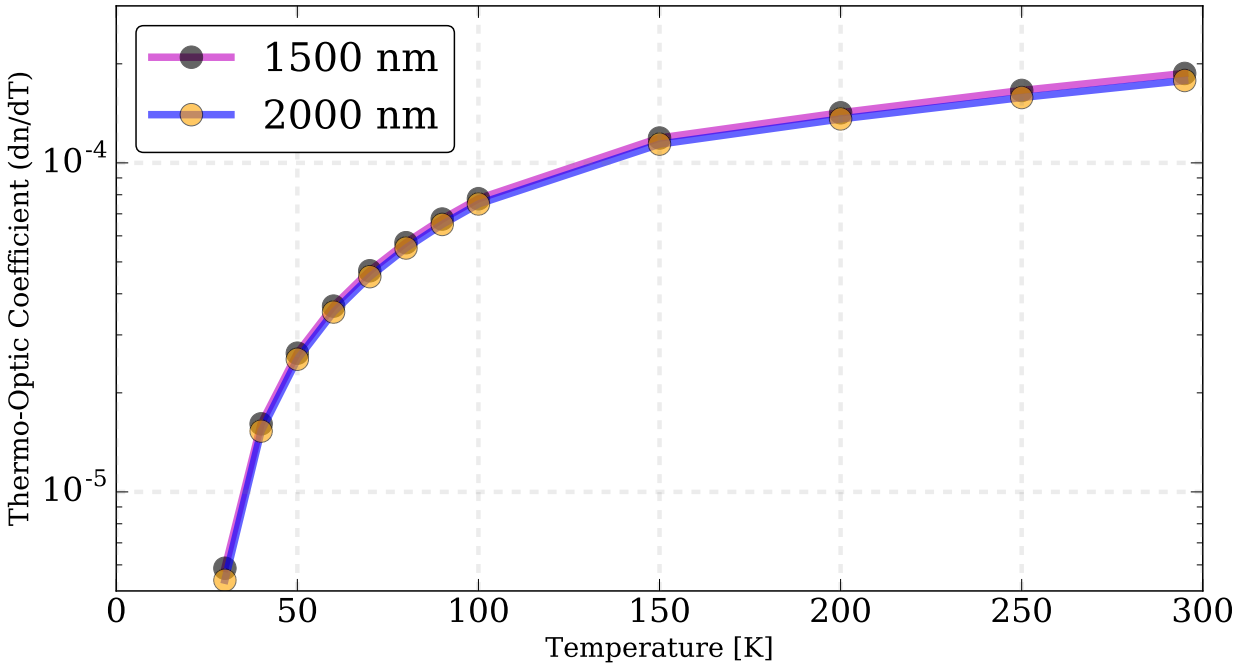

FIGURE 42: dn/dT of Silicon as a function of temperature at 1500 and 2000 nm

dn/dT of Silicon [45] as a function of temperature at 1500 and 2000 nm

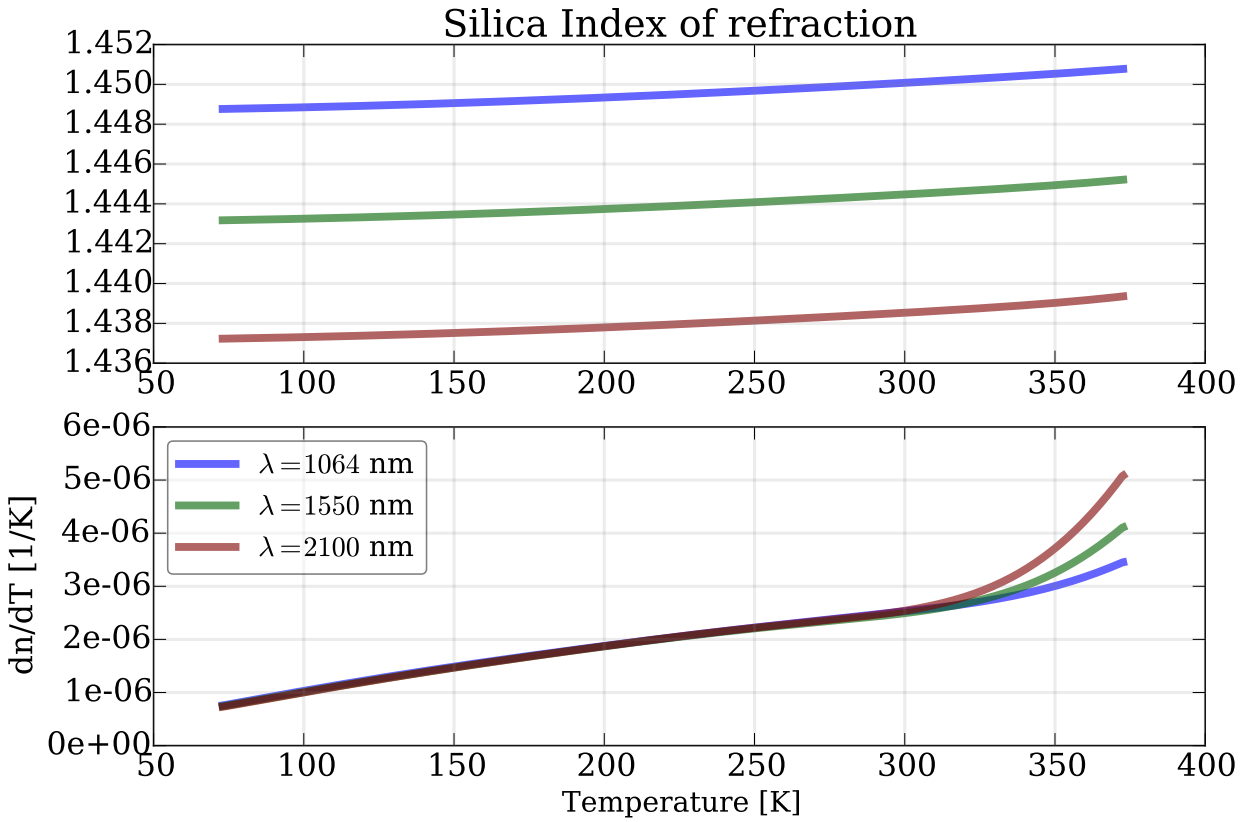

FIGURE 43: Index variation of SiO_2 with temperature and wavelength [82]

D HR Mirror Coating

D.1 Amorphous silica/silicon

Due to the low mechanical loss of amorphous silicon [84, 106, 117], and its high index contrast with respect to amorphous silica, there may be substantial promise in exploring this as a HR coating design for the Voyager test masses.

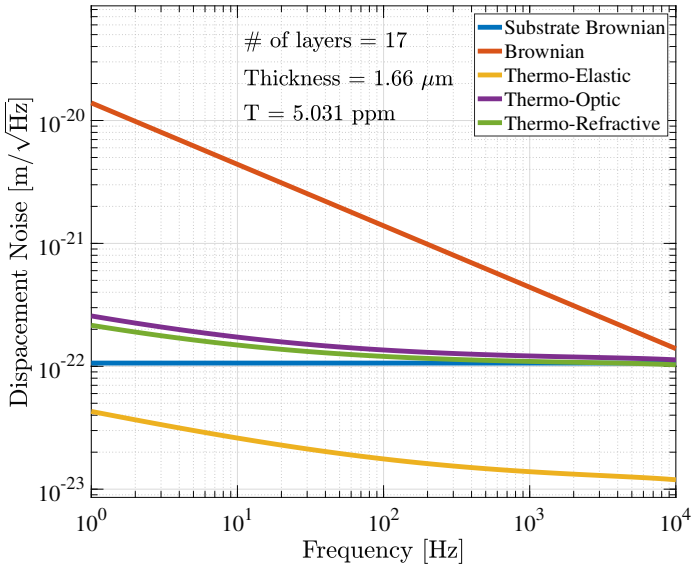

FIGURE 44: Thermal noise of a silicon mirror at 123 K with an α-Si:SiO_2 HR coating and a 6 cm beam spot radius.

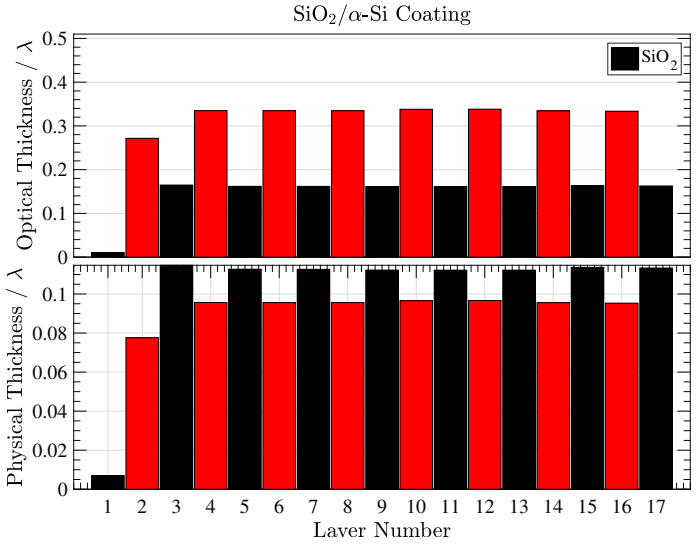

FIGURE 45: Layer structure for the α-Si:SiO_2 HR coating. Coating design optimized to minimize Brownian noise, meet the 5 ppm transmission goal, and minimize first order sensitivity to coating thickness and index of refraction errors.

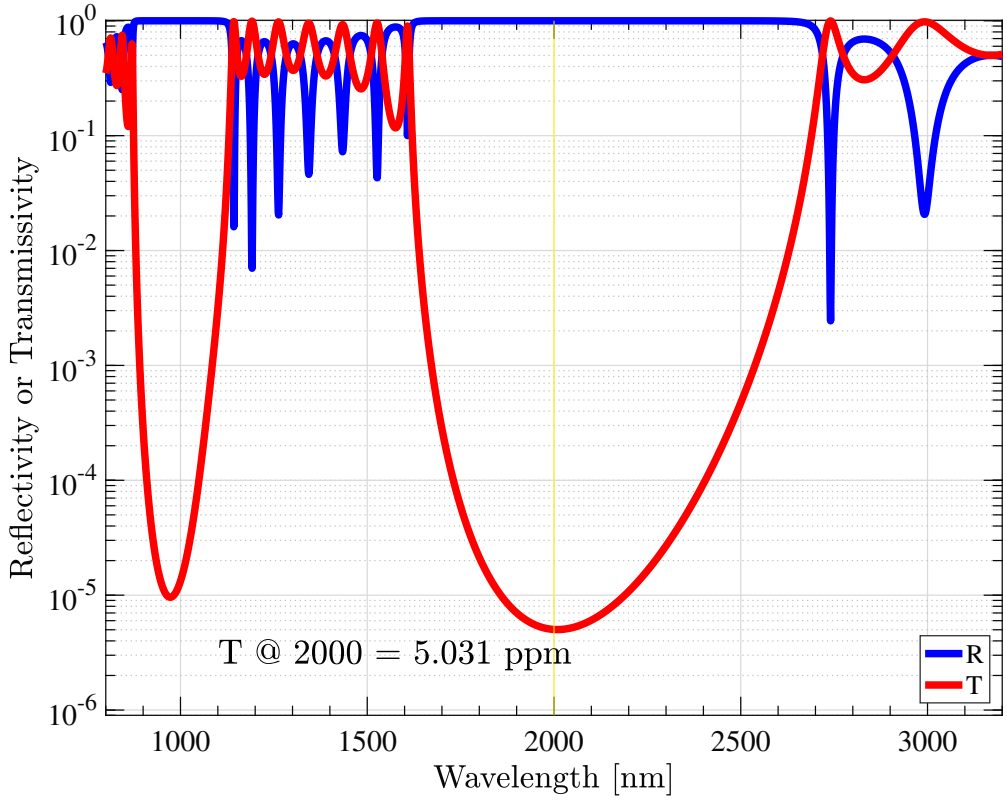

FIGURE 46: Reflection and transmission calculations for the α-Si:SiO_2 HR coating.

Material property	α-Si	SiO_2
Mechanical loss	2.0×10^{-6}	10×10^{-6}
Optical absorption	$0.01\,\mathrm{cm}^{-1}$	$0.0001\,\mathrm{cm}^{-1}$
Young's modulus	150 GPa	270 GPa
Poisson ratio	0.23	0.25
Thermal conductivity	$1.03\,\mathrm{W\,m^{-1}\,K^{-1}}$	$0.270\,\mathrm{W\,m^{-1}\,K^{-1}}$
Volume-specific heat	$1.05\,\mathrm{MJ\,m^{-3}\,K^{-1}}$	$230\,\mathrm{J\,m^{-3}\,K^{-1}}$
Thermal expansion	$1.0 \times 10^{-9}\,\mathrm{K}^{-1}$	$2.6 \times 10^{-6}\,\mathrm{K}^{-1}$
dn/dT	$140 \times 10^{-6}\,\mathrm{K}^{-1}$	$40 \times 10^{-6}\,\mathrm{K}^{-1}$
Refractive index	3.650	2.170

TABLE 16: Parameters used in the HR coating design for the test masses.

D.2 α-Si:SiN

Silicon nitride seems to also be a good low index material to use. It has no low temperature loss peak, and therefore may be a substitute for SiO_2 in a coating in which amorphous silicon is used as the high index material.

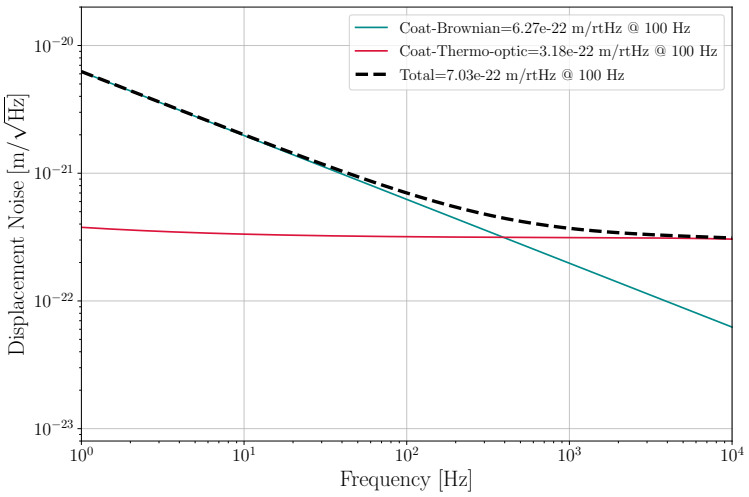

FIGURE 47: Thermal noise of a silicon ETM at 123 K with an α-Si:SiN HR coating and a 8.45 cm beam spot radius.

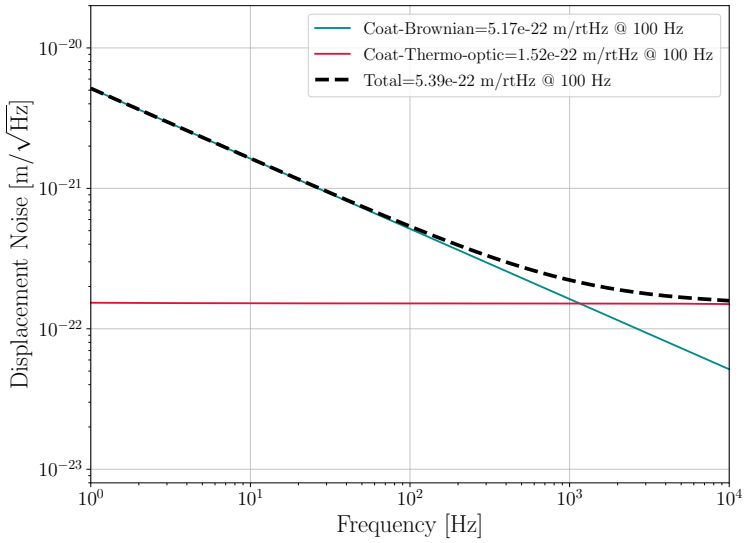

FIGURE 48: Thermal noise of a silicon ITM at 123 K with an α-Si:SiN HR coating and a 5.92 cm beam spot radius.

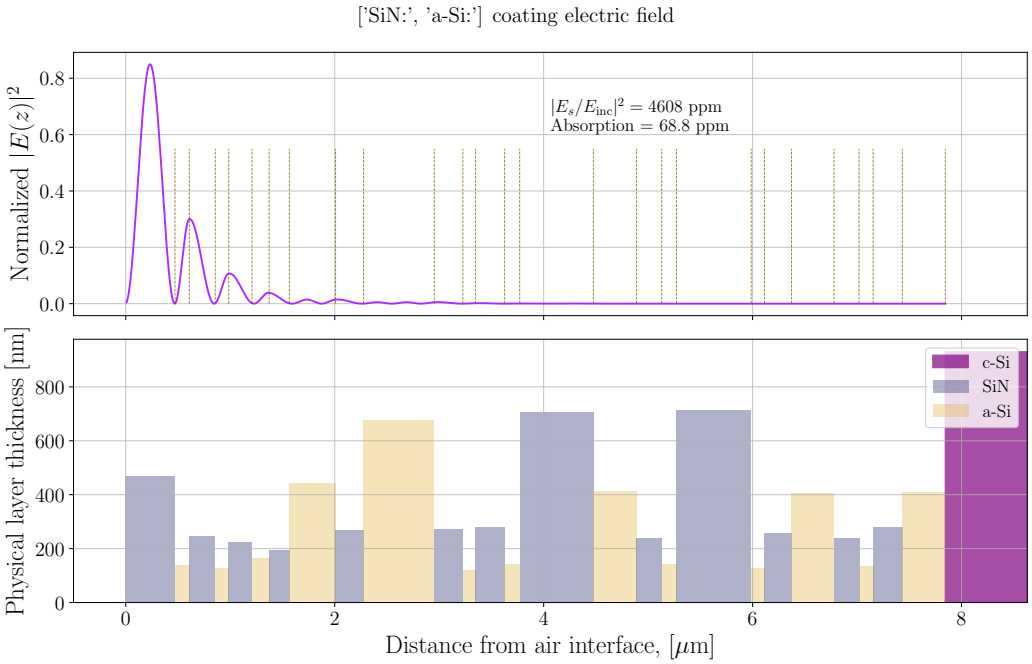

FIGURE 49: Layer structure for the α-Si:SiN ETM HR coating. Coating design optimized to minimize Brownian noise, meet the 5 ppm transmission goal, and minimize first order sensitivity to coating thickness and index of refraction errors.

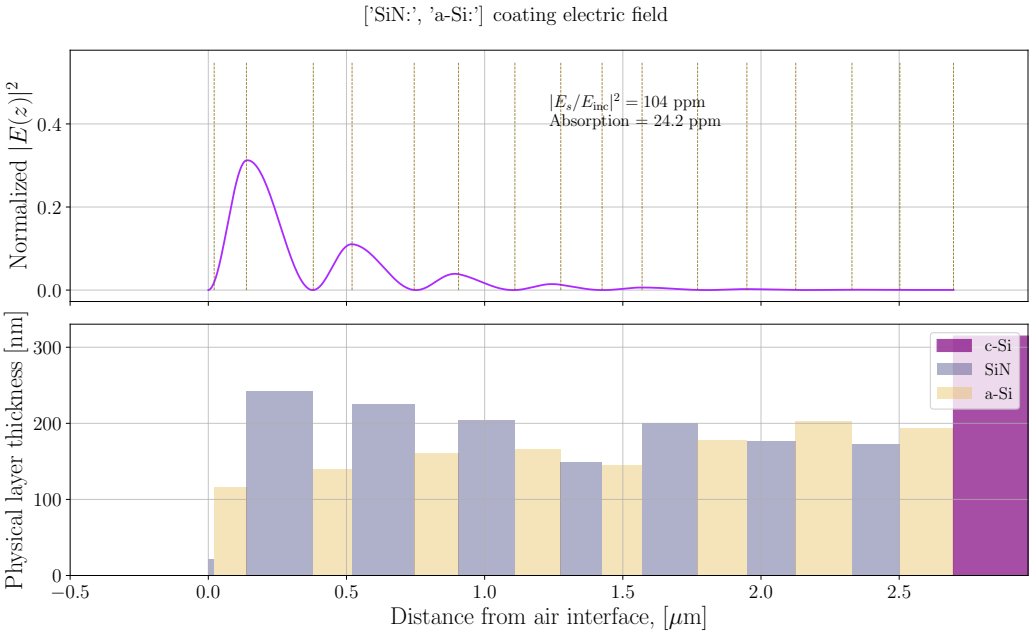

FIGURE 50: Layer structure for the α-Si:SiN ITM HR coating. Coating design optimized to minimize Brownian noise, meet the 1300 ppm transmission goal, and minimize first order sensitivity to coating thickness and index of refraction errors.

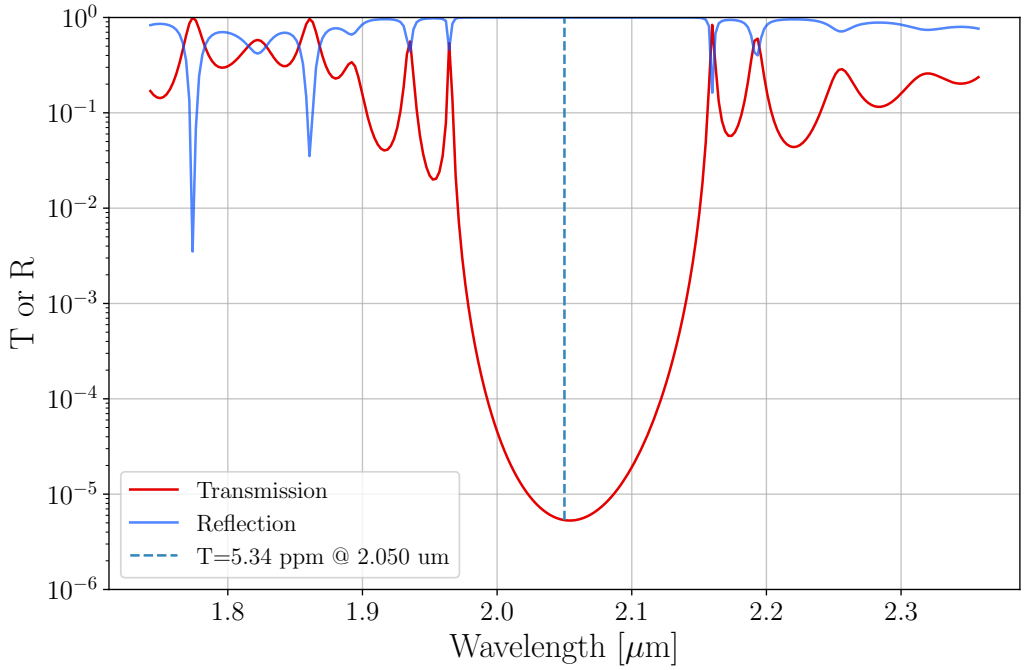

FIGURE 51: Reflection and transmission calculations for the α-Si:SiN ETM HR coating.

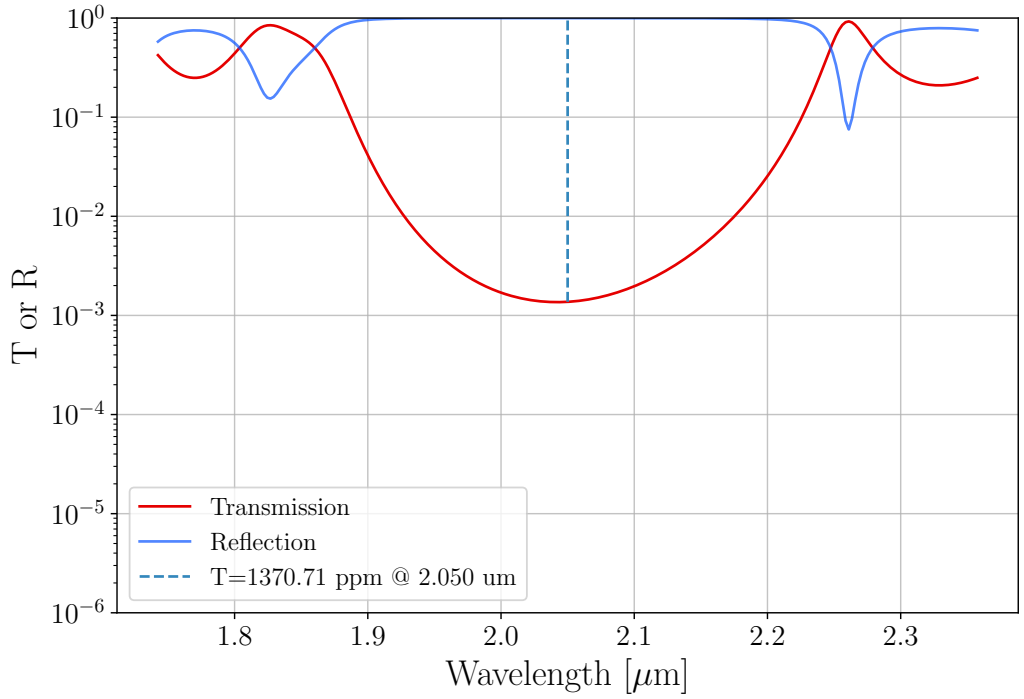

FIGURE 52: Reflection and transmission calculations for the α-Si:SiN ITM HR coating.

E Scattered Light

Practically, all of the high sensitivity interferometers in the past 30 years have been limited at some frequencies by the non-fundamental phase and amplitude fluctuations due to scattered light. The phenomenon of excess noise due to scattered light has been known about for many years [123]. Both the phase and amplitude quadrature of the scattered light are important. The former contributes directly to the phase of the interferometer while the latter contributes via radiation pressure on the optics [112]. The methods by which to combat scattered light have been developing steadily and involve the highest levels of experimental artistry in the field of laser interferometry.

Due to imperfections in the optics, for example, a small fraction of the laser light escapes from the main interferometer beam path. This light then interacts with something (e.g. a piece of the vacuum system or some other suspended optic or beam dump) and then recombines with the circulating laser field within the interferometer [41, 48, 112, 148, 156, 157]. The recombination may occur at virtually any point within the system: inside of the Fabry-Perot arm cavities, at the beamsplitter, or even at the final photodetector which records the GW strain signal. Scattered light induced noise in the sensing of auxiliary degrees of freedom can couple into the strain channel through the relevant feedback control systems.

E.1 Optical Scatter Loss

Optical scatter from the mirror surface leads to degradation of the shot noise limited sensitivity (due to lack of signal gain), increased backscatter from the vacuum equipment, and degradation of the squeezing amplitude (cf. Section 9.3.2).

Arm Cavity Loss If we set, as a goal, a stored arm cavity power of 3 MW (limited only by radiative cooling capacity), then this determines the minimum input laser power from simple conservation of energy arguments:

$$P_{PSL} = 150\,W \left(\frac{0.8}{T_{IO}}\right)\left(\frac{L_{mirror}}{10\text{ ppm}}\right)\left(\frac{P_{arm}}{3\text{ MW}}\right) \tag{5}$$

where we are assuming a baseline input optics efficiency of 80% (PMC, modulators, IMC, isolators), neglecting the optical losses in the Michelson, and assuming that the scatter losses per test mass are reduced from the current level of ~ 40 ppm to 10 ppm. This loss reduction is projected to come from two effects [161].

The first is that for all losses which come from small scale (≤ 2 mm) defects (such as dust or micro-roughness), we can assume that the 'Golden Rule' applies:

$$Loss = \left(\frac{4\pi\sigma}{\lambda}\right)^2 \tag{6}$$

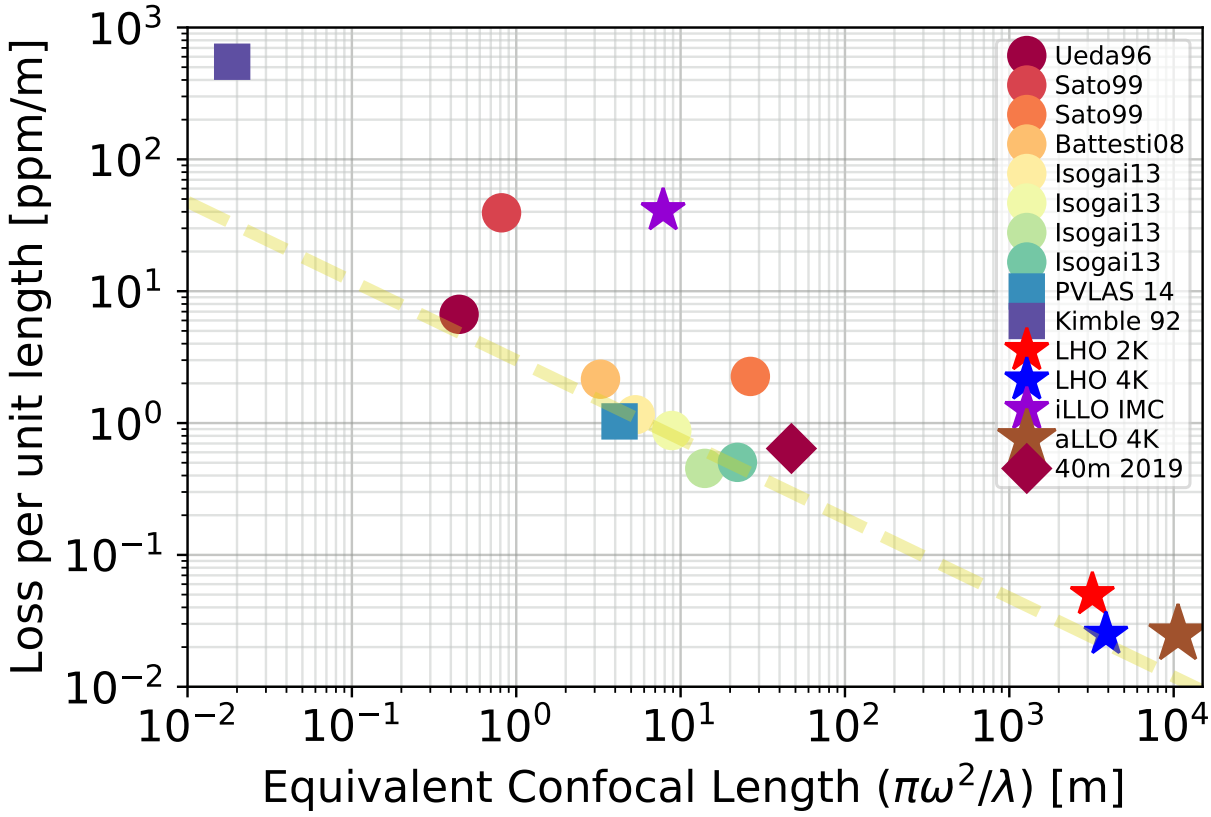

FIGURE 53: Data on Losses taken from [66]. Other data from [120],[154], [31], and the eLIGO and aLIGO electronic logbooks. The dashed line here is just to guide the eye – notice that it falls slower than $1/L_{con}$.

where σ is the RMS surface micro-roughness and λ is the laser wavelength. If this holds, we would get a factor of ~4 in loss reduction, if the surface roughness remains the same. Through discussions with Zygo, it seems that the metrology and ion beam figuring can be accomplished on silicon approximately as well as on silica [75]. However, not all of the power lost goes into wide angles.

The second factor of two comes from the removal of point defects in the coating. This is at the moment just a guess, but is based on current efforts to remove these defects through post-deposition annealing.

Squeezing Filter Cavity For all proposed filter cavity configurations [39], the beam spot size is less than a few mm. For such small beams, Equation 6 should apply, and we should expect a corresponding loss reduction as we increase the laser wavelength. Hence, we use a round trip loss of 10 ppm instead of the 40 ppm assumed for 1064 nm.

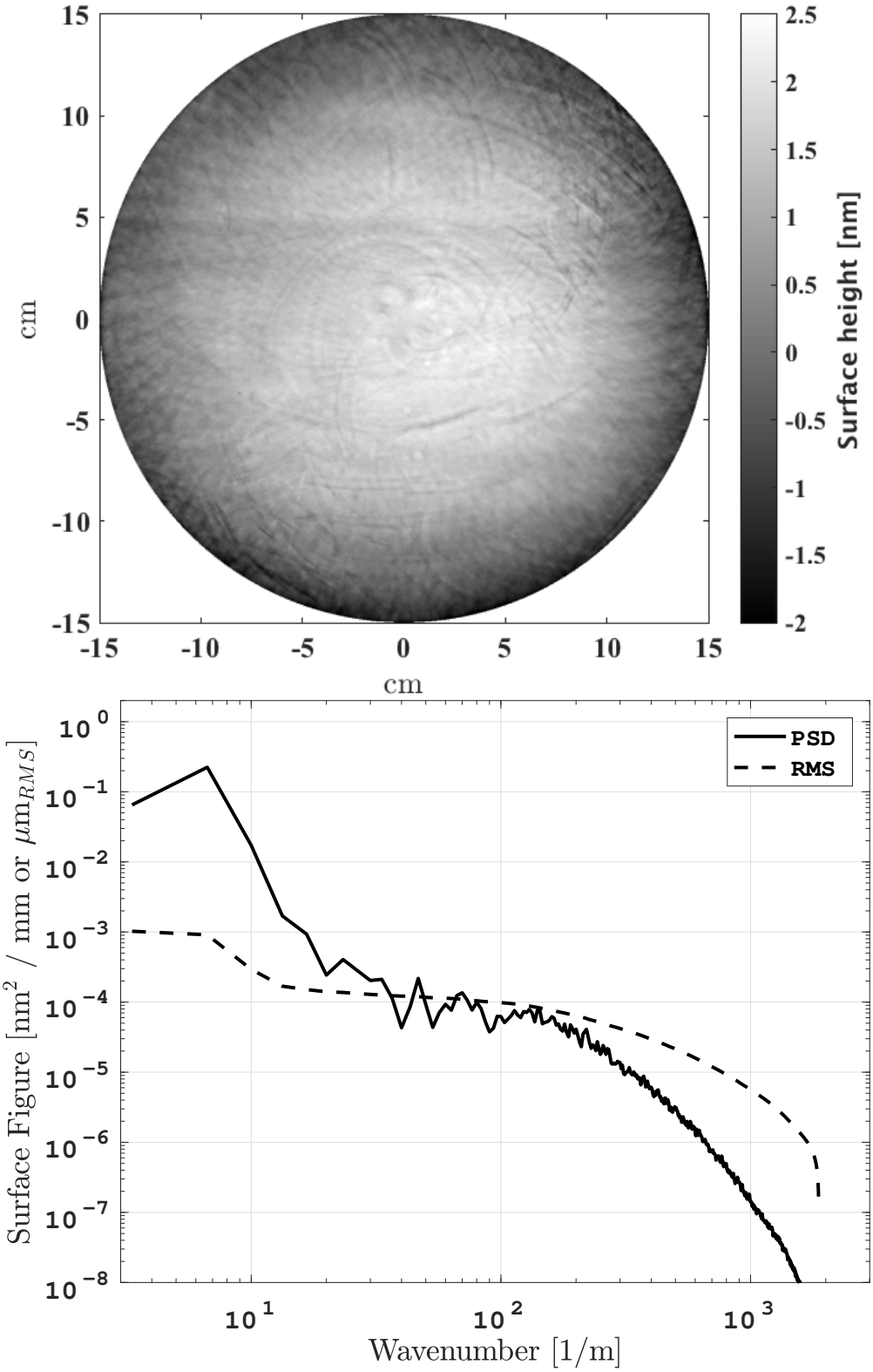

FIGURE 54: (left) Surface figure of an uncoated LIGO mirror (ETM07) with the spherical curvature and tilt subtracted. The ripple pattern at a radius of 3 – 15 cm from the center is due to the planetary coating technique. (right) 1D power spectrum of surface. Also plotted is the RMS surface roughness integrated from high to low spatial frequency.

E.2 Case I: The Beam Tube Baffles

The case of scattering from the multi-km beam tubes connecting the ends of the interferometer has been studied by Whitcomb, Weiss, Thorne, and Flanagan (for LIGO) and by Braccini, Vinet, et al. (for Virgo); see references above. Here we provide a condensed version of their arguments so as to construct a noise budget for backscatter. Let us assume in this case that the field scatters from the test mass surface, reflects from a piece of multi-km long beamtube, returns to the same test mass mirror, and then recombines into the circulating cavity mode. The resulting phase fluctuation of the electric field will be

$$\delta u_s = \frac{4\pi}{\lambda} x_s(f) \sqrt{P_s} \tag{7}$$

For comparison, the field fluctuation due to mirror motion will be

$$\delta u_m = \frac{4\pi}{\lambda} x_m(f) \sqrt{P_0} \tag{8}$$

where x_s is the motion of the beamtube in the direction of the mirror, x_m is the motion of the interferometer mirror, λ is the laser wavelength, P_0 is the power stored in the arm cavity, and P_s is the power which recombines into the circulating cavity mode. Ignoring for a moment the radiation pressure effects, we can see that the phase noise due to this type of backscatter can be simply expressed (in units of mirror displacement) using the ratios of the stored power and the backscattered power which recombines with the cavity mode:

$$x_m(f) = x_s(f) \sqrt{\frac{P_s}{2P_0}} \tag{9}$$

where the factor of 2 comes from only including phase fluctuations of the backscattered field.

So in order to estimate the x_m, we will have to compute P_s. This can be written down by tracing the path of the beam and considering the relevant scattering cross sections at each step [148]:

1. The probability for the main beam to scatter into some angle towards a potential backscatterer.
2. The probability for that backscatterer to scatter light back towards the mirror.
3. The probability for that backscattered field to recombine into the cavity mode.

$$P_s = P_0 \frac{\lambda^2}{d^2} \delta\Omega_{ms} \frac{dP}{d\Omega_{ms}} \frac{dP}{d\Omega_{bm}} \frac{dP}{d\Omega_{sm}} \tag{10}$$

In the above equation, the scatter probability is used; this is related to the more commonly used Bidirectional Reflectance Distribution Function (BRDF) by $\mathrm{BRDF}(\theta) \times cos(\theta) = dP/d\Omega$, where $\theta = 0$ corresponds to normal incidence. The scattering in/out of the main

cavity mode has time reversal symmetry, and so the first and last probabilities in Eq. (10) are equal:

$$P_s = P_0 \frac{\lambda^2}{d^2} \delta\Omega_{ms} \left(\frac{dP}{d\Omega_{ms}} \right)^2 \frac{dP}{d\Omega_{bm}} \tag{11}$$

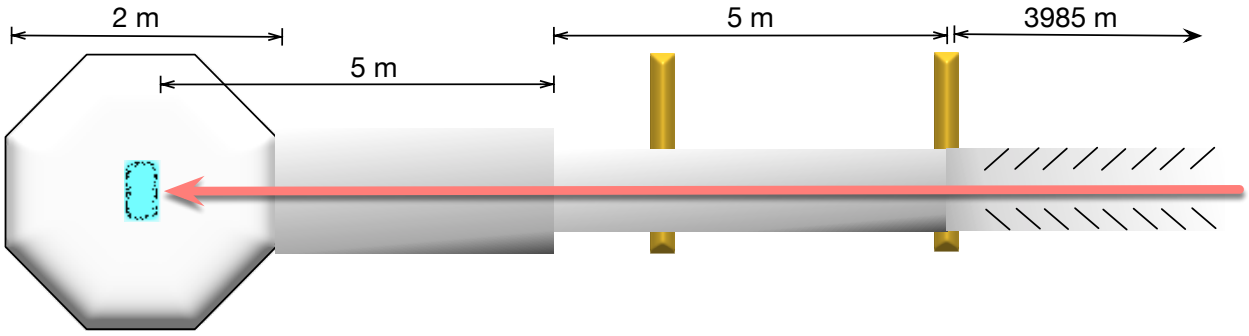

FIGURE 55: Schematic diagram of a LIGO interferometer mirror and surrounding vacuum chambers responsible for backscattered light.

Based on the dimensions in Fig. 55, we can see that we should consider angles of $\sim r_{\rm tube}/d_{\rm scat}$, where $r_{\rm tube} \simeq 0.5$ m and $d_{\rm scat}$ ~10 – 4000 m for the mirror BRDF. For light scattered into these angles ($\theta_{scat} = \lambda/\lambda_{rough} \simeq 0.1$–50 mrad), we need to consider spatial scales on the mirror of (cf. Figure 54) $\lambda_{rough} \sim 0.001 - 1$ cm.

E.3 Case II: The Test Mass Chambers

During the operation of the first generation of kilometer scale interferometers, it became clear that the scattered light from the test mass mirrors was not all concentrated into small angles (as predicted by theory for super-polished optics). To calculate the total power scattered into wide angles, one can use the equivalent of Fermi's 'Golden Rule' (Eq. (6)) for optical scattering.

Combining the measurement result from Fig. 54 with Eq. (6), we can see that the power radiated into angles greater than 1 degree should be less than 0.1 ppm. This underestimates the true number by at least 2 orders of magnitude.

Based on cavity ringdown and resonant reflectivity tests (cf. [66]), the round trip (arm cavity) loss in the initial LIGO interferometers ranged from ~60 – 140 ppm. For two of the Advanced LIGO interferometers, the loss is in the ~80 – 120 ppm range. Wide angle, *in situ*, measurements (using calibrated photodetectors and CCD cameras) show that the total loss for $\theta_{scat} \gtrsim 1$ deg is ~ 15 ppm. However, it is not at all clear that the angular distribution in that range is that of a Lambertian surface. Measurements taken at angles of ~ (0.5 m)/(4000 m) ≈ 0.1 mrad show a large azimuthal dependence (i.e. the BRDF is not symmetric around the beam axis). Imaging of the optics implicates point-like structures. Repeated cleaning of the surface using various techniques reveals a largely unchanging pattern, implying that the points are defects in the dielectric mirror coatings, rather than surface contaminants. Although the details of the story are still

being investigated, it seems possible that the defects are due to artifacts of the ion beam sputtering process [119] as well as crystal formation [118] in the amorphous thin films during the post-deposition annealing.

E.4 Case III: Backscatter from the Dark Port

Another location which requires much care in design is the (dark) detection port of the interferometer. Since it is in this location that the very small optical phase measurements are done, any small fields at this location can be potentially troublesome.

In particular, most of the past and current interferometers have ~5 – 50 mW of light going from the beamsplitter in the direction of the GW detection photodiodes. Some of this light is unwanted (coming from the contrast defect of the light from the two arms) and some is there intentionally (a local oscillator field at either the main laser frequency or offset by tens of MHz in the case of interferometers with heterodyne readout). As with all sources of backscatter, the fields which scatter back into the interferometer from the dark port produce both amplitude and phase modulation.

In order to reduce the backscatter noise from the dark port to an acceptable level, a series of measures are generally taken:

- an Output Mode Cleaner [46, 159] cavity with a ring (3 or 4 mirror) cavity design so as to limit the scattering into the counter propagating mode.
- high quality optics (for low scatter) in the Output Mode Cleaner.
- a Faraday isolator between the interferometer and the output detection systems.
- appropriate angling of the photodetectors so as to minimize the specular reflection and minimize the backscattering into the interferometer.

One promising approach would be to limit the amount of carrier light which is transmitted by the interferometer to the dark port. The idea of making a balanced homodyne readout [47] utilizing a local oscillator field from an auxiliary beam is being pursued as a future upgrade of Advanced LIGO.

E.5 Case IV: The Cryogenic Shielding

Figures 56 to 58 are estimates of the amount of scattered light noise from the various cryo shield segments (see Section 4.3 for technical details). The noise shown assumes equal contributions from all 4 test masses and represents the quadrature sum of all the test mass chambers. The noise also includes radiation pressure and phase noise contributions. Other assumptions are Lambertian reflections, no contributions from multiple reflections, and all shield segments suspended as well damped single stage suspension from the ground (ISI stage 0 for the inner shield). These figures plot the trade space of

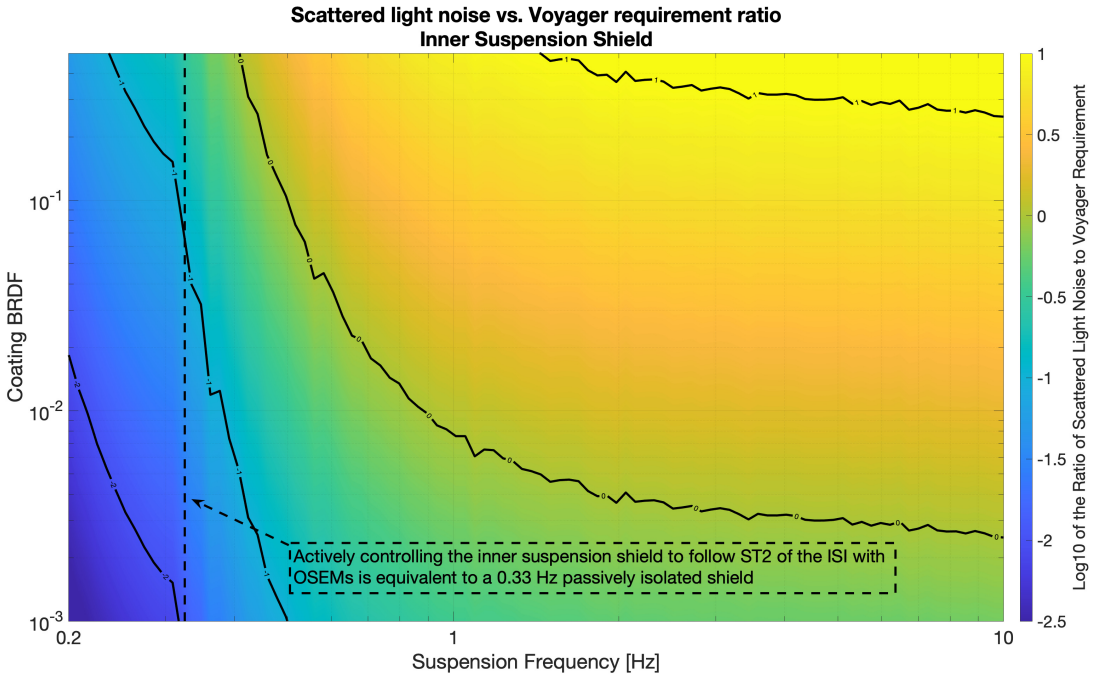

FIGURE 56: Estimated contribution of each ETM shield segment to the total scattered light noise.

BRDF with shield segment suspension frequency, using the ratio of scattered light noise to the Voyager requirement as the metric. This ratio should be less than 0.1 (the -1 contours). These scattered light calculations are based on the work in [16].

The inner suspension shield requires the greatest performance, requiring with the above assumptions a suspension frequency of approximately 0.3 Hz for a 0.1 BRDF, or a frequency of 0.4 Hz for a BRDF of 0.005. There is additionally an option to use active control for this shield. The proposed controller would use displacement sensors, such as OSEMs or capacitive sensors to measure the shield displacement relative to stage 2 (the optics table) of the ISI. Electromagnetic actuators would then force the shield's rigid body motion to follow the well isolated ISI. Discussion of such a controller is given in [128]. Assuming OSEM sensor noise, such an actively controlled shield is equivalent to a 0.33 Hz passively isolated shield, as shown by Fig. 56; assuming contributions from the active shield displacement dominate over rotation.

The cryopump shield has the next greatest performance requirements, despite being the furthest from the test mass. For a BRDF of 0.1, we need a suspension frequency of 0.35 Hz; or for a BRDF of 0.01 a suspension frequency of 0.43 Hz. The inner beam tube shield can have a frequency of about 0.4 Hz with a BRDF of 0.1 or a frequency of 0.5 with a BRDF of 0.01.

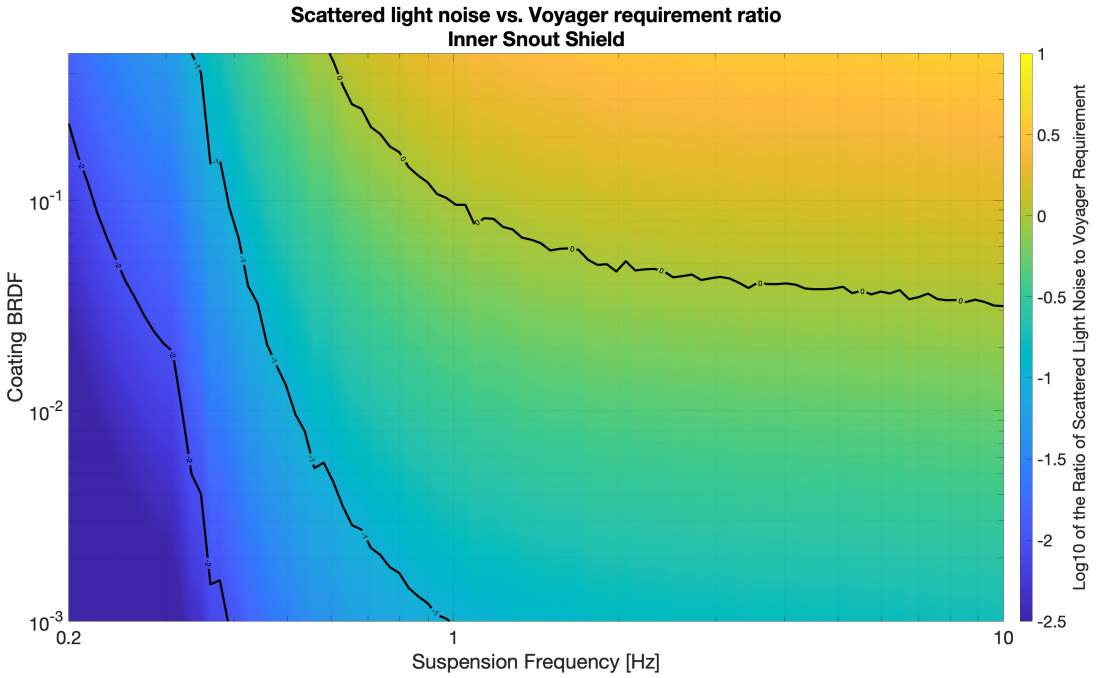

FIGURE 57: Estimated contribution of each ETM shield segment to the total scattered light noise.

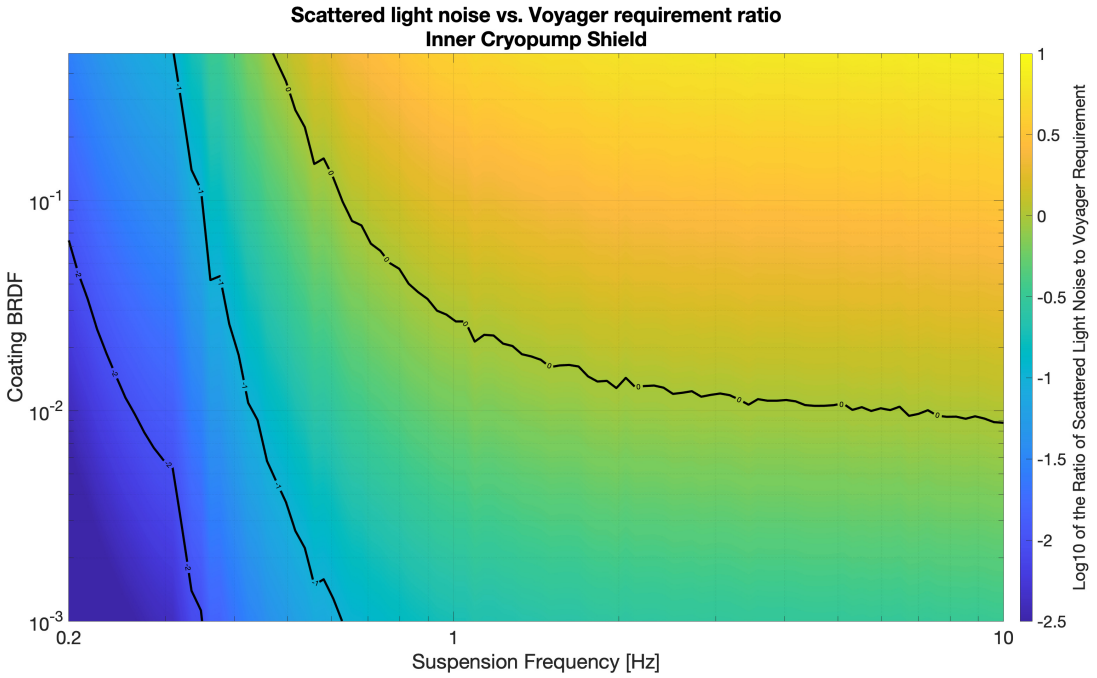

FIGURE 58: Estimated contribution of each ETM shield segment to the total scattered light noise.

F Residual Gas Noise

The amplitude spectral density of path length fluctuations due to residual gas particles in the vacuum system depends not only on the number density of particles, $\rho_{\#}$, but also on the molecular polarizability, $\alpha(\omega)$, of the particular gas species present. For a leak-free vacuum system, the gas species expected to be present are H_2 and H_2O, which will be outgassing and desorbing, respectively, from the tubes, chambers, and equipment contained therein. Air leaks will also deposit N_2 and O_2 molecules as well.

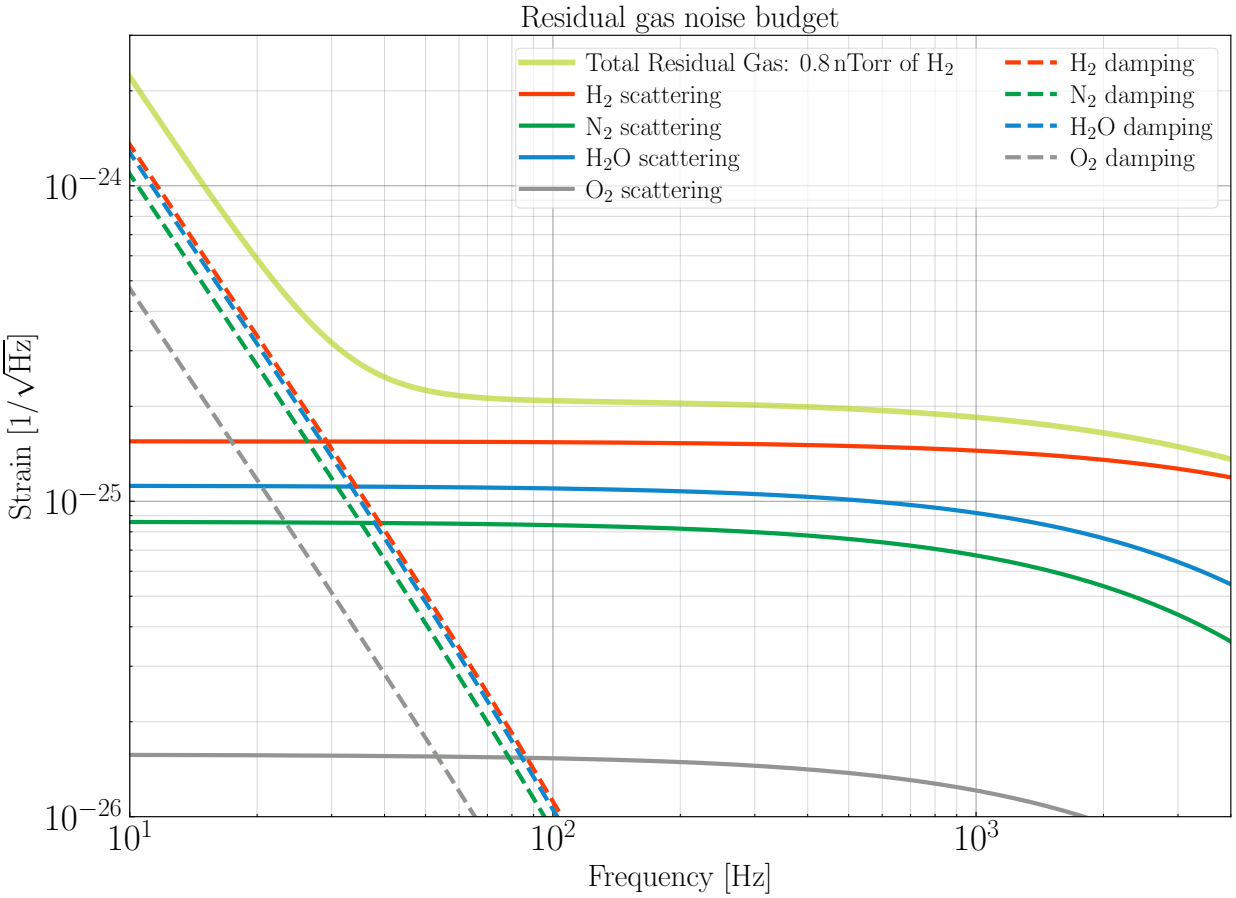

FIGURE 59: Broadband phase noise for each of the main (phase noise inducing) molecular species in the beam tubes.

F.1 Resonant Phase Noise Enhancement

In the $\lambda \sim 0.5-4\,\mu m$ region there is not much H_2 activity, but for the other three gases there are a number of molecular resonances where the dispersion (and therefore $\alpha(\omega)$) can change rapidly and an enhancement of path length fluctuations can occur.

Imaging and spectroscopy research has led to the detailed collection of absorption spectra. Specifically, the HITRAN [59] (*hi*gh-resolution *tran*smission) database contains information about molecular resonances for various compounds over a wide range of

wavelengths. At low pressures it can be assumed that there is no broadening of resonance linewidths due to particle collisions, but the distribution of particle velocities will create a Doppler resonance profile,

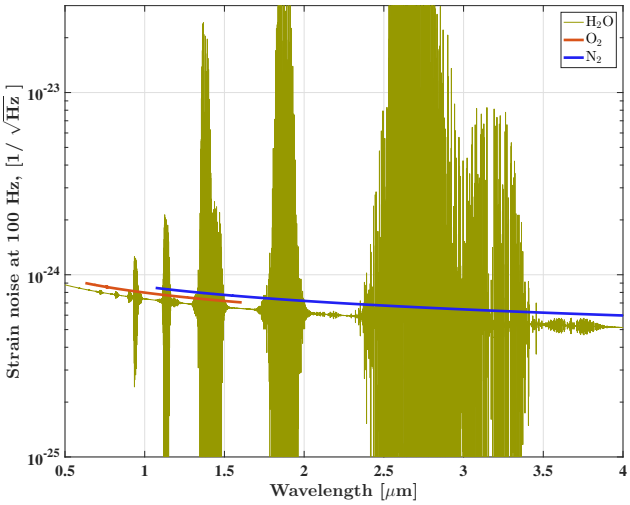

FIGURE 60: Shown here is the strain noise for the three most important gases (each with a partial pressure of 10^{-9} Torr). The actual beam tube pressure for water is close to 10^{-10} Torr (cf. recent RGA measurements). Due to Doppler broadening, each absorption line has a width of ~ 200 MHz and can be easily avoided by temperature tuning of the PSL frequency.

$$f(\nu,\nu_0) = \frac{1}{\sqrt{\pi}\delta\nu} e^{-(\nu-\nu_0)^2/\delta\nu^2}, \delta\nu = \frac{\nu_0}{c}\sqrt{2k_B T/m}, \tag{12}$$

where ν_0 is the wavenumber of the resonance, k_B is Boltzmann's constant, T is the temperature of the molecules (room temperature), and m is the mass of the molecules.

The HITRAN intensity data, coupled with the Doppler profile, results in a spectrum of the absorption coefficient, $k(\omega)$, which can be converted to the index of refraction via the Kramers-Kronig relation,

$$n(\omega) = 1 + \frac{c}{\pi}\int_0^\infty \frac{k(\omega')}{\omega'^2 - \omega^2} d\omega'. \tag{13}$$

Each absorption peak is accompanied by regions of normal and anomalous dispersion. The Clausius-Mossotti relation converts $n(\omega)$ into the polarizability, $\alpha(\omega)$,

$$\alpha(\omega) = \frac{3}{4\pi\rho}\frac{n^2(\omega)-1}{n^2(\omega)+2} \tag{14}$$

and $\alpha(\omega)$ appears in the formulation [140, 166] of the strain noise spectral density,

$$h(f) = \frac{4\pi\alpha}{L}\sqrt{\frac{2\rho_\#}{v_0}\int_0^L \frac{e^{-2\pi f w(z)/v_0}}{w(z)} dz}, \tag{15}$$

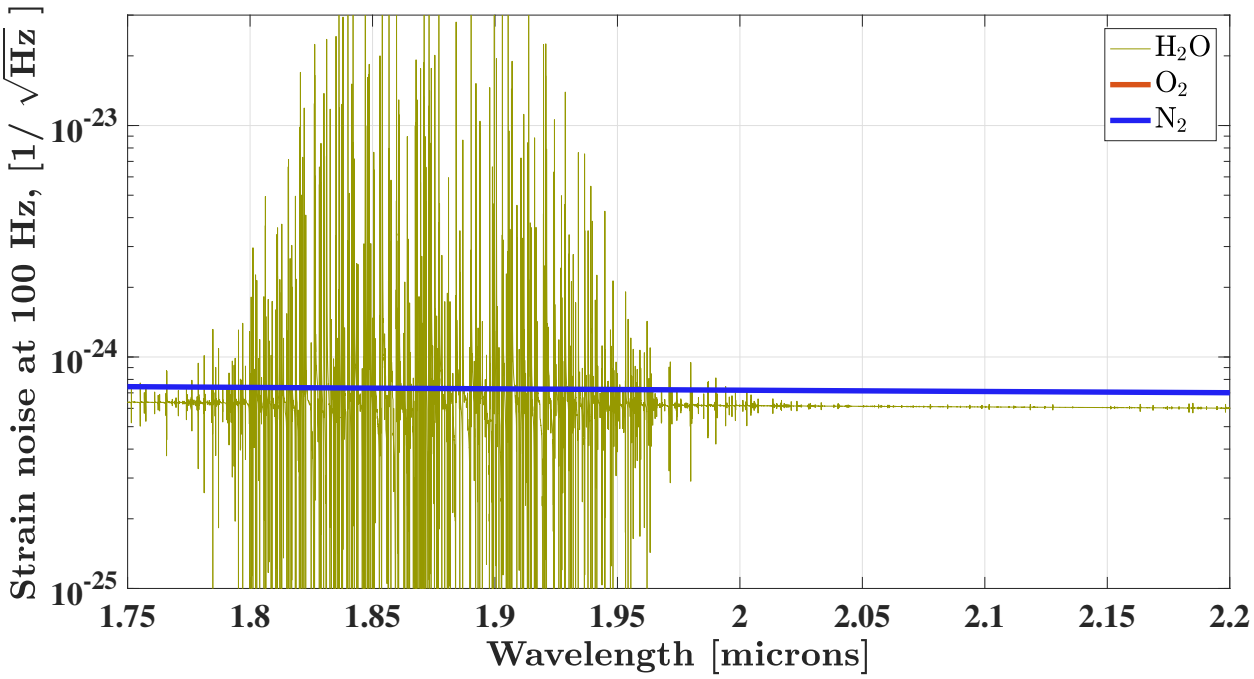

FIGURE 61: The narrow linewidths of absorption features allows for PSL frequencies placed in between resonances. In this band, which has the most water resonances, a 0.1 nm shift in wavelength corresponds to 8.5 GHz, so it is quite reasonable to keep the laser in one of the low strain noise regions. The overall expected strain noise would then be below 10^{-25} for the expected water pressure, and therefore **not a concern** for any foreseeable interferometer topology.

where $v_0 = \sqrt{2k_BT/m}$ is the most probable molecular speed, L is the length of the beam path, and $w(z)$ is the beam's Gaussian radius.

Figure 60 shows the strain noise at 100 Hz as a function of wavelength, for 10^{-9} Torr of a few gases, in an Advanced LIGO arm (calculated with the GWINC function `gas.m`). The O_2 and N_2 resonances only slightly modify their polarizabilities. Water vapor, however, has $> 10^5$ resonances in this band which can enhance the strain noise significantly, though notably not around 1.5 µm or just above 2 µm. Also, closer inspection reveals that the narrow linewidth of the absorption resonances produces several nm wide gaps where there is no appreciable noise enhancement, for instance in the 1.5 – 2 µm region. Data for the following isotopologues (taking abundance into account) are included in the strain noise estimates: H_2, HD, $H_2{}^{16}O$, $H_2{}^{17}O$, $H_2{}^{18}O$, $HD^{16}O$, $HD^{17}O$, $HD^{18}O$, $^{14}N_2$, $^{14}N^{15}N$, $^{16}O_2$, $^{16}O^{17}O$, and $^{16}O^{18}O$.

G Test mass cooldown

In order to maximize the duty cycle of an observatory with cryogenic test masses, some method of cooling is required to reach the desired temperature in a reasonable amount of time.

A "simple" way to do this is with only radiative cooling, which can reach the target TM temperature in a few days. By contrast, it will take 2 – 3 *weeks* to achieve the operating pressure within the LVEA vacuum envelope and open the gate valves to the arms without long-term degradation of water pressure in long tubes. Figure 62 shows pressure curves from an example aLIGO pumpdown of the LLO LVEA.

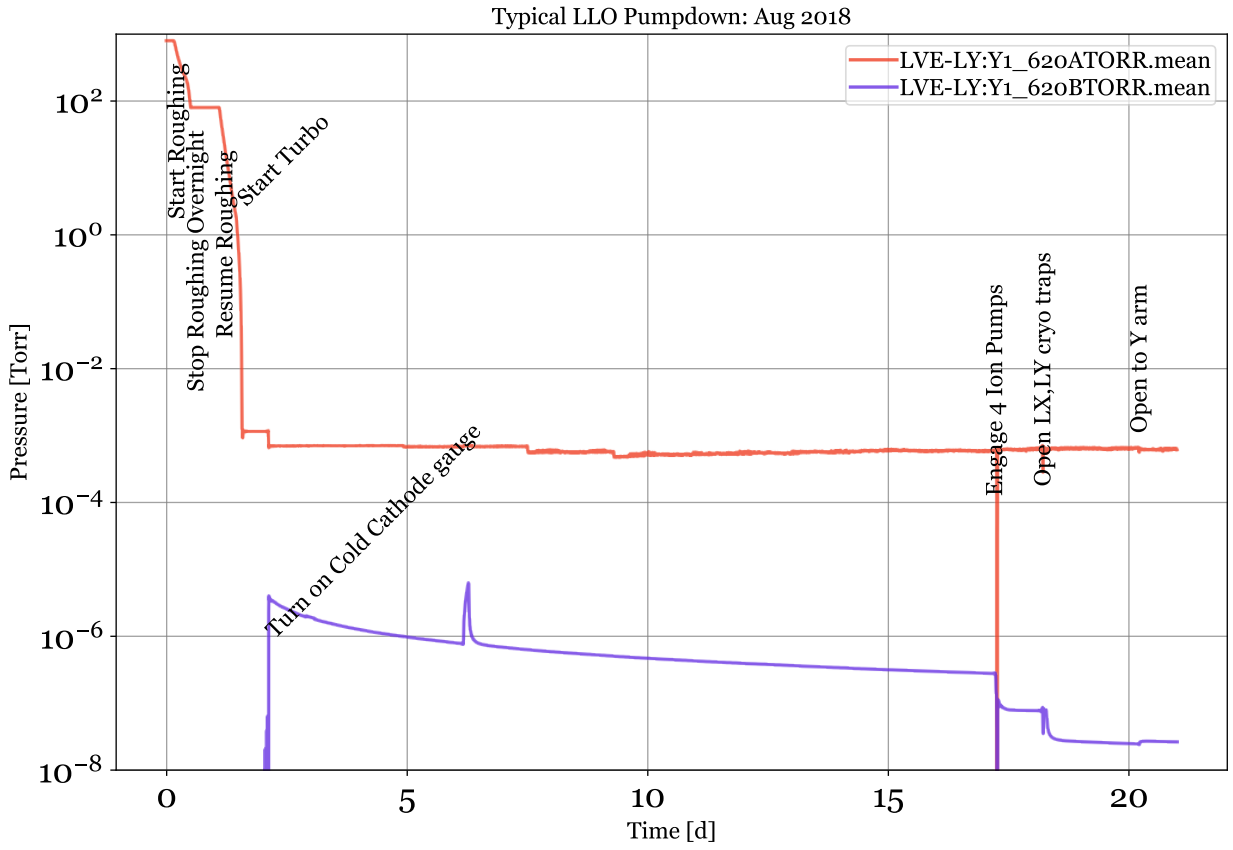

FIGURE 62: Pressure in the LLO LVEA during a typical pumpdown in August 2018. Each of the major transitions is indicated in the text annotations. At the ~18 day mark, the ion pumps are exposed, bringing the pressure to a level where the cryo traps can be engaged. (Data and annotations from S. McCormick and H. Overmeier)

Assuming that the pumpdown time in LIGO Voyager is not reduced substantially from aLIGO, the cooldown must be engineered to not extend the total time between start of pumpdown and interferometer operation.

Fig. 63 shows the result of a numerical simulation of the LIGO Voyager ITM cooldown assuming:

1. Main laser shutter closed during cooldown; opened once TM reaches 123 K

2. TM sees heat from the main beamtube during cooldown
3. inner and outer shield snouts extend 10m towards arm; 5m towards BS
4. emissivity of TM barrel = 0.95
5. emissivity of HR/AR faces = 0.3
6. emissivity of inner shield = 0.95
7. HR absorption of 1 ppm; HR scattering of 10 ppm
8. bulk absorption of 10 ppm/cm
9. temperature dependence of silicon material parameters taken from the standard literature

The discontinuity in the derivative of temperature traces comes from opening the laser shutter once the TM reaches 123 K. The inner shield experiences this effect due to laser scattering off of the TM that gets absorbed by the shield.

The dashed trace is the theoretical radiative cooling limit of a 200 kg silicon optic, assuming an emissivity of 1 and an enclosing bath at 0 K. This caps the fastest radiative cooling time to 123 K at 68 hours.

Modeling realistic radiative cooling of the test mass, the target temperature of 123 K is reached within ~4 days; much quicker than the main volume pumpdown in Fig. 62.

The simulation assumes the inner shield and snout are provided a total of 55 W of lift at 40 K. For more information on cryocooler requirements, see Appendix H.

If it turns out faster cooling times are needed, a mechanically-actuated cold flap (attached to the shield snout) could be used to block the heat from the main beamtube. In addition, more aggressive techniques are discussed in and G1400250 and [16].

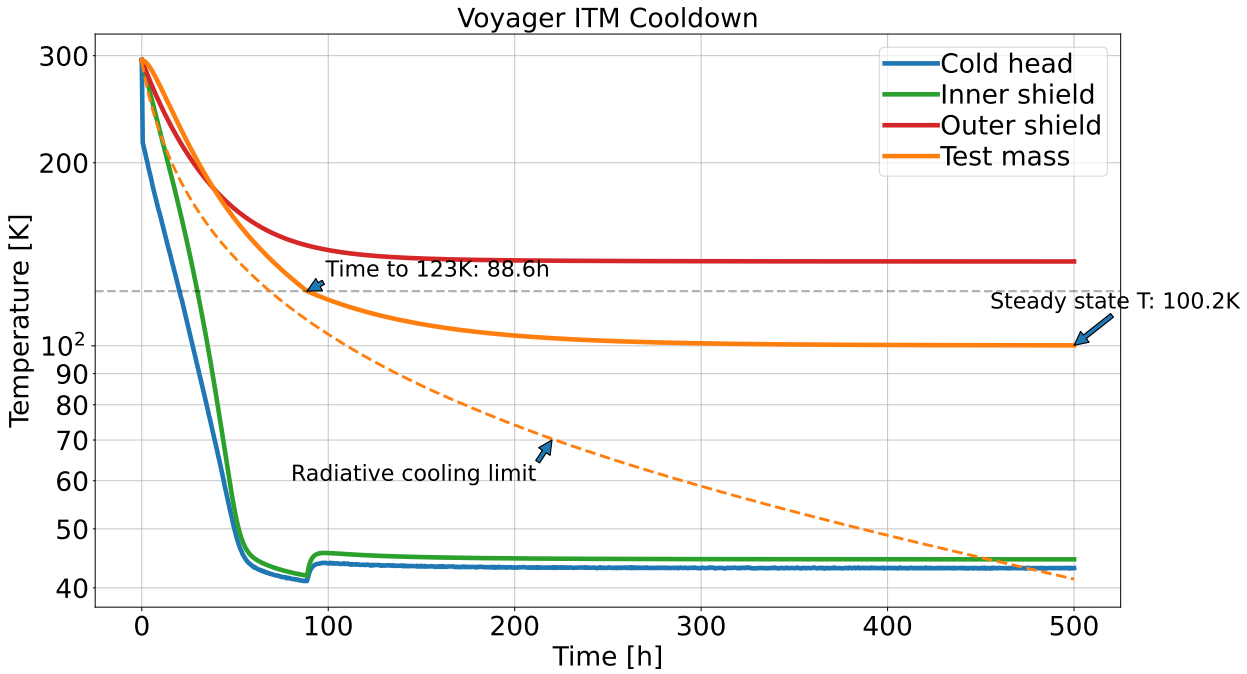

FIGURE 63: Estimate of ITM cooldown via numerical integration. Assuming a TM barrel emissivity of 0.95 and HR/AR emissivity of 0.3.

H Cryocooler Downselection

Cryocoolers need to have sufficient heat lifting capacity down to about 40 K, and also not introduce too much vibration. The required heat lifting capacity can be modeled, and Table 17 lists the requirements. Note that the selected cryocooler will only be responsible for cooling the inner shield and snout pair. A separate LN2 tank will provide the majority of the cooling power to the outer shield and snout, reducing the thermal load on the inner pair and thus lowering the selected cryocooler lift requirement.

However, the coupling from the vibration of the cold head to interferometer is less well known and will depend on in-situ measurements. Fig. 64 illustrates the vibration coupling paths to the test mass and the inner shield, both of which are vibration sensitive. Parts of these paths are not well known in advance. Thus, for vibration, we'll do our best to target known 'low vibration' cryocoolers that also have relatively high operating frequencies so the vibration can be filtered if necessary. This leads us to consider Stirling or high frequency pulse tube coolers.

Unlike pulse tube coolers, free piston Stirling coolers require no maintenance, and Sunpower lists a mean time to failure > 200,000 hours. The mean time to failure for pulse tubes is not currently known to us, but Cryomech only provides a warranty for about 10,000 hours. Stirling coolers are also easy to obtain at operating frequencies at or near 60 Hz. Pulse tubes, while they can be high frequency, are easier to find at low operating frequencies in the regime of 2 Hz. For these reasons, in particular the reliability, we prefer the Stirling coolers.

Shield Component	Min Operating Temp (K)	Cooling Power at Min (W)
Inner Sus Shield + Snout	40	55
Outer Sus Shield + Snout	200	850

TABLE 17: Cryo cooler cooling power requirements

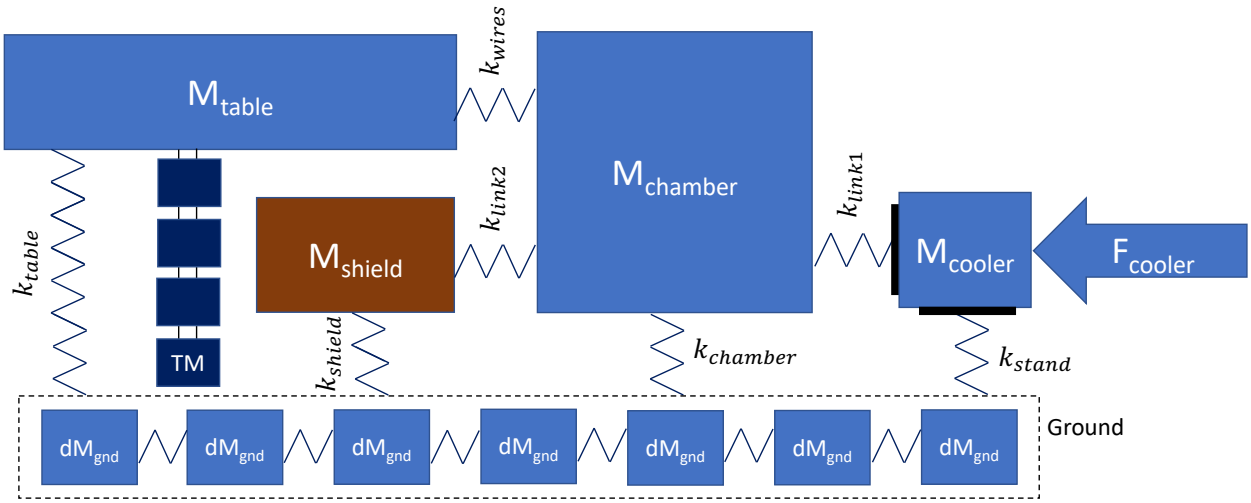

FIGURE 64: A schematic of the cryocooler's vibration path. Any vibration coupling to either the test mass (TM) or the inner heat shields (M_{shield}) can contribute noise to the interferometer.

I Warm vs Cold PUM Downselection

This appendix studies room temperature vs cryogenic PUMs in various configurations. The main driver for a cold PUM is to reduce the thermoelastic noise in the suspension ribbons/fibers supporting the test mass. Other configurations are considered here as possible alternatives to mitigate the challenges involved with the silicon fibers or ribbons by permitting use of established technologies.

Table 18 summarizes the physical differences between the four configurations considered in Fig. 65, which shows the strain suspension thermal noise and total noise seen by DARM. Table 18 shows the configurations in the same order as Fig. 65. Configuration 1 is the Voyager baseline.

All four configurations were assumed to have silicon PUM springs supporting the test mass fibers/ribbons/wires in order to decouple the breaking stress from the bounce and roll mode frequency requirements. Such silicon springs require development. In at least configuration 3 there would be a fused silica to silicon joint, which would also at least require a bonding study, if not development. In practice, configurations 3 and 4 might use silica and maraging steel blades respectively, rather than silicon. However, the choice of spring material here is not likely to alter the noise performance enough to drive this downselection.

Configuration	PUM Temp	Fiber/ribbon material	PUM material	PUM blades
1	123 K	Silicon ribbons	Silicon	Silicon blades
2	295 K	Silicon ribbons	Silicon	Silicon blades
3	295 K	Silica fibers	Silica	Silicon blades
4	123 K	Steel wires	Aluminum	Silicon blades

TABLE 18: Summary of the suspension differences for the warm vs cold PUM configurations.

Given that Fig. 65 shows that the baseline Voyager low frequency noise performance (configuration 1), as well as violin mode thermal noise, is significantly better than the other 3 configurations, we choose not to pursue any of the off-nominal configurations. See T1200099 for more details on the astrophysical motivations for low frequency noise performance.

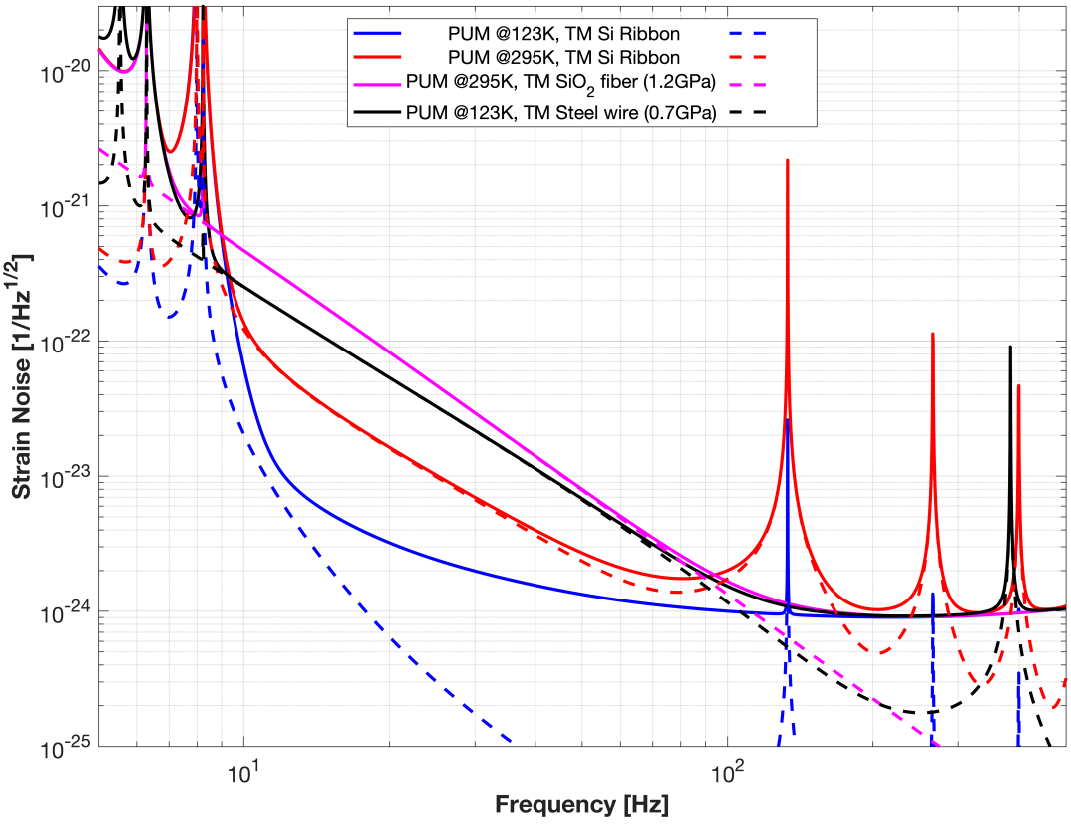

FIGURE 65: Strain noise seen by DARM for various PUM and suspension wire configurations. These curves represent the quadrature sum of the four test masses. Dashed lines are suspension thermal noise, solid lines are total DARM noise.